Accretion flow properties in low-mass X-ray binaries

Sanna, Andrea

rijksuniversiteit
groningen

Accretion flow properties in low-mass X-ray binaries

Proefschrift

ter verkrijging van het doctoraat in de
Wiskunde en Natuurwetenschappen
aan de Rijksuniversiteit Groningen
op gezag van de
Rector Magnificus, dr. E. Sterken,
in het openbaar te verdedigen op
vrijdag 8 februari 2013
om 11.00 uur

door

Andrea Sanna
geboren op 18 mei 1983
te Cagliari, Italië

Promotor:	Prof. dr. R.M. Méndez
Beoordelingscommissie:	Prof. dr. D. Barret Prof. dr. C. Done Prof. dr. L. Stella

ISBN 978-90-367-6018-8
ISBN 978-90-367-6019-5 (electronic version)

Ero matta in mezzo ai matti.
I matti erano matti nel profondo,
alcuni molto intelligenti.
Sono nate lì le mie più belle amicizie.
I matti son simpatici, non come i dementi,
che sono tutti fuori, nel mondo.
I dementi li ho incontrati dopo,
quando sono uscita!

Alda Merini

Ai miei genitori,
che mi hanno donato la vita

A Claudia,
che mi ha donato l'amore

Contents

1 Introduction

All difficult things have their origin in that which is easy, and great things in that which is small

Lao Tzu

In this work I investigate the properties of the accretion flow in interacting binary systems referred to as low-mass X-ray binaries. These systems are among the brightest objects in the X-ray sky, and important cosmic laboratories for studying the properties of dense matter and strong gravitational fields. With this chapter I wish to catch the reader's attention by providing an overview of these fascinating systems and a description of the techniques that I used to study them.

1.1 X-ray binaries

X-ray binaries are binary systems in which a normal star (companion star) and a compact object (a neutron star, black hole, or a white dwarf) orbit around a common center of mass. Mass is transferred from the normal star to the compact object either via stellar winds or Roche-lobe overflow. These systems are powered by the gravitational energy released by matter falling onto the compact object. The extreme compactness of these objects makes the accretion process at least an order of magnitude more powerful than nuclear fusion reactions in normal stars.

X-ray binaries are classified as high-mass X-ray binaries (HMXBs) or low-mass X-ray binaries (LMXBs). In HMXBs the companion star is a massive-

early-type star (type O or B) with a mass of the order of 10 $M_{\odot}$ or larger, characterised by strong winds that transfer mass to the compact object. In LMXBs the companion is a late-type star with a mass typically lower than 1 $M_{\odot}$.

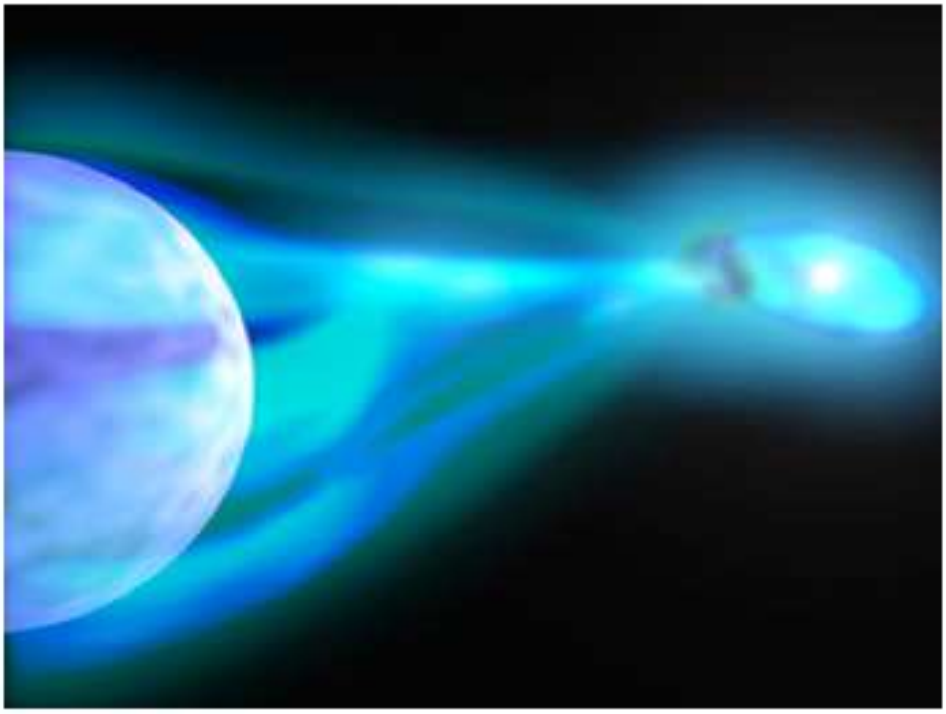

Figure 1.1: Artist's conception of a low-mass X-ray binary. The companion star (left) fills its Roche lobe losing matter which accretes onto the compact object via an accretion disc (right). Image credit: ESA

In this thesis, I focus on the study of the LMXBs (see Figure 1.1 for an artist's impression). In these systems, the orbital separations between the compact object and the companion star is such that material from the outer layers of the latter is stripped off and gravitationally pulled onto the compact object via the first Lagrangian point (e.g., Frank et al., 1992). The volume within which the matter is bound to the companion star (Roche-lobe) depends only on the orbital separation and the masses of the two stars. Therefore, the Roche-lobe overflow requires that either the companion star expands (due to stellar evolution), or that the orbit shrinks (due to losses of orbital angular momentum). As a consequence of the high angular momentum carried by the in-falling material, the radial accretion onto the compact object is prevented;

instead the in-streaming matter spirals in forming a rotating disc. In order to reach the compact object, the matter in the disc has to lose angular momentum. Viscosity and friction allow angular momentum to be transferred outwards as the matter moves inwards, originating a so-called *accretion disc* (Pringle & Rees, 1972). The accretion disc can extend between the first Lagrangian point (which sets the largest outer radius available) and the innermost stable circular orbit (ISCO; Shakura & Sunyaev, 1973). Once matter crosses the ISCO, the gravitational pull disrupts the stable (quasi)circular orbits forcing the matter to plunge onto the compact object.

In the processes of accretion, viscous stresses convert the kinetic energy of the in-falling matter into radiation, which is emitted mainly in the X-ray band. In the vicinity of the compact object, the hottest region of the accretion disc, the temperature can reach up to several millions degrees.

The fact that the energy spectrum of these systems typically extends up to 100 keV implies that the accretion disc is not the only emitting region. The high-energy photons originate in a region called *corona* that probably surrounds both the compact object and the accretion disc (at least the inner part of the disc, close to the compact object). This region is filled with a plasma of hot electrons of temperature up to hundreds of keV. Both the origin and the geometry of the corona are still under debate, however there is evidence (observational and theoretical) that such a hot plasma interacts, via inverse Compton scattering, with the photons emitted from the accretion disc (e.g., Thorne & Price, 1975; Pozdnyakov et al., 1983; Dove et al., 1997).

In neutron-star (NS) LMXBs, the solid surface of the NS and the boundary layer are also emission regions. At the end of the accretion process, the accreting material falls onto the NS surface, releasing the residual gravitational energy into X-ray photons. The boundary layer is the region between the accretion disc and the NS surface over which the accreting matter orbiting in the disc (with frequencies up to 1400 Hz) is forced to slow down to the spin frequency of the NS (typically 10 to 600 Hz).

From all just said, it is clear that the analysis of the X-ray emission from these systems is a fundamental tool to understand the physics of accretion and to investigate the properties of compact objects. Furthermore, the strong gravitational field near the compact objects makes these systems a unique laboratory where to finally test general relativity in extreme conditions (so far only tested in weak field regimes; Taylor et al., 1992). LMXBs with accreting neutron stars allow us to study physics of matter at extreme densities (up to 10^{15} g cm^{-3}), so far unachievable in laboratories, and to constrain the equation of state (i.e., the mathematical description of the relations between temperature, pressure and density of matter) of these objects.

1.2 Techniques

The only source of information that we have (at least for the moment) to understand X-ray binaries comes from studies of the photons emitted from these systems. Even though the focus of this thesis is in the X-ray emission, these systems have a broad emission spectrum that extends from radio to gamma rays. Current technologies do not allow us to resolve LMXBs using direct imaging in X-ray, therefore we rely on timing and spectral techniques to understand the evolution and the physical parameters of these systems. Here I briefly describe the timing and spectral analysis commonly used in the X-ray band, with more focus on the techniques applied in this thesis.

1.2.1 Timing analysis

X-ray light curves of LMXBs show variability in a very wide range of timescales, from years to milliseconds, reflecting different aspects of the accretion processes. Of particular interest for this thesis is the rapid variability (on milliseconds scale) which can probe the properties of the accreting matter orbiting in the inner edge of the accretion disc, where the strong gravitational field of the compact-object is the dominant force. The X-ray emission from these systems is a stochastic process, and the main tool used for studying the very fast variability is the Fourier power density spectrum (PDS), which gives a representation of the signal in the frequency domain. By applying the Fourier transform to the flux time series, we decompose the total variance (strength) of the signal into the power density, P_ν, for each Fourier frequency value, ν, to describe the signal (see van der Klis, 1989, for a detailed explanation of the Fourier techniques applied to X-ray variability studies). In this way it is possible to identify the characteristic timescales (frequencies) of the variability present in the light curve.

The power density spectrum is created by dividing the X-ray light curve into chunks of equal time duration and calculating the Fourier transform of each of the segments. The power density spectra of the segments are very noisy, and to reduce the variance, power spectra are averaged together, generally into one power density spectrum per observation. Defining T and δt, the length of the X-ray light curve segments and the time resolution, respectively, the power density spectrum extends from $\nu_{min} = 1/T$ Hz and $\nu_{max} = 1/(2\delta t)$ Hz (Nyquist frequency). The frequency resolution is defined as $\delta\nu = 1/T$.

Periodic signals, such as pulsation in accreting X-ray pulsars, appear as single frequency-bin spikes, while aperiodic signals cover several frequency elements. If a feature covers a broad range of frequencies in the Fourier power density spectrum, it is usually called *broadband noise*, while a narrow-peaked

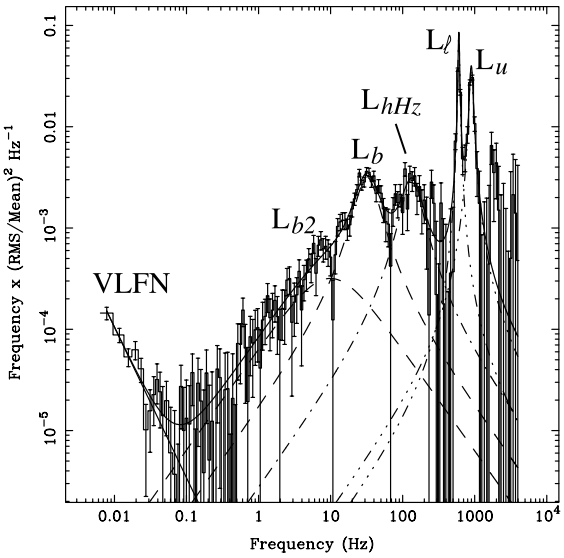

Figure 1.2: Representative averaged power density spectrum of the neutron-star LMXB 4U 1608–52, where noise (VLFN), low-frequency QPOs (L_{b2}, L_b, L_{hHz}) and kHz QPOs (L_l and L_u) are present. Figure adapted from van Straaten et al. (2003).

feature is defined as *quasi-periodic oscillation* (QPO). Figure 1.2 shows a representative PDS of the neutron-star LMXB 4U 1608–52, which presents different variability components such as, noise (VLFN), low-frequency QPOs (L_{b2}, L_b, L_{hHz}) and kHz QPOs (L_l and L_u; van Straaten et al., 2003). Following Belloni et al. (2002), the power density spectrum of LMXBs can be well described as the superposition of several Lorentzian components. Signals modelled with a Lorentzian component are characterised by three parameters: centroid frequency, ν, the quality factor $Q = \nu/FWHM$ where $FWHM$ is the full-width at half-maximum, and the fractional rms, which gives a measure of the modulated flux as a fraction of the total source flux.

Kilohertz quasi-period oscillations in neutron-star LMXBs

Kilohertz quasi-periodic oscillations (kHz QPOs) are the fastest variability so far observed in X-ray binaries. Since their discovery in 1996 (van der Klis et al., 1996; Strohmayer et al., 1996), kHz QPOs have been detected in more than 30 neutron-star LMXBs (see van der Klis, 2006, for a review). Most of these sources show two simultaneous kHz QPOs, usually called the lower and the upper kHz QPO. Figure 1.3 (left panel) shows the two simultaneous kHz QPOs observed in the neutron-star LMXB 4U 1608–52 (Mendez et al.,

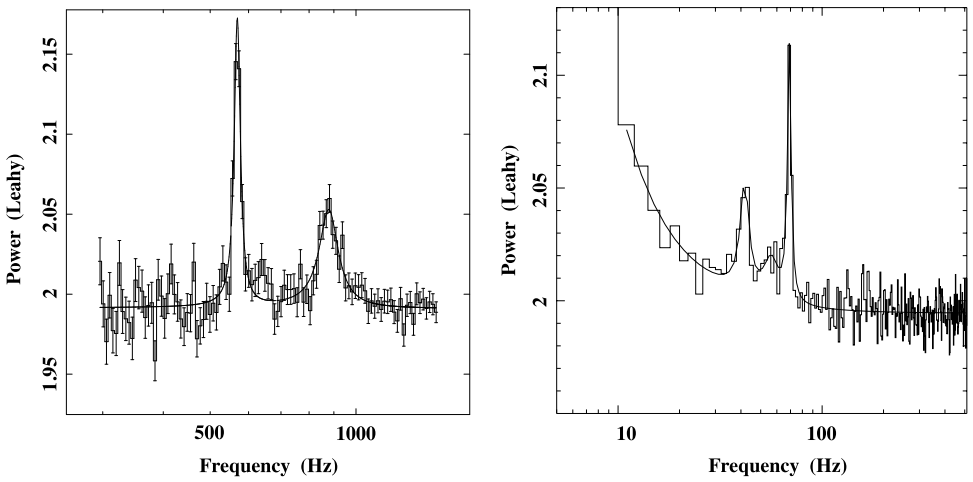

Figure 1.3: Twin kHz QPOs in the neutron-star LMXB 4U 1602–52 (left panel), and high-frequency QPOs in the black-hole LMXB GRS 1915+105 (right panel). Figures adapted from Mendez et al. (1998) and Strohmayer (2001b), respectively.

1998). The frequency of the kHz QPOs changes with time, probably driven by changes of the mass accretion rate, $\dot{M}$ (Miller et al., 1998a). Figure 1.4 shows the dynamical power spectrum of the NS LMXB 4U 1728–34 (Méndez, 2001), in which the kHz QPO frequency (dark feature in the plot) changes over about 100 Hz during the observation.

Systematic analysis of kHz QPO properties (Jonker et al., 2000; van Straaten et al., 2000; Méndez et al., 2001; Homan et al., 2002; Di Salvo et al., 2003; Barret et al., 2005a,b,c; Altamirano et al., 2005; Barret et al., 2006; Méndez, 2006; Sanna et al., 2010) showed that the lower kHz QPO is in general narrower (more coherent), and has a lower fractional rms amplitude, than the the upper kHz QPOs (see Barret et al., 2005a; Méndez, 2006, for more details). Even though none of the models proposed so far has been able to fully explain all the kHz QPO properties, the close correspondence between the typical dynamical timescales of matter orbiting a few kilometres above the surface of a ~ 1.4 solar mass and ~ 15 km neutron star and the kHz QPOs characteristic frequencies make this phenomenon one of the few potential tools to investigate general relativity in the strong-field regime.

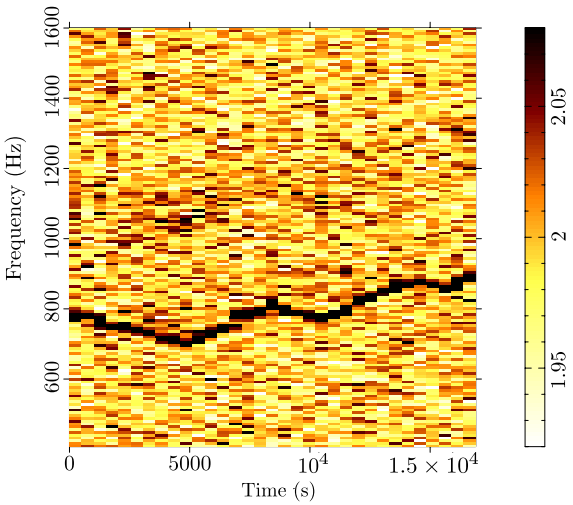

Figure 1.4: Dynamical power spectrum of the NS LMXB 4U 1728–34. The x-axis represents time (starting from the beginning of the observation), the y-axis is the Fourier frequency, and the colours indicate the power in each bin. The dark feature that varies in frequency between ~ 800 and ~ 900 Hz is one the kHz QPO detected. Figure adapted from Méndez (2001).

High-frequency quasi-period oscillations in black-hole LMXBs

The fastest quasi-period oscillations in black-hole (BH) systems have been observed in the frequency range between 40 and 500 Hz (Morgan et al., 1997; Remillard et al., 1999; Cui et al., 2000; Strohmayer, 2001a,b; Miller et al., 2001; Homan et al., 2001; Remillard et al., 2002b,a; Homan et al., 2003; Remillard & McClintock, 2006; Altamirano & Belloni, 2012; Belloni et al., 2012). Figure 1.3 (right panel) shows two simultaneous high frequency QPOs detected in the black hole system GRS 1915+105 (Strohmayer, 2001b). Contrary to the kHz QPOs in NS systems, these QPOs usually occur at fixed frequency values. This signals are very weak, and only a small number of detections are available in the literature. Similar to the kHz QPOs, this phenomenon constitutes a promising way to detecting effects of general relativity in the strong field regime, however it is still not clear whether the same mechanism is responsible for both types of QPOs in NS and BH systems.

QPO models

Here I briefly describe some of the models that have been proposed to explain the kHz and high-frequency QPOs.

Relativistic precession models. In these models the frequencies of the QPOs are associated with the fundamental frequencies of geodesic motion of clumps of gas around the compact object (Stella & Vietri, 1998). The frequencies considered are the general relativistic orbital frequency, ν_ϕ, the radial epicyclic frequency, ν_r, and the vertical epicyclic frequency, ν_θ. Stella & Vietri (1998) identify the upper kHz QPO frequency with the orbital frequency ν_ϕ at the inner edge of the accretion disc, the lower kHz QPO frequency with the periastron precession frequency, $\nu_{per} = \nu_\phi - \nu_r$, and the low-frequency QPO with the nodal precession frequency, $\nu_{nod} = \nu_\phi - \nu_\theta$. This model is very predictive, as the frequency relations basically depend only on the parameters of the compact object (mass and angular momentum) and general relativity.

Relativistic resonance models. These models are based on the resonance of the fundamental frequencies that may occur at particular radii in the disc, where some of these frequencies are commensurable to each other or with the spin frequency. Different resonances have been proposed in the past, e.g., a resonance at radii where ν_r/ν_ϕ equals 1/2 or 1/3 (Kluzniak & Abramowicz, 2001), or where $\nu_r/\nu_\theta = 2/3$ (Kluzniak & Abramowicz, 2002), that where $\nu_\phi - \nu_r = \nu_{spin}$ or $\nu_{spin}/2$ (Wijnands et al. 2003; see also Kluźniak et al. 2004 for other resonances involving the spin frequency). All the resonant frequencies are predicted to scale with the mass of the compact object (Kluźniak et al., 2004), and if the resonant mechanism is identified, both the mass and the angular momentum can be constrained. Relativistic resonance models predict constant QPO frequencies, although modified versions of these models allow tuneable frequencies (e.g., Abramowicz et al., 2003; Rebusco, 2004).

Beat-frequency models. In these models one of the kHz QPOs originates from the interaction between the spin frequency of the neutron star and the accretion disc. Miller et al. (1998b) proposed that the lower kHz QPO comes from the interaction between clumps of matter orbiting at the sonic radius and a pulsar-like beam sweeping the inner edge of the accretion disc at the spin frequency of the NS. When illuminated, radiation drag extracts angular momentum from a clump in the disc, which quickly accelerates radially inwards increasing the amount of matter accreting onto the NS surface. As a consequence of that, the radiation from the NS surface shows a modulation at a frequency equal to the orbital frequency at the sonic radius minus the NS spin frequency. Similarly, in the *magnetospheric beat-frequency model* (Alpar & Shaham, 1985; Lamb et al., 1985; Lamb, 1991) the NS spin frequency interacts with clumps orbiting just outside the magnetosphere. These models only work for neutron-star systems, moreover they require some sort of azimuthal structure in the disc that interacts with the pulsar-like beam at the NS spin.

1.2.2 Spectral analysis

X-ray energy spectrum

The energy spectrum of X-ray binaries is the superposition of photons emitted in a broad energy range, that originates in various regions of the system (e.g., accretion disc, corona, boundary layer) from different mechanisms (e.g., viscous stress, Compton scattering, etc). In order to extract information on the physical origin of the emitting components and the geometry of the system, we fit the energy spectrum with spectral models, usually by means of χ^2 fit statistic. Although this method gives the possibility to estimate directly values of physical quantities of the system, it strongly depends upon the models used. This leaves the possibility of having a so called *model degeneracy*, for which the energy spectrum can be described equally well (statistically speaking) by models that express very different physical scenarios.

The energy spectrum of LMXBs is typically described by two main component: a soft, thermal component peaking near 1-2 keV that originates from the accretion disc, and a hard component extending from few keV up to tens or even hundreds of keV, which probably originates in the corona. For neutron-star LMXBs, a third component is added to model the energy spectrum: a soft, thermal component, slightly hotter than the accretion disc that, originates from the neutron-star surface or the boundary layer. Emission from the accretion disc is usually described as the superposition of blackbody spectra emitted from the different disc annuli (multi-colour disc blackbody; Mitsuda et al., 1984), with blackbody temperatures following the temperature profile of the standard accretion disc (Shakura & Sunyaev, 1973). The hard component has been explained as the result of the Compton up-scattering of the soft photons emitted by the disc by the highly energetic electrons (tens to hundreds keV) that form the corona (Sunyaev & Truemper, 1979; Sunyaev & Titarchuk, 1980), and is usually modelled as a power-law-like component. The neutron-star surface/boundary layer emission is generally modelled with a single blackbody peaking at around 5-6 keV (e.g., Gilfanov & Revnivtsev, 2005), however a thermal Comptonization component has also been proposed (Titarchuk, 1994).

Besides the emission components mentioned before, these systems emit the so called *reflection spectrum*. The reflection spectrum originates as the result of the accretion disc being irradiated by highly energetic X-ray photons, such as the photons emitted by the corona. This spectrum is the superposition of backscattered radiation, fluorescence, Auger effect and recombination emission generated in the accretion disc (e.g., Fabian et al., 1989; Ross & Fabian, 1993), which consists of a structured continuum plus a complex line spectrum. The

characteristic features of the reflection spectrum are: The Compton hump (at 20–40 keV) which is the signature of the Compton recoil at high energies, and an iron emission line (in the energy range between 6 and 7 keV, depending on the ionisation state of the disc) due to fluorescence.

The reflection spectrum is expected to occur mostly around the compact object, in which most of the X-ray emission comes from the accretion disc. Matter in the inner edge of the accretion disc is rapidly rotating, reaching velocities up to a few tenths of the speed of light, hence the reflection spectrum is believed to be modified due to Doppler shifts, Doppler broadening, and gravitational redshift (e.g., Fabian et al., 1989; Laor, 1991). The left panel of Figure 1.5 shows these effects at work in a schematic way. At each radius of the accretion disc, emission coming from matter moving away from (red-shifted) and towards (blue-shifted) the observer produces a double-peak line profile. Near the compact object, where matter approaches relativistic orbital velocities, special relativistic aberration (i.e., the beaming of the emission in the direction of motion) enhances the blue peak over the red. In addition to that, the line profile is also gravitationally redshifted due to the strong gravitational field near the compact object. Summing the line emission profiles from all radii in the disc gives the final broadened and skewed line profile shown in the bottom panel of Figure 1.5. As the accretion disc approaches the compact object, gravitational effects become stronger extending the red wing to lower energies, and leading to a broader iron line profile. The correlation between the iron line profile and the inner radius of the accretion disc can be used to estimate properties of the compact object such as the angular momentum of the compact object if the inner radius of the disc extends down to the ISCO (e.g., Fabian et al., 1989; Laor, 1991), or to constrain the radius of the neutron star if its radius is larger than the ISCO. The line profile also depends strongly on the angle between the accretion disc and the line of sight: For a disc seen almost face-on the Doppler effect is negligible and the line profile is symmetric, although aberration and gravitational effects still make the profile rather broad. The right panel of Figure 1.5 shows the residual of the iron emission line in the NS LMXB 4U 1636–53, when fitting the iron line with a relativistic line model and setting the normalisation to 0.

Doppler and relativistic effects are not the only mechanisms that can shape the broad and asymmetric iron line profile. Other mechanisms such as Compton broadening due to scattering in the disc corona (Misra & Kembhavi, 1998; Misra & Sutaria, 1999), or relativistic optically-thick wind outflows (Laming & Titarchuk, 2004) have been proposed to explain the iron line properties.

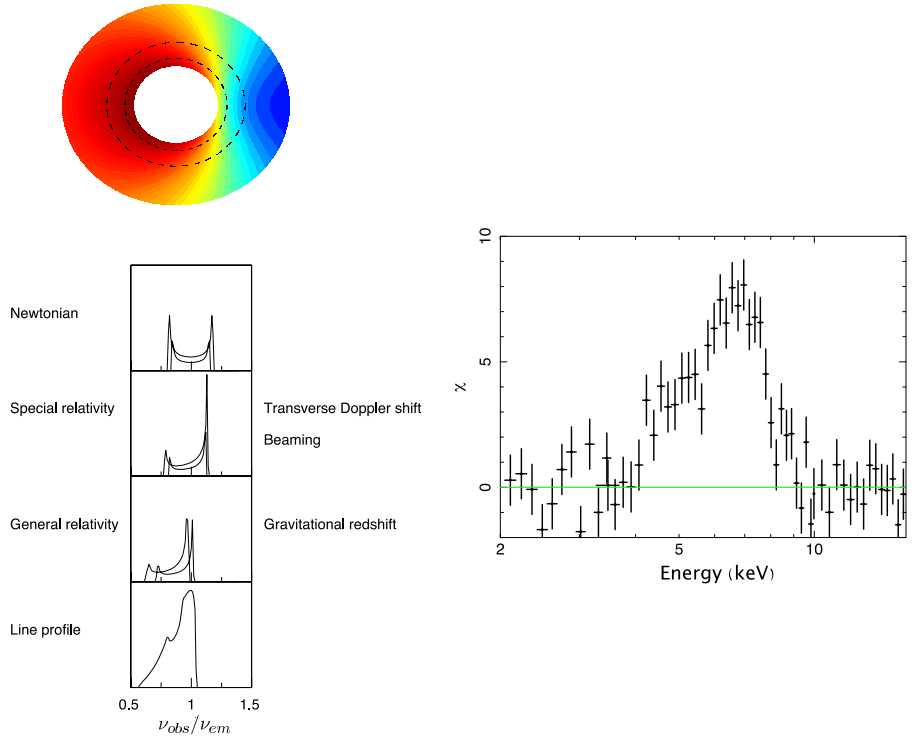

Figure 1.5: On the left I show a schematic representation of the relativistic broadening mechanism of an emission line around a compact object (Figure taken from Fabian & Ross 2010). The upper panel shows the symmetric double-horned profiles from two narrow annuli (dotted circles in the schematic accretion disc drawn above) on a non-relativistic disc. The second panel represents the transverse-Doppler shifting, as well as the relativistic beaming effect. The third panel shows the gravitational redshift. The bottom panel shows the final broad and skewed line profile after integrating over all disc radii. The plot on the right shows the residuals of the iron emission line in the NS LMXB 4U 1636–53, when fitting the iron line with a relativistic line model and setting the normalisation to 0.

X-ray colours

An alternative approach to investigate the energy spectrum of LMXBs is the so called *colour analysis*. Compared with the spectral modelling, this method has the advantage to be model independent and it is more sensitive to short timescale variations of the properties of the system. The colour analysis is

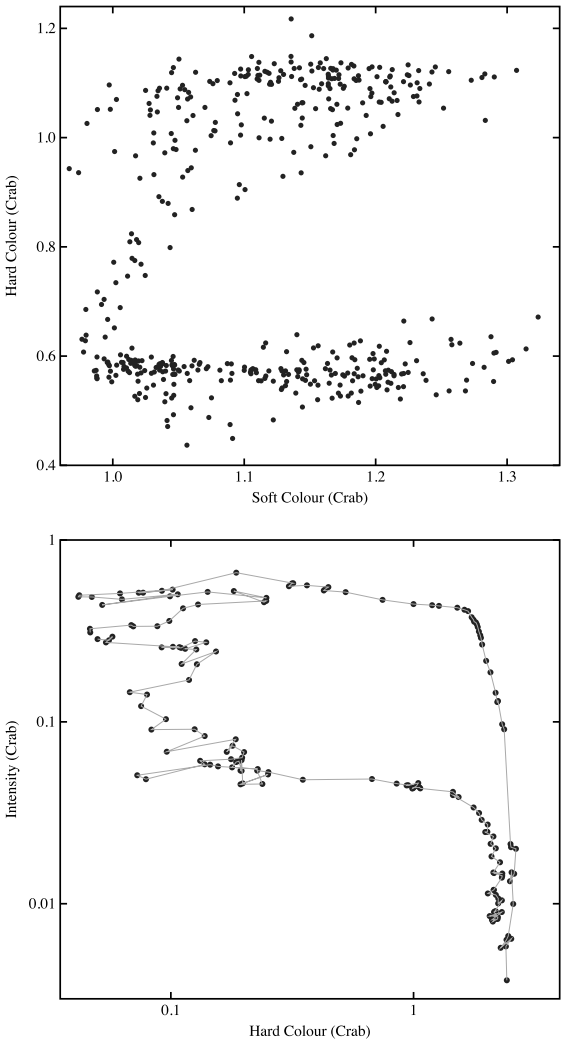

Figure 1.6: Colour-colour diagram of the NS LMXB 4U 1608–52 (upper panel), and hardness-intensity diagram of the 2007 outburst of the BH LMXB GX 339–4 (bottom panel). Each point represents the average colours and intensity within an observation.

performed by means of colour-colour and intensity-colour diagrams, where a colour is defined as the X-ray count rate ratio in two energy bands, while the intensity is just the X-ray count rate in one energy band. Small variations on the definition of the energy bands are usually applied when studying neutron star or black hole systems, to take into account the different spectral variability.

In this thesis, I always calculate X-ray colours using the Standard 2 PCA data (see Section 1.3.1) from the Rossi X-ray Timing Explorer. For neutron-star systems I define soft and hard colour as the 3.5–6 keV / 2–3.5 keV and 9.7–16 keV / 6–9.7 keV count rate ratio, respectively. I also define the intensity as the 2–16 keV count rate. For black hole systems (see Chapter 4), I only define one colour and the intensity per observation; the hard colour is the 6–10 keV / 3.2–6 keV count rate ratio, and the intensity is the count rate in the 3.2–19 keV energy band. To account for the gain changes of the proportional counter units (PCUs) (Jahoda et al., 2006) as well as differences in the effective area between the PCUs, I normalise colours and intensity values by the Crab Nebula (which I use as a standard candle) colours (see Kuulkers et al., 1994; van Straaten et al., 2003).

Based on the pattern traced on the colour-colour diagram and the correlated variations of the X-ray spectral and rapid X-ray variability properties, neutron-star LXMBs are classified as Z and atoll sources (Hasinger & van der Klis, 1989). The differences between the two classes are likely due to qualitatively different inner flow configurations (e.g., structure of the accretion disc, boundary layer, absence or presence of the corona, jets). The position of the source in the colour-colour and hardness-intensity diagram likely reflects the mass accretion rate (e.g., van der Klis et al., 1990). Figure 1.6 shows an example of colour-colour diagram for the neutron-star LMXB 4U 1608–52 (atoll source; upper panel) and a hardness-intensity diagrams from an outburst of the black-hole LMXB GX 339–4 (bottom panel).

1.3 X-ray telescopes

Here I briefly describe the characteristics and the capabilities of the X-ray satellites that provide the data used in this thesis.

1.3.1 Rossi X-ray Timing Explorer

The Rossi X-ray Timing Explorer (RXTE, Bradt et al., 1993) was launched on December 30, 1995 from the Cape Canaveral Air Station in Florida. After 16 years of uninterrupted work, on January 5 2012, RXTE was decommissioned.

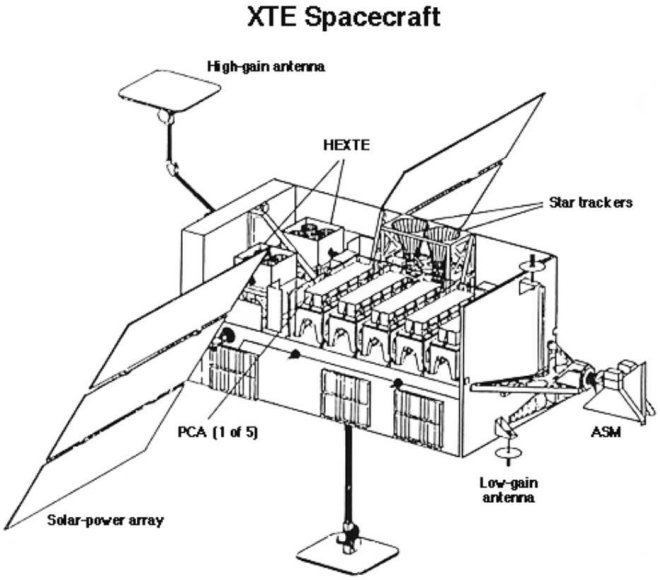

Figure 1.7: Schematic illustration of the RXTE spacecraft, with instruments labeled.

The satellite was equipped with three main instruments, namely the All Sky Monitor (ASM; Levine et al., 1996), the Proportional Counter Array (PCA; Zhang et al., 1993; Jahoda et al., 2006), and the High-Energy X-Ray Timing Experiment (HEXTE; Gruber et al., 1996; Rothschild et al., 1998). The ASM observed the long term (from hours to years) behaviour of the brightest X-ray sources, covering ∼80% of the sky every 90 minutes. The ASM operated in the 1.5–12 keV energy range, with a spatial resolution of $3' \times 15'$, and a time resolution of 18 seconds. In the past 16 years, the ASM followed more than 300 X-ray sources, for which the long term light curves are still available in the ASM database (`http://xte.mit.edu/ASM_lc.html`). This instrument did an excellent work on discovering outbursts from transient sources and state transitions in persistent sources, which were used to quickly trigger follow-up observations with other instruments and satellites.

HEXTE consisted of 2 clusters each containing four scintillation counters, for a total collecting area of ∼1600 cm^2. This instrument was sensitive in the 15–200 keV energy range, with energy resolution of ∼15% at 60 keV, and a time resolution of 10 μs.

The PCA was an array of five proportional counter units (PCUs) that covered the 2–60 keV energy range with an energy resolution of ∼18% at 6 keV. The key feature of the PCA was the ∼1 μs time resolution that, combined with a collecting area of 6500 cm^2, made this instrument extremely suitable

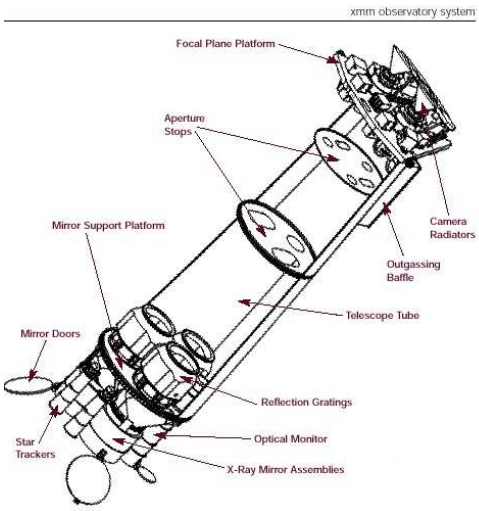

Figure 1.8: Schematic illustration of the XMM-Newton spacecraft, with instruments labeled.

for high-resolution timing studies. Both pointed instruments aboard RXTE, HEXTE and PCA, were co-aligned and had a field of view of ∼1 square degree.

1.3.2 XMM-Newton

The X-ray Multi-Mirror Mission (XMM-Newton) is part of the European Space Agency's Horizon 2000 programme. It was launched on December 10, 1999 from Europe's Spaceport in Kourou into a highly eccentric orbit with ∼48 hour period. The satellite is equipped with three X-ray telescopes, each of which contains 58 Wolter-type concentric mirrors, for a total combined collecting area of 4300 cm^2. At the focus of each set of mirrors there is a charge-coupled device (CCD) based European Photon Image Camera (EPIC). Two of the three EPIC instruments use Metal Oxide Semi-conductor (MOS) CCD array (Turner et al., 2001), while the other is an array of pn CCD (Strüder et al., 2001). The EPIC cameras operate in the energy range 0.1–15 keV, with the possibility to perform extremely sensitive imaging observations over the 30 arcmin field of view, with moderate spectral resolution ($E/\Delta E \sim 20$–50). All EPIC CCDs operate in photon counting mode with a fixed, mode-dependent, frame read-out. Depending on the data acquisition set up, the EPIC cameras allow different observational modes. For this thesis we use data collected from the EPIC pn camera operating in timing mode (Chapter 5). This mode is suitable for bright sources and it allows a high-speed read out of the CCD. In

timing mode, however, the spatial information is lost because one dimension of the CCD is collapsed into one pixel. The advantage of this observational mode is that it reduces the pileup effect, which appears when more than one photon hit the same pixel of the CCD within one read-out cycle.

Besides the EPIC cameras, XMM-Newton carries the Reflection Grating Spectrometers (RGS; den Herder et al., 2000), which allow high-resolution ($E/\Delta E \sim 100$–500) spectroscopy in the 0.3–2.1 keV energy range, and the Optical Monitor (OM; Mason et al., 2001) which consists of a 30 cm telescope providing coverage between 170 nm and 650 nm of the central 17 squared arcmin region of the X-ray field of view.

1.4 Outline of this thesis

In this thesis I study some specific properties of the accretion flow in low-mass X-ray binaries.

In Chapter 2, I focus on the properties of kHz QPOs in the neutron star LMXB XTE J1701–462. This is one of the few sources so far discovered that during an outburst showed (beyond any doubt) spectral and timing characteristics both of the Z (high-luminosity state) and atoll type (low-luminosity state). KHz QPOs detected in the same frequency range in the two states show significantly different properties such as the strength of the signal (fractional rms) and coherence. If the QPO frequency is a function of the radius in the accretion disc in which it is produced, our results suggest that in XTE J1701–462 the coherence and rms amplitude are not uniquely related to this radius. Here I argue that this difference is instead due to a change in the properties of the accretion flow around the neutron star.

In Chapter 3, I analyse the origin of the time variation of the kHz QPOs in the neutron-star LMXB 4U 1636–53. Using the lower kHz QPO, I measure the rate at which the QPO frequency changes as a function of the QPO frequency itself. Assuming that the kHz QPO reflects the Keplerian frequency at the inner edge of the accretion disc, my results support a scenario in which the inner part of the accretion disc is truncated at a radius that is set by the combined effect of viscosity and radiation drag.

In Chapter 4, I present the the results of the analysis of a large database of X-ray observations of 22 galactic black-hole transients with RXTE throughout its operative life. Here I run a semi-automatic homogeneous search for high-frequency (100 - 1000 Hz) QPOs, of which several cases were previously reported in the literature. After taking into account the number of independent trials, I obtain 11 significant detections from two sources only: XTE J1550-564 and GRO J1655-40. I discuss also these results in comparison with

kHz QPO in neutron-star X-ray binaries and the prospects for future timing X-ray missions.

In Chapter 5, I study the properties of the broad iron emission line in the X-ray spectra of six observations, simultaneously taken with XMM-Newton and RXTE, of the neutron-star LMXB 4U 1636–53. Here I fit the line profile with a set of phenomenological models including symmetric as well as relativistically-broadened profiles, and a relativistically smeared ionised reflection model. The aim of the analysis is to constrain the radius of the accretion disc where the iron line originates, as well as the variation of the line properties with the source state. From this analysis I conclude that even though the iron line profile is consistent with being symmetric, the large line breadth still requires the relativistic broadening mechanism. Furthermore, I find that properties of the line, such as the inner disc radius, emissivity index and line energy do not show any particular trend with respect to the source state.

In Chapter 6, I investigate the hypothesis that both the broad iron line and the frequency of the kHz QPOs in neutron-star LMXBs can provide independent measures of the inner radius of the accretion disc, using the XMM-Newton and RXTE simultaneous observations of the LMXB 4U 1636–53. To do so, I combine the inner-radius estimates from the iron line reported in Chapter 5 and those from the upper kHz QPOs detected simultaneously, under the assumption that they reflect the orbital frequency at the inner edge of the accretion disc. Here I find that the actual values of the inner radii inferred from kHz QPOs and iron lines, in four observations, do not lead to a consistent value of the neutron star mass, suggesting that either the kHz QPO or the iron emission line interpretation does not apply for this system.

2 The kilohertz quasi-periodic oscillations during the Z and atoll phases of the unique transient XTE J1701–462

— Andrea Sanna, Mariano Méndez, Diego Altamirano, Jeroen Homan, Piergiorgio Casella, Tomaso Belloni, Dacheng Lin, Michiel van der Klis and Rudy Wijnands —

MNRAS, 2010, 408, 622

Abstract

We analysed 866 observations of the neutron-star low-mass X-ray binary XTE J1701–462 during its 2006-2007 outburst. XTE J1701–462 is the only example so far of a source that during an outburst showed, beyond any doubt, spectral and timing characteristics both of the Z and atoll type. There are 707 RXTE observations ($\sim$ 2.5 Ms) of the source in the Z phase, and 159 in the atoll phase ($\sim$ 0.5 Ms). We found, respectively, pairs of kilohertz quasi-periodic oscillations (kHz QPOs) in 8 observations during the Z phase and single kHz QPO in 6 observations during the atoll phase. Using the shift-and-add technique we identified the QPO in the atoll phase as the lower kHz QPO. We found that the lower kHz QPO in the atoll phase has a significantly higher coherence and fractional rms amplitude than any of the kHz QPOs seen during the Z phase, and that in the same frequency range, atoll lower kHz QPOs show coherence and fractional rms amplitude, respectively, 2 and 3 times larger than the Z kHz QPOs. Out of the 707 observations in the Z phase, there is no single observation in which the kHz QPOs have a coherence or rms amplitude similar to those seen when XTE J1701–462 was in the atoll phase, even though the total exposure time was about 5 times longer in the Z than in the atoll phase. Since it is observed in the same source, the difference in QPO coherence and rms amplitude between the Z and atoll phase cannot be due to neutron-star mass, magnetic field, spin, inclination of the accretion disc, etc. If the QPO frequency is a function of the radius in the accretion disc in which it is produced, our results suggest that in XTE J1701–462 the coherence and rms amplitude are not uniquely related to this radius. Here we argue that this difference is instead due to a change in the properties of the accretion flow around the neutron star. Regardless of the precise mechanism, our result shows that effects other than the geometry of space time around the neutron star have a strong influence on the coherence and rms amplitude of the kHz QPOs, and therefore the coherence and rms amplitude of the kHz QPOs cannot be simply used to deduce the existence of the innermost stable circular orbit around a neutron star.

2.1 Introduction

It is now more than 13 years ago that kilohertz (kHz) quasi-periodic oscillations (QPOs) were discovered (van der Klis et al., 1996; Strohmayer et al., 1996) in neutron star (NS) low-mass X-ray binary (LMXB) systems. Interest in this phenomenon remains high because of the close correspondence between kHz QPO timescales and typical dynamical timescales of matter orbiting close to a NS. For this reason, kHz QPOs are potential tools to probe general relativity in the strong-gravitational field regime (van der Klis, 2005), and constrain the NS equation of state (Miller et al., 1998a).
Since the launch of the Rossi X-Ray Timing Explorer (RXTE) in 1995, kHz QPOs have been detected in about 30 NS LMXBs (for a review see van der Klis, 2005). Most of these sources show two simultaneous kHz QPOs, usually called the lower and the upper kHz QPO, with frequencies that can drift as a function of time in the range 250-1200 Hz (van der Klis, 2004a). Studies of these kHz QPOs show that QPO frequencies are related to other properties of the source; e.g. on short time-scales (within a day or less) QPO frequencies are well correlated with the intensity of the source, whereas on long timescales this correlation breaks down and intensity-frequency diagrams show the so-called "parallel tracks" (Méndez et al., 1999). The frequencies of the kHz QPOs correlate also with the position of the source in the colour-colour diagram, and with parameters of spectral components used to describe the X-ray spectrum of these sources (Wijnands et al., 1997; Méndez & van der Klis, 1999; Kaaret et al., 1999; Di Salvo et al., 2001). Nevertheless, it is still unclear which physical parameters drive the QPO frequency, although there are indications that mass accretion rate, $\dot{m}$, plays a key role (Miller, Lamb, & Cook, 1998a). Several models have been proposed to explain the kHz QPOs (e.g., Miller et al., 1998b; Stella & Vietri, 1998; Abramowicz et al., 2003), as well as the connection between high-frequency QPOs and other time variability usually present in power density spectra (for a review of variability at low frequencies see van der Klis, 2001). Despite these efforts, there is still no single model that is able to explain in a self-consistent way all the QPO properties.
KHz QPOs are characterised by three parameters: centroid frequency ν, quality factor $Q = \nu/FWHM$, where $FWHM$ is the full-width at half-maximum of the QPO, and fractional rms amplitude. Systematic analyses of these kHz QPO properties have been done for a large number of sources (e.g. Jonker et al., 2000; van Straaten et al., 2000; Di Salvo et al., 2001; Méndez et al., 2001; Homan et al., 2002; van Straaten et al., 2002; Di Salvo et al., 2003; Barret et al., 2005a,b,c; Altamirano et al., 2005; Méndez, 2006; Barret et al., 2006). Those studies show that, in each source the quality factor and the

rms amplitude of the lower kHz QPO increase with the centroid frequency of the QPO until they reach a maximum value, after which they decrease as the frequency continues to increase (e.g., Méndez, van der Klis, & Ford 2001; Di Salvo, Méndez, & van der Klis 2003; Barret, Olive, & Miller 2005b; see Méndez 2006 for a compilation of results). The upper kHz QPO does not show the same trend; in this case the quality factor usually does not change with the centroid frequency while the rms amplitude stays more or less constant at lower frequencies and then decreases as the frequency increases (van Straaten et al., 2002, 2003; Barret et al., 2005a; Altamirano et al., 2008a).
Barret et al. (2005b) and Barret et al. (2006) interpreted the drop of the quality factor of the lower kHz QPO at high frequencies in the LMXBs 4U 1636–536 and 4U 1608–522 as a signature of the inner disc radius reaching the innermost stable circular orbit (ISCO), and starting from that assumption they estimated the mass and the radius of the compact object in these two systems. However, Méndez (2006) argued against this idea and suggested that the drop of Q and rms in individual sources might be related (at least in part) to changes of the properties of the accretion flow in these systems.
Following those results, here we investigate the properties of the kHz QPOs for the transient NS LMXB XTE J1701–462. This source was detected for the first time on 2006 January 18 with the All-Sky monitor on-board RXTE (Remillard et al., 2006a). As reported by Homan et al. (2007b), Lin et al. (2009b) and Homan et al. (2010), this is the only source so far that showed both Z and atoll behaviour (for more details about the Z and atoll classes see Hasinger & van der Klis, 1989). The luminosity range covered by XTE J1701–462, from Eddington limit to quiescence, gives us a unique opportunity to study kHz QPO properties in different states and, more importantly, at different mass accretion rates in the same system, which could provide vital information to understand the origin and the mechanisms that drive the properties of these QPOs.
In section 2.2 we describe the observations and the data analysis, and in section 2.3 we present our results. In section 2.4 we discuss those results in the context of current ideas concerning the mechanisms behind the kHz QPOs in LMXBs, and in section 2.5 we summarise our conclusions.

2.2 Observations & Data reduction

We analysed all the public data of the LMXB XTE J1701–462 collected with the Proportional Counter Array (PCA) on board of RXTE (Bradt et al., 1993; Jahoda et al., 2006). There are 866 observations of this source in the RXTE archive, for a total exposure time of $\sim$ 3 Ms. During these observations the

Z phase						
Obs ID	L_ℓ			L_u		
	Q_ℓ	rms_ℓ%	ν_ℓ (Hz)	Q_u	rms_u%	ν_u (Hz)
91442-01-07-09	35.3 ± 18.8	1.4 ± 0.2	642.7 ± 3.1	52.8 ± 38.8[1]	< 1.6	932.6 ± 7.9[1]
92405-01-01-02	22.6 ± 11.1	3.4 ± 0.5	615.1 ± 3.8	56.9 ± 28.8	2.9 ± 0.5	944.9 ± 3.7
92405-01-01-04	5.4 ± 2.8[1]	< 3.5	502.4 ± 23.1[1]	10 ± 3	3.1 ± 0.3	760.8 ± 6.4
92405-01-02-03	11.9 ± 6.5	3.0 ± 0.5	623.9 ± 8.3	20.6 ± 11.1	2.7 ± 0.4	911.2 ± 8.4
92405-01-02-05	8.9 ± 6.9	2.7 ± 0.4	595.9 ± 10.1	6.2 ± 1.4	4.1 ± 0.4	850.5 ± 12.4
92405-01-03-05	8.5 ± 2.7	4.6 ± 0.5	612.5 ± 7.7	10.5 ± 3.5	4.6 ± 0.6	917.3 ± 10.6
92405-01-40-04	9.2 ± 3.2	2.8 ± 0.3	650.5 ± 7.1	11.1 ± 3.1	2.9 ± 0.3	911.0 ± 8.6
92405-01-40-05	8.1 ± 2.4	3.0 ± 0.3	637.9 ± 8.6	12.9 ± 3.5	3.0 ± 0.3	919.8 ± 7.6

Table 2.1: Properties of the kHz QPOs detected in the Z phase of XTE J1701–462. Subscript letters u and ℓ denote lower and upper kHz QPOs, respectively. Parameters without errors represent 95% confidence level upper limits. All other errors reported represent 1σ confidence intervals. [1]These parameters are calculated for kHz QPOs with a significance level lower than 3σ (see the text for precise values).

source showed several type-I X-ray bursts that we excluded from our analysis (see Lin et al., 2009a, for a detailed analysis of the bursts).

2.2.1 Timing analysis

To search for kHz QPOs, we created Leahy-normalised power density spectra using Event mode data with $125\mu s$ time resolution covering the full PCA energy band, nominally from 2 to 60 keV. We created Fourier power density spectra from 16-seconds data segments, using 1/4096 s time resolution such that the frequency range is defined from 0.0625 Hz to 2048 Hz. We removed detector drop-outs; no dead-time correction or subtraction of background contribution were done to calculate the power density spectra. We created one averaged power density spectrum for each observation that we visually inspected to search for the presence of QPOs with characteristic frequencies in the range from 200 Hz to 1200 Hz. We found kHz QPOs in 14 out of the 866 observations that we analysed.

Following Homan et al. (2010), we considered that XTE J1701–462 was in the Z phase from its discovery in January 2006 (Remillard & McClintock, 2006) until the end of April 2007 (as reported by Homan et al. 2010, no clear boundary between Z and atoll phase has been found which makes this date just an approximation), when it started to behave as an atoll source until it went into a quiescence state. Using this division, there are 707 observations ($\sim$ 2.5 Ms) of XTE J1701–462 in the Z phase, and 159 observations ($\sim$ 0.5 Ms) in the atoll phase. KHz QPOs were detected in individual observations only in the horizontal branch during the Z phase, and in the lower banana in the atoll

phase of the outburst (see Homan et al., 2010). From 14 observations with kHz QPOs, 8 belong to the Z phase (ObsIDs are reported in Table 2.1) and 6 to the atoll phase (observations: 93703-01-02-04, 93703-01-02-11, 93703-01-02-05, 93703-01-02-08, 93703-01-03-00, and 93703-01-03-02).
A quick analysis of the observations showed clear differences in the properties of the QPOs between Z and atoll phases (see Section 2.3 for a detailed discussion). The QPOs were always weaker and broader in the Z than in the atoll phase. It is well known that the frequency of the kHz QPOs can change over tens of Hz in time intervals of a few hundred seconds (e.g Berger et al., 1996), and this can artificially broaden the QPO in the averaged power spectrum of long observations. Therefore, for each observation in which we found a kHz QPO, we divided the observation in smaller intervals to check if a significant QPO was still present, and whether the QPO frequency was changing. We found that in the Z phase it was not possible to detect a significant kHz QPO in power spectra of intervals shorter than a full observation: In all observations in the Z phase with kHz QPOs the QPOs were weak and broad over short time intervals. Therefore, for the rest of the analysis, for the Z phase we report QPO properties for the average power density spectrum of each observation. In the atoll phase, the kHz QPOs were significantly detected on time intervals shorter than a full observation, and in most cases the frequency was changing in time. Therefore, for the atoll phase, we decided to average power density spectra according to the frequency of the QPO. To do this we produced power density spectra of 16s of data, and averaged up to 15 of these power spectra to get a significant detection of the kHz QPO from which we measured the QPO frequency as a function of time. Finally we averaged power density spectra such that the frequency of the QPO was within a range of 10 Hz to 60 Hz (frequency intervals are reported in Table 2.2). We shifted the frequency scale of all these power density spectra in order to align the frequencies of the QPOs to a constant value and then averaged the power density spectra to create one power density spectrum per selection (see Mendez et al., 1998). We fitted each Z and atoll average power density spectrum in the frequency range 200-1200 Hz using a constant to model the Poisson noise plus one Lorentzian to model the kHz QPO. It must be clarified that, for the atoll phase, the centroid frequencies of the QPOs reported in Table 2.2 are the mean frequencies within the interval selected, and the errors associated are the standard deviations of the selection.
In order to label the QPOs we used the standard convention introduced by Belloni et al. (2002) where each QPO is denoted with the letter L with a subscript that specifies the category. In this particular case we were interested in kHz QPOs so we used L_ℓ and L_u to identify the lower and the upper kHz

QPO, respectively. Following this criterion all the characteristics associated with one QPO have the same label.
We estimated the fractional rms amplitude of QPOs in the atoll phase in different energy bands. For each observation with QPOs we first created power density spectra in 5 different energy intervals: 2-3 keV, 3-6 keV, 6-11 keV, 11-16 keV and 16-25 keV (we stopped at 25 keV because of the lack of sensitivity of the detector above that energy). We shifted and added the power density spectra creating one single power density spectrum for each energy band and we fitted these power density spectra as the atoll power density spectra previously described. To calculate the fractional rms amplitude we calculated the integral power of the Lorentzian and we renormalised it using the source and background count rate (van der Klis, 1997).

2.2.2 Spectral analysis

We calculated X-ray colours and intensity of the source using the Standard 2 mode data. We defined a hard colour as the count rate ratio in the energy bands 9.7-16.0 keV and 6.0-9.7 keV, and the intensity of the source as the count rate in the energy band 2.0-16.0 keV. To obtain the exact count rate in each of these bands we interpolated in channel space.
To correct for the gain changes and differences in the effective area between the proportional counter units (PCUs) as well as differences due to changes in the channel to energy conversion of the PCUs as a function of time, we normalised our colour and intensity by the Crab Nebula values obtained close in time to our observations and per PCU (see Kuulkers et al. 1994 and Altamirano et al. 2008a for details). Finally we averaged the normalised colours and intensities per PCU every 16 seconds using all available PCUs.
We also calculated the source luminosity for all 14 observations containing kHz QPOs. In order to do so, we first created a light curve for each observation, we then checked for X-ray bursts and detector drop-outs, and if any were present we eventually excluded them from the analysis. Using Standard 2 data we extracted energy spectra following the procedures described in the RXTE web page, and we added a 0.6% systematic error in quadrature to each channel. We fitted the energy spectra in Xspec in the energy range from 3 keV to 22 keV using a model consisting of a blackbody and a multi-colour blackbody for the Z observations, while we added also a broken power-law with the break energy fixed at 20 keV to fit the atoll observations (see Lin et al., 2009b). These model also include absorption from the interstellar medium toward the source and when necessary we added a Gaussian emission line at ~ 6.5 keV. The reduced χ^2 of our fits range from 0.6 to 1.1 (for 36 d.o.f.). From the best-fitting model we calculated the unabsorbed flux in the energy range 2-50 keV,

atoll phase				
Interval	Hz	Q	rms%	ν(Hz)
1	600-660	69.9 ± 17.1	9.8 ± 0.9	640.9 ± 13.5
2	660-700	59.6 ± 15.6	10 ± 1	673.3 ± 14.5
3	700-750	98.2 ± 14.8	9.2 ± 0.5	716.8 ± 6.7
4	750-780	67.1 ± 19.2	11.8 ± 1.2	772.2 ± 4.2
5	780-800	106.9 ± 9.7	9.9 ± 0.3	793.9 ± 5.4
6	800-820	150.3 ± 20.9	8.7 ± 0.4	811.5 ± 6.6
7	820-830	114.9 ± 12.7	9.3 ± 0.4	827.3 ± 2.6
8	830-840	93.4 ± 8.7	8.9 ± 0.3	835.8 ± 2.6
9	840-850	100.6 ± 13.9	7.9 ± 0.4	846.2 ± 2.9
10	850-950	123.9 ± 36.8	6.6 ± 0.7	854.8 ± 4.3

Table 2.2: Properties of the kHz QPOs detected in the atoll phase of XTE J1701–462. Column 2 shows the frequency selections used to create the intervals (see text for details). Column 3, 4 and 5 show the quality factor, the fractional rms amplitude and the frequencies of the kHz QPOs, respectively. All errors represent 1σ confidence intervals.

setting the N_H to zero. and creating an artificial response function for the full energy range 2 keV to 50 keV. We then estimated the luminosity assuming a distance $d = 8.8$ Kpc (Lin et al., 2009a) .

2.3 Results

In Table 2.1 and Table 2.2 we report the quality factor Q, fractional rms amplitude and frequency of the kHz QPOs detected in all the RXTE observations available for XTE J1701–462, from January 2006 to August 2007.
In Table 2.1 we show the properties of the kHz QPOs during the Z phase. The significance level of these QPOs ranges between 3.2σ and 6σ, except for L_u in observation 91442-01-07-09 and L_ℓ in observation 92405-01-01-04 which have, respectively, significances of 2.4σ and 2.3σ. (The significances of kHz QPOs are given as the ratio of the integral of the power of the Lorentzian used to fit the QPO divided by the negative error of the power. As shown by Boutelier et al. 2010, this probably underestimates the true significance of the QPOs). For these two kHz QPOs we report upper limits. During the Z phase the lower and upper kHz QPOs show similar quality factors, on average around 15; also the fractional rms amplitude of the two QPOs is similar, between $\sim 1.4\%$ and 4.5%.

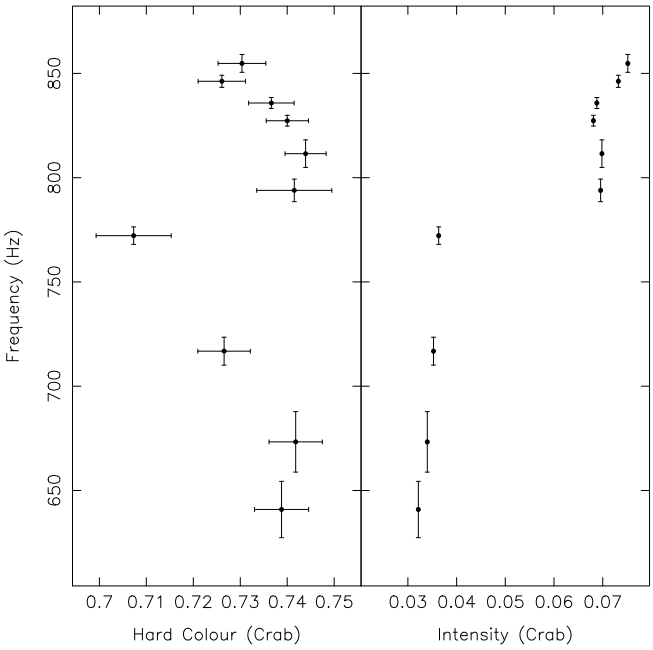

Figure 2.1: Left panel shows the frequency of the QPOs in the atoll phase of XTE J1701–462 as a function of the hard colour of the source. Right panel show the frequency of the QPOs as a function of the intensity of the source.

In Table 2.2 we report the properties of the 10 QPOs detected in the frequency-selected intervals in the atoll phase. These QPOs have significances between 5σ and 15σ. The QPO frequency varies from 640 Hz to 860 Hz; the quality factor changes from about 60 up to 150. The fractional rms amplitude ranges from about 7% to 12%.

2.3.1 QPO identification

While for the Z phase it is easy to label the QPOs, for the atoll phase the identification is not straightforward since there we found just one QPO in each observation. A quick inspection of the values in Table 2.2 shows similar QPO properties between different intervals, which indicates that in all cases we are probably dealing with the same QPO. To progress further we compared Q and rms values with those of other LMXBs where two simultaneous kHz QPOs have been studied (Wijnands et al., 1997, 1998; Jonker et al., 1998; Barret et al., 2005a,b, 2006); the coherence and rms amplitude are similar to

those of the lower kHz QPO in other atoll sources.
According to Méndez et al. (1999) and Belloni et al. (2007), lower and upper kHz QPOs in atoll sources follow two different tracks in the frequency-hardness diagram. Lower kHz QPOs are found when the source has low hard colour and the centroid frequency does not seem to be correlated with hard colour (as the frequency changes the hard colour changes slightly in a restricted range). On the contrary, upper kHz QPOs are found where the source has high hard colour that decrease as the QPO frequency increases (see Figure 3 in Belloni et al., 2007). In Figure 2.1 we plot the QPO frequency as a function of the hard colour and intensity of the source. All points are concentrated within a narrow hard colour range, from 0.7 to 0.75, while the frequency ranges from 640 Hz to 860 Hz. The fact that the hard colour changes within a restricted range while the frequency moves in a range of about 200 Hz resembles what Belloni et al. (2007) show concerning the lower kHz QPO behaviour in the atoll source 4U 1636–53. This further supports our identification of the kHz QPOs in the atoll phase as lower kHz QPOs.
In order to understand the frequency-hardness diagram, we plot in the right panel of Figure 2.1 the QPO frequency as a function of the source intensity. It is apparent from the graph that the data are divided into two different tracks characterised by intensity values which differ by a factor of ~ 2. That trend resembles the so-called "parallel tracks" phenomenon which has been seen in many LMXBs (see e.g. Méndez et al., 1999). Although the points in Figure 2.1 are the result of frequency selection, it turns out that all the QPOs we combined to make the intervals from 1 to 4 and from 5 to 10 on Table 2.2 are concentrated in a time interval, respectively, of about 1 day and less than half a day. Moreover, those two groups are separated by more or less 4 days, which means the points in the right panel of Figure 2.1 can in fact reflect the "parallel tracks" phenomenon.

We notice that QPOs at the highest intensities correspond to the ones with the highest frequencies in the frequency-hardness diagram, while QPOs at the lowest intensities correspond to those with the lowest frequencies in the frequency-hardness diagram. This can be interpreted as "parallel tracks" in the frequency-hardness diagram. A similar trend was seen in the LMXB 4U 1636–53 (see Figure 2 in Di Salvo, Méndez, & van der Klis, 2003).
To search for a second (possibly weaker) kHz QPO in the atoll phase we apply the shift-and-add method (Mendez et al., 1998). As we described in section 3.2, first we fit the centroid frequency of the kHz QPO in each individual atoll power density spectrum, then we shift all the power spectra such that the kHz QPO frequencies are aligned at the same value. Finally we average all the data into a single power density spectrum which we fit with a constant

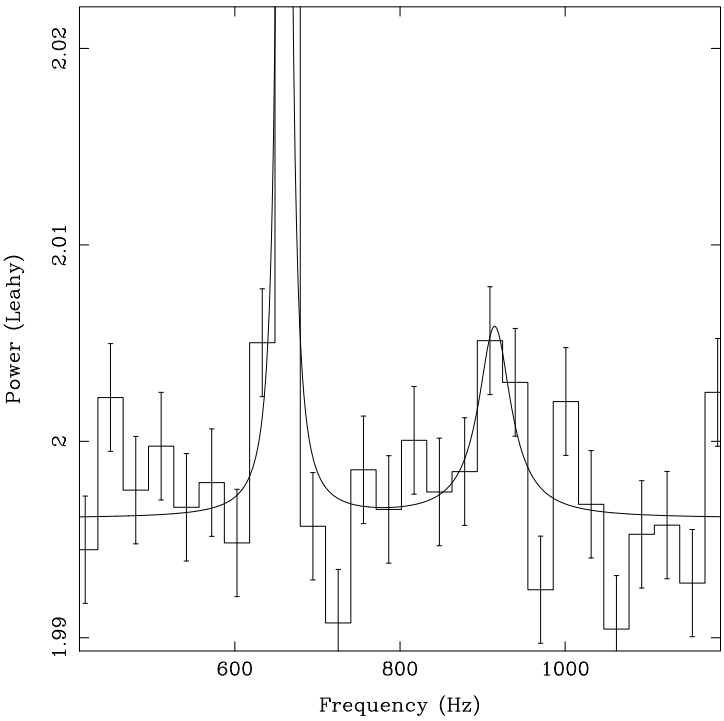

Figure 2.2: Power density spectrum of all the atoll observation where QPOs are detected. This power spectrum is the result of the shift-and-add method. Two kHz QPOs are visible, the one at lower frequency (30 σ significant) was the one originally used to shift and add the power spectra, while the one at higher frequencies (3.1σ significant, single trial) appears as result of the application of the method.

plus Lorentzian component for each QPO. This method corrects the frequency drift in time of the kHz QPOs, increasing their signal to noise ratio and their significance. If the second kHz QPO is at a (more or less) fixed distance from the first, this method adds all the data in a way that increases the significance of the second QPO, which may then become detectable.
The result of this procedure is presented in Figure 2.2, which shows two simultaneous kHz QPOs, the one at lower frequency is the kHz QPO which we already knew, while the second one becomes detectable as a result of the shift-and-add method. The significance level of the second, upper, kHz QPO is 3.1σ, which implies a marginal detection. Note however that the frequency difference between the kHz QPOs is 258 ± 13 Hz, which is consistent with the value in the Z phase (see Table 2.1 and Homan et al. 2007a) and therefore there are no other trials involved in estimating this significance. As a result of this analysis, taking into account all the caveats, we find a pair of simultaneous kHz QPOs in the atoll phase of the XTE J1701–462 which strengthens our previous suggestion that the strong kHz QPOs detected in this phase are always the lower kHz QPO.
As described in section 3.2, we calculate the fractional rms amplitude of the atoll QPOs in 5 different energy bands, 2-3 keV, 3-6 keV, 6-11 keV, 11-16 keV and 16-25 keV, respectively. We find fractional rms amplitudes of less than 10.9%, 6.9 ± 0.3, 11.4 ± 0.2, 17.5 ± 1.2 and less than 21.3%, respectively (upper limits are given at 95% confidence). Those results, as already noticed in other sources (see Berger et al. 1996), show that the strength of the variability increases as the energy increases.

2.3.2 Amplitude and coherence of the kHz QPOs in the Z and atoll phases

Figure 2.3 shows the values of the QPO quality factor as a function of frequency. Black points represent measurements in the atoll phase while grey points are measurements in the Z phase. For the Z phase, empty and filled square symbols represent, respectively, lower and upper kHz QPOs. From the plot we notice a few interesting aspects: 1) QPOs in the atoll phase are on average 10 times more coherent than in the Z phase; 2) in the atoll phase Q increases as the frequency increases, reaching a maximum value of about 150 at ~ 810 Hz; within the errors the behaviour is consistent with what has been observed in other sources (see Barret et al., 2005a). No such trend seems to be present in the Z phase; 3) comparing lower kHz QPOs in both phases it is clear that in the Z phase the lower kHz QPO appears at lower frequencies than in the atoll phase; 4) there is an overlap in frequency around 640 Hz

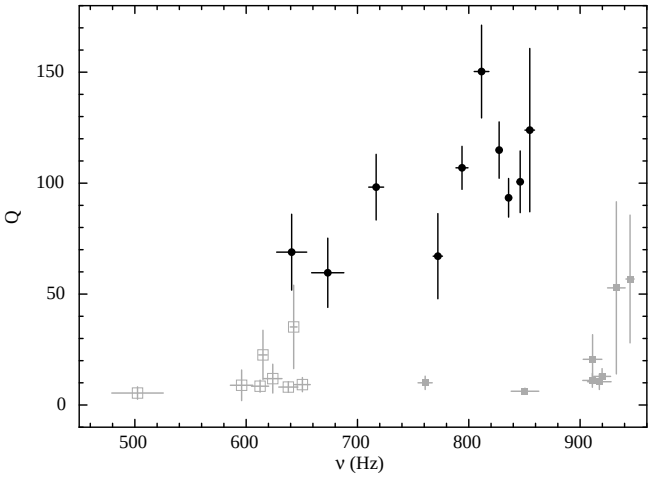

Figure 2.3: Quality factor Q as a function of the QPO centroid frequency for XTE J1701–462. Black points represent QPOs in the atoll phase, and grey points represent QPOs in the Z phase. Empty and filled squares indicate lower and upper kHz QPOs, respectively. The two values of the coherence at frequencies ∼500 Hz and ∼930 Hz correspond to kHz QPOs with significances 2.3σ and 2.4σ, respectively (see text).

between Z and atoll QPOs with a significant mismatch in Q.

Figure 2.4 shows the QPO rms fractional amplitude as a function of frequency. As in Figure 2.3, black points denote measurements in the atoll phase, while grey points are QPOs in the Z phase. The rms amplitude of the lower kHz QPO in the atoll phase remains more or less constant around 10% as the QPO frequency increases from 640 Hz to 780 Hz and then drops rapidly at $\sim$ 800 Hz. There is no evidence of a similar trend for the rms of the lower or upper kHz QPOs in the Z phase. As already noticed for the quality factor, the rms amplitude values show a clear difference between the atoll and Z phases: The lower kHz QPOs amplitude in the atoll phase is on average a factor of 2 higher than in the Z phase; this difference is also apparent in the region where atoll and Z QPOs overlap in frequency between 620 Hz and 660 Hz.

We test whether we may have missed any significant kHz QPO in our analysis. We calculate upper limits to the fractional rms amplitude in frequency ranges where we did not find kHz QPOs. To do so we take two power density spectra, one for each source phase, where no kHz QPOs were found. We fit those power density spectra using a model consisting of a constant to fit the Poissonian noise, and a Lorentzian to fit the QPO with fixed values for the centroid frequency and the quality factor Q. We fit the data and we estimate

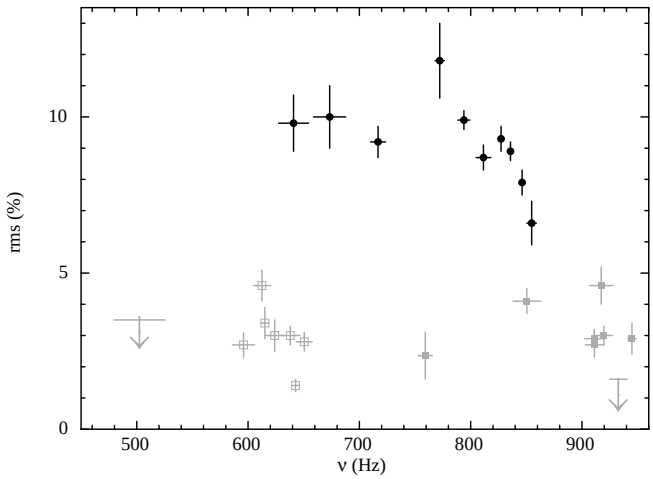

Figure 2.4: Factional rms amplitude as a function of the QPO centroid frequency for XTE J1701–462. Black points represent QPOs in the atoll phase, and grey points represent QPOs in the Z phase. Empty and filled squares indicate lower and upper kHz QPOs, respectively. Arrows correspond to 95% confidence level upper limits.

the upper limit of the amplitude of the Lorentzian using $\Delta\chi^2 = 2.7$, which corresponds to 95% confidence level. We repeat the same procedure shifting gradually the frequency of the Lorentzian to higher values until we cover the frequency range of interest.

For the analysis of atoll observation we use power density spectra of 256s, comparable to the time intervals over which we detected kHz QPOs in the atoll phase. We use two different quality factors, $Q = 50$ and $Q = 20$, which are comparable to the values we found for the kHz QPOs at low frequencies (see Table 2.2). We find upper limits to the fractional rms amplitude that vary within the range 2.7%-5.2% and within the range 3%-7%, respectively for $Q = 20$ and $Q = 50$. From these values it appears that the rms amplitude of the lower kHz QPO in the atoll phase should decrease at frequencies lower than 640 Hz. This would be in agreement with the typical rms-frequency trend observed in most of the LMXBs (Méndez et al., 2001; van Straaten et al., 2000, 2002, 2003; Di Salvo et al., 2001, 2003; Barret et al., 2005a).

For the Z observation, we estimate the upper limits to the amplitude of a kHz QPO with typical atoll properties within short time intervals to check whether we could have missed such a QPO during the analysis. We calculate the upper limits in the frequency range 650-940 Hz assuming a kHz QPO with $Q = 100$ and setting 3 values of the integration time, 128, 256 and 512 seconds. We find

that the upper limits to the fractional rms amplitude vary between 1% and 4% for 128 seconds of integration time, between 0.8% and 4% for 256 seconds, and between 0.4% and 3.4% for 512 seconds. From this we conclude that if a kHz QPO with $Q = 100$ and fractional rms amplitude similar to what we found for the atoll kHz QPOs was present in the Z observations, we would have detected it significantly in intervals as short as 128s.

2.4 Discussion

The transient source XTE J1701–462 is so far the only accreting neutron-star X-ray binary that changed from a Z into an atoll source during an outburst. Here we found that the properties of the kHz QPOs in XTE J1701–462 in the atoll and Z phases are significantly different: At approximately the same frequency (about 640 Hz), the coherence of the kHz QPOs is a factor of 2 larger, and the rms amplitude is a factor of 3 larger, in the atoll than in the Z phase (see Figure 2.3 and Figure 2.4, respectively). Furthermore, out of 707 observations in the Z phase, there is no single one in which the kHz QPOs have a coherence or rms amplitude similar to those seen when XTE J1701–462 was in the atoll phase, even though the total exposure time was about 5 times longer in the Z than in the atoll phase. If the kHz QPOs reflect the motion of matter in the accretion disc, and the QPO centroid frequency is related to the radius in the accretion disc where this motion takes place, our results show that, at least in XTE J1701–462 there is no unique relation between the radius of the disc at which the QPO is produced and the coherence and rms amplitude of the QPO.

It was already known that the kHz QPOs are broader and weaker in Z than in atoll sources (see Méndez, 2006, for a compilation), but this is the first time that the same trend is observed in a single source. This result conclusively excludes things like neutron-star mass, magnetic field, spin, inclination of the accretion disc, etc., as the cause of this trend, since these parameters cannot change on time scales of one and half year. As we discuss below, the most likely reason for the difference of QPO coherence and rms amplitude between the Z and atoll phase in XTE J1701–462 is a change in the properties of the accretion flow around the neutron star where the QPOs are produced. Despite the the lack of information about the precise mechanism, our result shows that effects other than the geometry of space time around the neutron star have a strong effect on the QPO properties. If, as suggested by Barret et al. (2005a,c), the ISCO affects the coherence and rms amplitude of the kHz QPOs, our result shows that there are other mechanisms that should also be taken into account to explain the trend seen in the data. For instance, in

XTE J1701–462 the coherence and rms amplitude differ by a factor of ~ 3 to 10 between the Z and atoll phases similar, for instance, to the change of coherence and rms amplitude that has been proposed to be due to the ISCO in 4U 1636–53 Barret et al. (2005b).
Méndez (2006) found that the the behaviour of the coherence and rms amplitude of the kHz QPOs in individual sources is similar to the behaviour of the maximum coherence and maximum rms of the kHz QPOs as a function of the luminosity in a sample of 12 NS-LMXBs. It is interesting to test to what extent this luminosity relation holds for the Z and atoll phases of XTE J1701–462, which are well separated in luminosity. In Figure 2.5 we combine the data points from the Z and atoll phases of XTE J1701–462 with those of the 12 NS-LMXBs studied by Méndez (2006).
The upper and the lower panels show respectively the maximum quality factor and the maximum rms amplitude of the lower kHz QPO for 13 sources as a function of the luminosity of the source in the 2-50 keV range, normalised by the Eddington luminosity, $L_{Edd} = 2.5 \times 10^{38}$ erg s^{-1}, corresponding to a neutron star of 1.9 $M_{\odot}$ accreting gas with cosmic abundance. As it is apparent from the plots, XTE J1701–462 follows the trends already traced by the other sources; moreover the coherence of the kHz QPOs in the Z phase fill the gap between the atoll sources in the left-hand side and the Z sources in the right-hand side of the graph, strengthening the correlation. (Notice, however that the luminosity of XTE J1701–462 could be uncertain by up to a factor of ~ 2, Lin et al. 2009b).
Besides differences of the kHz QPOs properties between Z and atoll sources, Figure 2.5 shows also a trend of both Q and rms amplitude within the atoll sources. This is noticeable in the lower panel of Figure 5 of Méndez (2006), where the maximum coherence and maximum rms amplitude of the lower kHz QPO are plotted vs. each other. From that plot it is apparent that the two quantities both in Z and atoll sources follow the same correlation (see Méndez, 2006). This suggests that there is a single mechanism behind this trend. Our observations of XTE J170–462 in the Z and atoll phase are in line with this.
We can qualitatively explain how it is possible to find high rms amplitudes of kHz QPOs at energies where the contribution of the disc is insignificant. As reported by Berger et al. (1996), the rms amplitude of the lower kHz QPO in the LMXB 4U 1608–52 increases with energy up to 20% (fraction of the total emitted flux) at energies around 30 keV, significantly above the energy range where the accretion disc contributes to the X-ray spectrum (see also Méndez et al., 2001; Gilfanov et al., 2003; Altamirano et al., 2008a). If the kHz QPOs are produced in the accretion disc, this must imply the presence of a mechanism that amplifies the variability at different energy bands. Some mechanisms

have been proposed for this: Lee & Miller (1998) found that oscillations of the density and temperature of the Comptonizing medium can reproduce the rms amplitude behaviour of the lower kHz QPO in the atoll source 4U 1608–52. Gilfanov et al. (2003), from the analysis of the Z source GX340+0, suggest that QPOs are related to the contribution of the boundary layer emission to the total source emission. Gilfanov & Revnivtsev (2005) found that as $\dot{m}$ increases from the horizontal branch to the flaring branch along the Z-shaped track in the colour-colour diagram of GX 340+0, the contribution of the boundary layer decreases. If we combine the results of Gilfanov, Revnivtsev, & Molkov (2003) and Gilfanov & Revnivtsev (2005), and we apply them to the case of XTE J1701–462, we would expect the boundary-layer contribution to be stronger in the atoll phase than the in Z phase. To verify this, we used the spectral analysis of XTE J1701–462 done by Lin et al. (2009b); their Figures 14 and 15 show the spectral fitting results, respectively, of the atoll and the Z phase. From their Figure 14 we notice that in the atoll phase the blackbody (BB) component used by Lin et al. (2009b) to fit the boundary-layer emission becomes dominant, while the emission from the disc (fitted with a multi colour disc blackbody, MCD) becomes negligible. Comparing this with their Figure 15, we found that the fractional contribution of the boundary-layer emission in the atoll phase is higher than in the Z phase, which is in agreement with the results of Gilfanov, Revnivtsev, & Molkov (2003), and can also explain the fact that we found stronger kHz QPOs in the atoll phase than in the Z phase. If this is correct, we should expect that most of the variability concentrates in the energy band where the boundary-layer emission peaks. From Figure 14 of Lin et al. (2009b), the BB temperature is about 2 keV, which implies that the peak of the boundary-layer emission is at about 10 keV. According to the results shown in the previous section, the atoll fractional rms amplitude increases as the energy increases, up to about 20% in the energy band 16-25 keV. We test whether the fractional rms amplitude we found above 10 keV is compatible with the fractional contribution of the boundary layer emission to the total emission of the source. From the spectral fits shown by Lin et al. (2009b, see their Figure 12 panel "atoll SS"), the BB contributes more than 30% of the total emission in the 10-25 keV band, which means that the picture where the amplitude and coherence of the kHz QPOs are driven by the boundary layer is still consistent at those energies. Further studies should address the fact the kHz QPOs are only detected over narrow regions in the colour-colour diagram.

Adding all these together, we suggest a possible scenario to describe the behaviour of the properties of the kHz QPO. Mathematically a Lorentzian (which is usually used to model quasi-periodic oscillations) is the Fourier transform

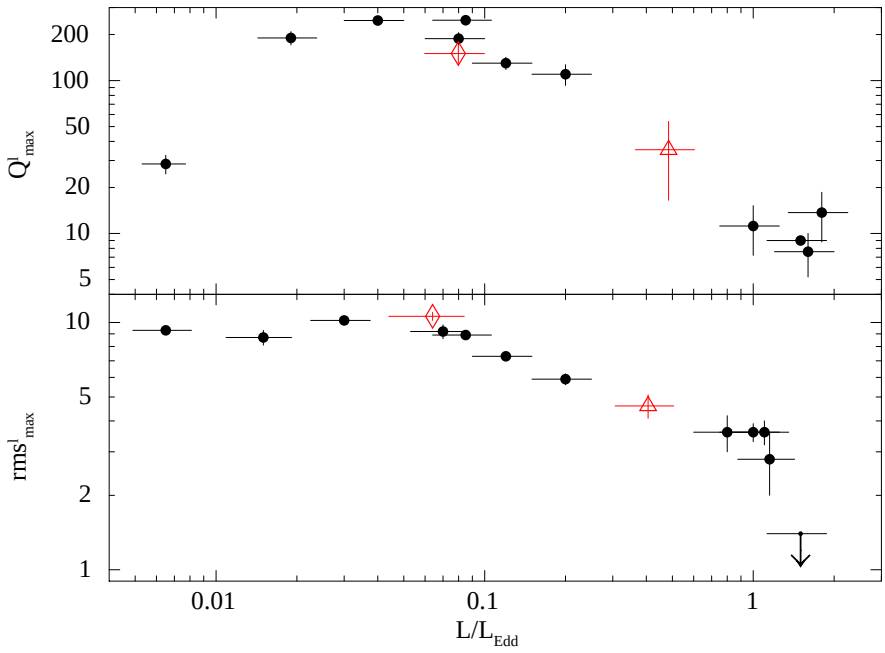

Figure 2.5: Upper panel: the maximum fractional rms amplitude of the lower kHz QPO for a sample of 12 sources (filled circles, see Table 1 Méndez 2006 for the source names) plus XTE J1701–462 as a function of the luminosity of the source. The diamond and the triangle represent, respectively, measurements in the atoll and the Z phase. Lower panel: the maximum quality factor of the lower kHz QPO for the same sources mentioned above as a function of the luminosity of the source. The symbols are the same as in the upper panel. The luminosity is in units of the Eddington luminosity for a 1.9 $M_{\odot}$ neutron star.

of an exponentially damped sinusoid signal, $A\,e^{-t/\tau}sin(2\pi\nu t+\phi)$, where A is the amplitude of the signal, τ is the life time of the variability, ν is the frequency of the oscillation, and ϕ is an arbitrary phase. Starting from this mathematical expression we can build a qualitative mechanism to describe the behaviour of the quality factor and the rms of the kHz QPO. Most of the models proposed to explain the kHz QPOs, consider the disc as the most probable location where those QPOs are generated (e.g., Miller et al., 1998b). Under this assumption, the above expression could represent the oscillator that generates the QPO in the disc and sets its frequency ν. Since the rms amplitude of kHz QPOs depends on energy, we should introduce an energy-dependent amplification factor $B(E)$ which should be physically related to the mechanism which generates high-energy photons. For example, this could be related to the properties of the Comptonizing medium (Lee & Miller, 1998) or to the contribution of the boundary-layer emission to the total emission of the source (Gilfanov et al., 2003; Gilfanov & Revnivtsev, 2005). The life time τ drives the QPO width, and as the amplitude, also this could be energy dependent. Additionally, we should consider that each process that amplifies the variability could also modify the life time of the variability. Just to give an example, if the QPO is created in the disc, and later on the QPO photons interact with matter in the corona, the final width of the QPO will be the result from the combination of the two process. In our model this would imply a lifetime for the QPO $1/\tau_{tot} = (\tau_{disc} + \tau_{cor})/(\tau_{disc} * \tau_{cor})$. With these considerations, the modulated flux in the kHz QPO could be described by the expression $B(E)*A\,e^{-t/\tau_{tot}}\,sin(2\pi\nu t+\phi)$. This simple expression describes the rms amplitude and coherence of the QPO in terms of the quantities $B(E)$ and τ_{tot}, which in turn could depend on the properties of the boundary layer. The above expression would reproduce the behaviour of the rms amplitude and coherence if, for instance, $B(E)$ and τ_{tot} depended upon mass accretion rate, $\dot{m}$, such that $B(E)$ and τ_{tot} decreased as $\dot{m}$ increased. The previous description does not resolve however the issue of which processes are involved, or what the key mechanisms are that create or amplify the QPO signal. Nevertheless, this qualitative explanation provides a starting point to build a realistic model to explain the kHz QPO properties.

For most of the considerations in this paper we assumed that the only kHz QPO in the atoll phase is the lower kHz QPO. Although it is very unlikely (see section 2.3), if it instead was the upper kHz QPO, one would have to explain the fact that in the frequency range, from 740 Hz to 860 Hz, the atoll kHz QPOs show Q and rms values significantly different than those of the Z phase kHz QPOs (Figures 2.3 and 2.4).

From the INTEGRAL catalog (INTEGRAL general reference catalog, Version

30) we found no other sources within 1 square degree of the position of XTE J1701–462. The closest source reported (about 2.3 degrees away from XTE J1701–462) is the Gamma-ray source 2EGS J1653-4604 that does not show X-ray emission. Krauss et al. (2006) observed XTE J1701–462 in outburst with the Chandra's High-Resolution Camera (HRC-S) in timing mode and they did not find evidence of other sources in the HRC-S field of view ($6' \times 90'$). Swift observations with the X-ray telescope as well as XMM Newton observations of XTE J1701–462 did not show other sources, respectively within $23.6' \times 23.6'$ and $30' \times 30'$. Finally we checked the RXTE Galactic Bulge scans archive and we found that with a spatial accuracy of $15'$ no sources have been detected in a 1 square degree area from the XTE 1701-462 position. The evidence just discussed indicates that most likely the outburst observed by RXTE was due to a single source, XTE J1701–462, switching from Z to atoll.
Another interesting aspect to mention is the mismatch of the frequency of the lower kHz QPOs between the two different phases of the source. It is clear from Tables 2.1 and 2.2 and Figures 2.3 and 2.4 that Z phase lower kHz QPOs are in the range $500 - 660$ Hz, while in the atoll phase the lower kHz QPOs are in the frequency range $640 - 860$ Hz. Although a similar effect has been observed when one compares other atoll and Z sources (see Méndez, 2006, for a compilation), we have now shown this effect in a single source. Studying the energy spectra in different parts of the colour-colour diagram, Lin et al. (2009b) found that in the Z phase the disc is truncated far from the NS surface and its inner radius could be set by the local Eddington limit, while in the atoll phase the disc extends closer to the NS. Different sizes of the inner radius of the accretion disc could explain the different range of kHz QPO frequencies. However we can not discard the presence of other lower kHz QPOs in the Z phase at frequencies higher than what we found. From the upper limits for the Z phase reported in section 2.3, it is apparent that we are not sensitive enough to detect broad and weak QPOs at high frequencies in that phase.

Conclusions

We studied the properties of the kHz QPOs in the transient source XTE J1701–462, the only source so far that during an outburst underwent a transition from Z to atoll class. We found that:

- Most of the time, when there are kHz QPOs in the Z phase, the power spectrum shows two simultaneous kHz QPOs, whereas in the atoll phase there is only one kHz QPO that we identify as the lower kHz QPO.

- The coherence and fractional rms amplitude of the kHz QPOs are signif-

icantly different between the Z and atoll phases. Atoll lower kHz QPOs show quality factors and fractional rms amplitude, respectively, 2 and 3 times larger than the Z ones in the same frequency range.

- There is no single Z observation in which the kHz QPOs have a coherence or rms amplitude similar to those seen when XTE J1701–462 was in the atoll phase, even though the total exposure time was about 5 times longer in the Z than in the atoll phase.

- The difference in QPO properties cannot be due to quantities like neutron-star mass, magnetic field, spin, inclination of the accretion disc, etc. We suggest that this difference is due to a change in the properties of the accretion flow around the neutron star where the QPOs are produced.

We conclude that, at least in XTE J1701–462 the coherence and rms amplitude of the kHz QPOs are not uniquely driven by the radius in the accretion disc in which QPOs are most probably created.
Our results show that effects other than the geometry of the space time around the neutron star have a strong influence on the QPO properties.

Acknowledgment. This research has made use of data obtained from the High Energy Astrophysics Science Archive Research Center (HEASARC), provided by NASA's Goddard Space Flight Center. This research made use of the SIM-BAD database, operated at CDS, Strasbourg, France and NASA's Astrophysics Data System. MM, DA, TB, PC, and MK wish to thank ISSI for their hospitality. We thank Didier Barret for interesting discussions that helped us improved the presentation. JH gratefully acknowledges support from NASA grant NNX08AC20G. PC acknowledges funding via a EU Marie Curie Intra-European Fellowship under contract no. 2009-237722. TB acknowledges support from grant PRIN-INAF 2008 and from ASI via contract I/088/06/0, and a visitor grant from NWO.

3 The time derivative of the kilohertz quasi-periodic oscillations in 4U 1636–53

— **Andrea Sanna, Mariano Méndez, Tomaso Belloni, Diego Altamirano** —

MNRAS, 2012, 424, 2936

Abstract

We analysed all archival RXTE observations of the neutron-star low-mass X-ray binary 4U 1636–53 up to May 2010. In 528 out of 1280 observations we detected kilohertz quasi-periodic oscillations (kHz QPOs), with $\sim$ 65% of these detections corresponding to the so-called lower kHz QPO. Using this QPO we measured, for the first time, the rate at which the QPO frequency changes as a function of QPO frequency. For this we used the spread of the QPO frequency over groups of 10 consecutive measurements, sampling timescales between 320 and 1600 s, and the time derivative of the QPO frequency, $\dot{\nu}_{\rm QPO}$, over timescales of 32 to 160 s. We found that: (i) Both the QPO-frequency spread and $\dot{\nu}_{\rm QPO}$ decrease by a factor ~ 3 as the QPO frequency increases. (ii) The average value of $\dot{\nu}_{\rm QPO}$ decreases by a factor of ~ 2 as the timescale over which the derivative is measured increases from less than 64 s to 160 s. (iii) The relation between the absolute value of $\dot{\nu}_{\rm QPO}$ and the QPO frequency is consistent with being the same both for the positive and negative QPO-frequency derivative. We show that, if either the lower or the upper kHz QPO reflects the Keplerian frequency at the inner edge of the accretion disc, these results support a scenario in which the inner part of the accretion disc is truncated at a radius that is set by the combined effect of viscosity and radiation drag.

3.1 Introduction

Kilohertz quasi-periodic oscillations (kHz QPOs) are the fastest variability so far observed in neutron star (NS) low-mass X-ray binary (LMXB) systems. These oscillations were first detected (van der Klis et al., 1996; Strohmayer et al., 1996) shortly after the launch of the Rossi X-ray Timing Explorer (hereafter RXTE; see Bradt et al., 1993; Jahoda et al., 2006). Since then, kHz QPOs have been observed in more than 30 neutron star LMXBs (see, e.g., van der Klis, 2005). KHz QPOs are often observed in pairs, usually called lower and upper kHz QPO, with frequencies ranging from a few hundred Hz to more than 1 kilohertz (e.g., van der Klis, 2005, for an extensive review). The fact that the timescale of these oscillations corresponds to the dynamical timescale very close to the NS, makes kHz QPOs potentially one of the few tools nowadays available to directly measure strong-field gravitational effects.

In the past 16 years, several models have been proposed to explain these oscillations, with emphasis in trying to explain the frequency of the QPOs. Almost all models associate the frequency of these oscillations with characteristic frequencies in a geometrically thin accretion disc (e.g., Miller et al., 1998b; Stella & Vietri, 1998). Systematic studies of other properties of kHz QPOs, such as the coherence and the amplitude of the oscillation, are also available for several LMXBs (Jonker et al., 2000; van Straaten et al., 2000; Di Salvo et al., 2001; Méndez et al., 2001; Homan et al., 2002; van Straaten et al., 2002; Di Salvo et al., 2003; van Straaten et al., 2003; Barret et al., 2005a,b, 2006), but not many models explain these other properties (see Miller et al., 1998b; Barret et al., 2006). Some sources show a characteristic dependence of the coherence (defined as $Q = \nu/\Delta\nu$, where ν and $\Delta\nu$ are the centroid frequency and the full width at half-maximum of the kHz QPO, respectively) and the amplitude of those oscillations upon the centroid frequency of the oscillation: Both the coherence and the amplitude of the lower kHz QPO in these sources increase as the frequency increases, and then quickly decrease as the QPO frequency continues to increase. Barret, Olive, & Miller (2006) proposed that the drop of the coherence Q at high frequencies is a direct consequence of the disc approaching the innermost circular stable orbit (ISCO), where the inner edge of the disc gets shattered by the gravitational force of the neutron star. If this interpretation is correct, the drop of the coherence and rms amplitude of the lower kHz QPO at high frequencies would confirm the existence of the ISCO, and it would provide a direct measurement of the mass of the neutron star (Miller, Lamb, & Psaltis, 1998b). However, other non space-time-related interpretations have been proposed to explain the properties of QPOs; e.g., Méndez (2006) suggested that the drop of Q and rms amplitude in individual

sources might be related (at least in part) to changes in the properties of the accretion flow in these systems. This could explain the significantly different properties of the kHz QPOs, respectively, in the high and low-luminosity phase of the outburst of the LMXB XTE J1701–462 (Sanna et al., 2010).

Here we investigate the properties of the kHz QPOs for the NS system 4U 1636–53 by scanning the whole RXTE archive until May 2010. In Section 3.2 we describe the observations and the data analysis, and in Section 3.3 we present our results. In Section 3.4 we discuss our results in the context of current ideas concerning the origin of the kHz QPOs in LMXBs.

3.2 Observations & Data reduction

We analysed all archival observations of the LMXB 4U 1636–53 obtained with the Proportional Counter Array (PCA) on board of RXTE up to May 2010. We used a total of 1280 RXTE observations, which correspond to an exposure time of ~ 3.5 Ms. During these observations the source showed a large number of type-I X-ray bursts that we excluded from our analysis (see, Zhang et al. 2011).

Except for four observations, we used event-mode data with $125\mu s$ time resolution and 64 channels covering the full PCA energy band to produce Fourier power density spectra (PDS), setting the time resolution to 4096 points per second, corresponding to a Nyquist frequency of 2048 Hz. In the four observations in which the event-mode data were not available, we used a combination of binned modes that allowed us to reach the same Nyquist frequency in the PDS. In all cases we selected photons with energies below ∼46 keV (absolute channel 101), with the exception of observation 10072-03-01-00 where we selected photons between channels 24 and 139, and observations 10072-03-02-00 and 10088-01-08-010 where we used the full energy band, because in these cases it was not possible to have simultaneously the same Nyquist frequency and energy selection as in the other observations. We created Leahy-normalised PDS for each 16-seconds data segment. We removed detector drop-outs, but no background subtraction or dead-time correction were applied before calculating the PDS.

We averaged all 16-s spectra within each observation, and we searched for kHz QPOs by fitting the averaged PDS in the frequency range 200-1500 Hz using a constant to model the Poisson noise and one or two Lorentzians to model the QPOs. From each fit, we estimated the significance of the Lorentzian by dividing its normalisation by the negative 1σ error. We considered only features with this ratio larger then 3, and coherence Q larger than 2.

We calculated the X-ray colours and intensity of the source using the Standard

2 data (16-s time resolution and 129 channels covering the entire PCA energy band). We defined soft and hard colour as the count rate ratio in the energy bands 3.5-6.0 keV / 2.0-3.5 keV and 9.7-16.0 keV / 6.0-9.7 keV, respectively. The intensity of the source is defined as the count rate in the energy band 2.0-16.0 keV. To obtain the exact count rate in each of these energy bands we linearly interpolated in channel space, since the energy boundaries of each channel change slightly with time. To correct for gain changes and differences in the effective area between the proportional counter units (PCUs) as well as differences due to changes in the channel to energy conversion of the PCUs as a function of time, we normalised the colours and intensity to those of the Crab Nebula obtained close in time to our observations (see Kuulkers et al. 1994 and Altamirano et al. 2008a for details). Finally we averaged the normalised colours and intensities per PCU for the full observation using all available PCUs.

3.2.1 KHz QPOs Identification

We detected kHz QPOs in 528 out of 1280 observations analysed. Among the observed QPOs, $\sim$84% where detected with a significance larger then 3.5σ, $\sim$72% with a significance larger then 4σ, and $\sim$53% with a significance larger then 5σ. Even though $\sim$16% of the QPOs could be considered only marginally significant (between 3 and 3.5σ), all these QPOs follow the frequency-hardness correlation described below, which adds confidence to the detections. Only 26 observations with QPOs showed two simultaneous high-frequency oscillations. In those cases the QPO identification is trivial because lower and upper kHz QPOs were both present. For all the other observations where we only detected a single QPO peak we had to apply a different method to identify the peak as either the lower or the upper kHz QPO. In Figure 3.1 we plot, for each observation, the centroid frequency of all the kHz QPOs as a function of the hard colour of the source. From the plot it is apparent that, for frequencies below 1000 Hz, the data follow two separate branches. The first branch extends between QPO frequencies of $\sim$ 550 Hz and $\sim$ 950 Hz, with more or less constant hard colour at around 0.65, except for a small deviation at low frequencies where the hard colour increases slightly. The second branch shows a clear anti-correlation between frequency and hard colour. This has been already reported for this source (see Belloni et al., 2007) as well as for other neutron-star systems (e.g., Méndez et al., 1999; Méndez & van der Klis, 1999) and can be used to identify the two different kHz QPOs: Lower kHz QPO at low hard colour, and upper kHz QPO at high hard colour.

In Figure 3.1 we also show the kHz QPOs detected simultaneously per ob-

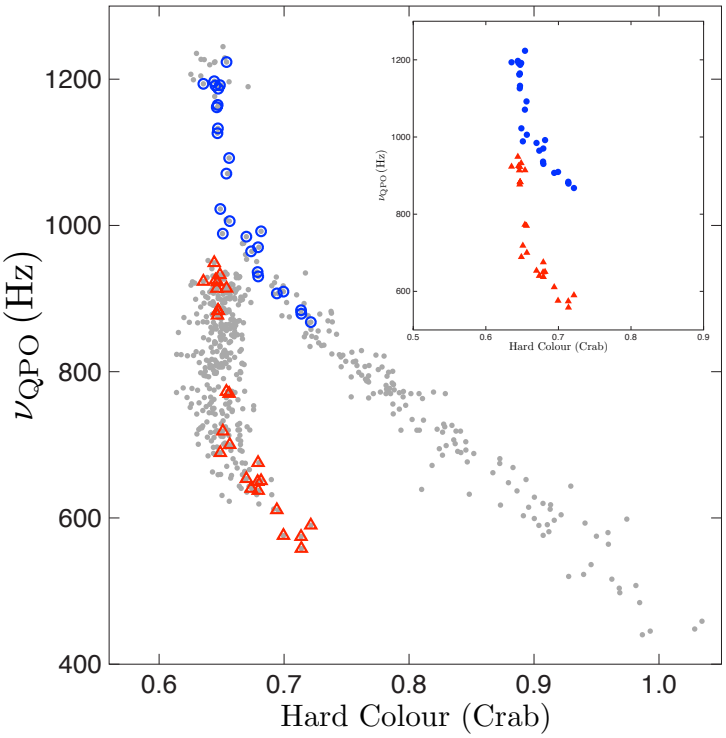

Figure 3.1: Centroid frequency of the kHz QPOs detected in 4U 1636-53 as a function of hard colour. Grey bullets represent the QPOs in observations in which only one kHz QPO is observed. Red triangles and blue circles represent QPOs identified, respectively, as the lower and the upper kHz QPO in observations in which two simultaneous kHz QPOs are detected. For clarity, in the inset we plot only the QPO frequencies of the observations in which two simultaneous kHz QPOs were detected.

servation: Red-empty triangles and blue-empty circles represent, respectively, the lower and the upper kHz QPOs. Those points confirm the correlation previously mentioned between frequency, hard colour and type of QPO. Interestingly, by checking the distribution of the blue circles in Figure 3.1 we can resolve the ambiguity regarding the identification of the QPOs in the region above 1000 Hz, in which the two branches approach each other. To summarise, we detected a total of 357 lower kHz QPOs and 197 upper kHz QPOs. Compared to Belloni et al. 2007, we find that the branch corresponding to the upper kHz QPO extends to higher frequencies at more or less constant hard colour, while the branch corresponding to the lower kHz QPO extends to lower frequencies at higher hard colour.

3.2.2 Variations of the kHz QPO frequency

It is well known that the frequency of the kHz QPOs can change over tens of Hz in time intervals of a few hundred seconds (e.g., Berger et al., 1996), and this can artificially broaden the QPO in the averaged power spectrum of long observations. In order to study frequency variations of the kHz QPOs, we tried to detect kHz QPOs on timescales shorter than the full observation. We found that in observations with only the upper kHz QPO we cannot detect the QPO significantly on timescales shorter than the full observation, whereas we detected the lower kHz QPO on timescales between 32 s and 160 s in about 50% of the observations that showed kHz QPOs, all at significance levels larger than 4σ. For these observations we created dynamical power density spectra (see, e.g., Figure 2 in Berger et al., 1996), and we extracted the frequency evolution as a function of time (hereafter frequency profile). To reduce the influence of the frequency error on the analysis of the frequency variation, we applied a Savitzky–Golay filter (Savitzky & Golay, 1964; Press et al., 1989) to smooth the frequency profile. This method locally fits a polynomial function on a series of values (in our case we used a 4th order polynomial on 6[1] consecutive points), and it provides the first time derivative of the QPO frequency (hereafter frequency derivative) for each measurement.

For each observation we then calculated how much the centroid frequency moved with time by measuring the sample standard deviation (hereafter the spread) using groups of 10 consecutive measurements of the frequency profile. We also used the frequency derivative to evaluate the rate at which the centroid frequency changes on certain timescales.

3.3 Results

In Figure 3.2 we show the spread of the lower kHz QPO frequency as a function of the QPO frequency measured over timescales of 320 and 1600 s. Each point represents the average spread within frequency bins of 5 to 40 Hz, depending on the number of measurements at different frequencies. Notice that the rebin has been applied under the assumption that the spread only depends on frequency.

Figure 3.2 shows that the frequency spread decreases from ~ 7 Hz to ~ 2 Hz as the QPO frequency increases from ~ 650 Hz up to ~ 910 Hz. Above ~ 910 Hz, the data show a marginal increase of the spread to ~ 4 Hz as the frequency increases further up to ~ 930 Hz. The apparent rise of the spread at high frequency is suggested by two points only, which are the average of 13

[1] We varied the number of overlapping points from 4 to 10, but within errors this does not affect the time derivative of the QPO frequency.

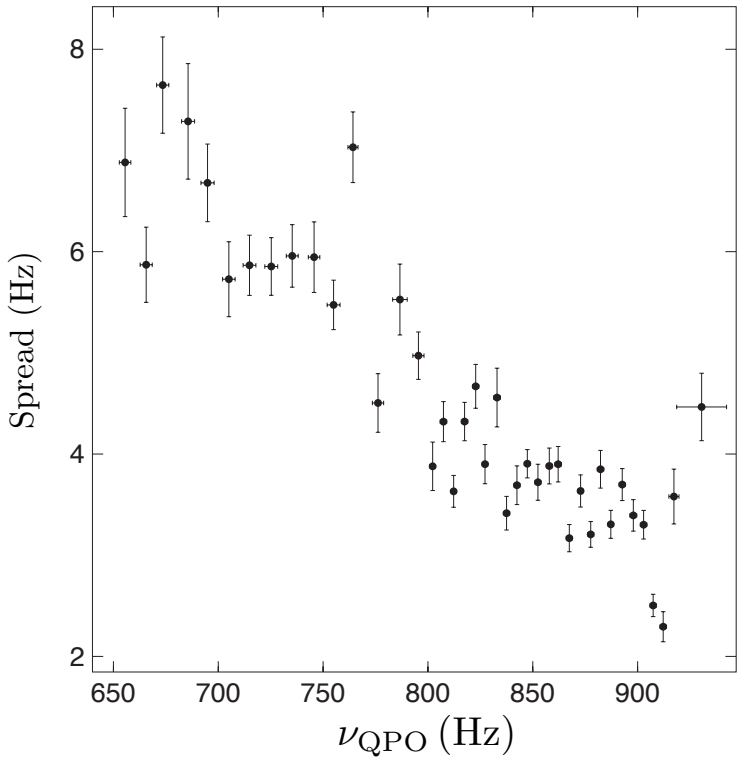

Figure 3.2: Measurements of the frequency spread of the lower kHz QPO in 4U 1636–53 as a function of the QPO centroid frequency. Each point is the average of the QPO-frequency spread at that frequency, corresponding to timescales between 320 s and 1600 s. See section 3.3 for more details.

and 12 measurements, respectively. We fitted the data both with a line and a broken line function, and we carried out an F-test to compare both fits. The F-test probability is 2.2×10^{-2}, indicating that the fit with a broken line is marginally better than a fit with line. We cannot rule out the possibility that this increase is real, but as we discuss below, it could also be (partly) due to a larger contribution of the statistical errors to the QPO frequency in that frequency range.

To take into account the contribution of the statistical errors from the measurements of the frequency on the spread, we subtracted in quadrature the 1-sigma errors from the observed spread (see Vaughan et al., 2003, section 6.1, Eq. 8). We found that the errors of the QPO frequency contribute about 10% of the observed spread at around 650 Hz, whereas this contribution de-

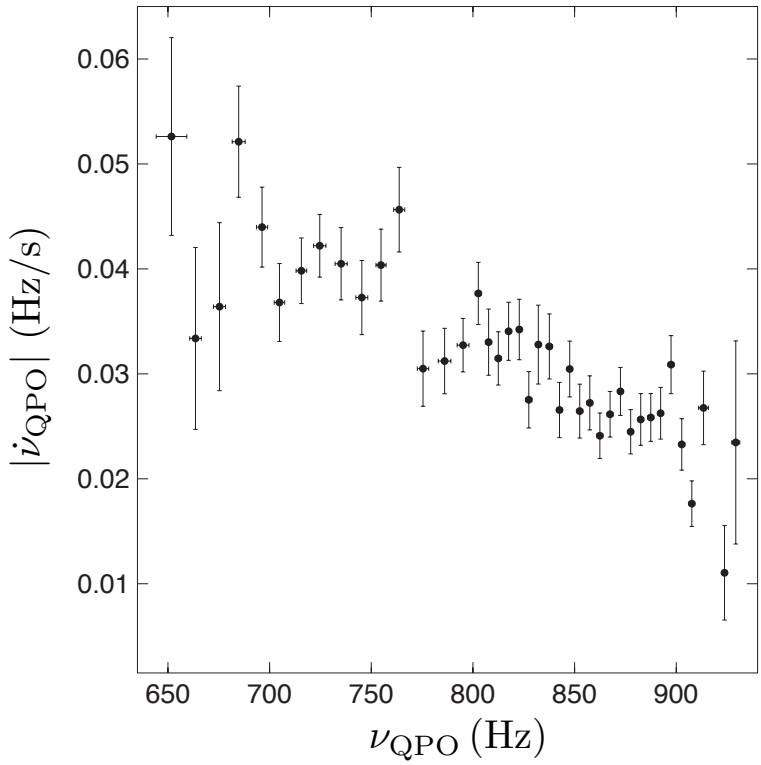

Figure 3.3: Absolute value of the frequency derivative of the lower kHz QPO frequency in 4U 1636–53 as a function of the QPO frequency. Each point is the average value (within a frequency bin) of the frequency derivative of the QPO frequency detected on timescales of 64 s or less. See section 3.2.2 for more details.

creases down to 5% at 850 Hz, and then increases up to 40% at $\sim$ 930 Hz. Although this correction slightly flattens the relation, the overall trend does not change significantly, except that the apparent increase of the spread at the high-frequency end becomes less significant.

The accuracy with which one measures the centroid frequency of the QPO depends on the amplitude and the width of the oscillation (e.g., van der Klis, 1997), which in turn change with QPO frequency (e.g., Barret et al., 2006). In order to verify whether this affects the relation between spread and frequency, we made simulations where we added normally distributed noise to the frequency profile, with standard deviation ranging from 1 to 10 Hz. As expected, the extra noise component tends to flatten the relation, but errors of up to 10 Hz (rms) in the determination of the QPO frequency do not significantly

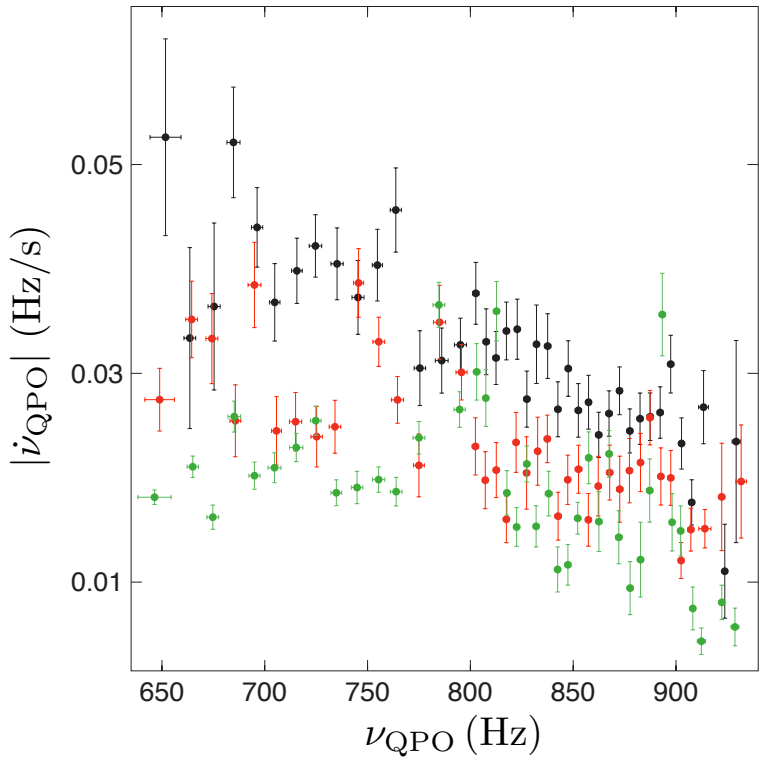

Figure 3.4: Absolute frequency derivative values of the lower kHz QPO in 4U 1636–53 for 3 different timescales. Black points are measurements for QPOs detected on intervals shorter than 64 s. Red points represent detections between 64 s and 160 s, while green points represent measurements of the QPO on intervals of 160 seconds.

change the trend shown in Figure 3.2.

Figure 3.3 shows the absolute value of the frequency derivative of the lower kHz QPO as a function of the QPO frequency. This plot is based on measurements of the QPO frequency on timescales of 64 s or less. Each point represents the average value of the frequency derivative within a frequency bin from 5 to 30 Hz. Similar to what happens with the spread, the frequency derivative decreases as the frequency of the QPO increases, but unlike Figure 3.2, in this case there is no indication of an increase of the frequency derivative above $\sim$ 910 Hz.

In Figure 3.4 we compare the absolute value of the frequency derivative of the lower kHz QPOs detected over three different timescales. Black points represent the frequency derivative of the QPOs measured on timescales of 64

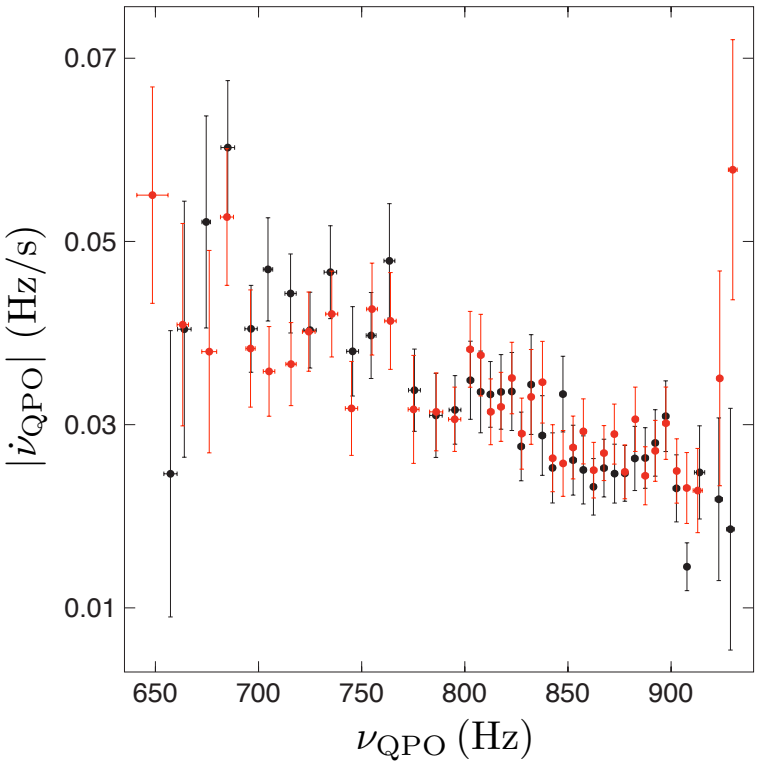

Figure 3.5: Comparison between absolute values of the positive (red points) and negative frequency derivative (black points) for the lower kHz QPOs in 4U 1636–53 detected on timescales shorter than 64 s.

s or less (the same as Figure 3.3), red points are for timescales between 64 and 160 s, and green points are for timescales of 160 s.

Interestingly, for timescales longer than 64 s the frequency derivative initially stays more or less constant as the QPO frequency increases, and at around 800 Hz it decreases following more or less the same trend seen on the shortest timescale. We investigated whether the difference between trends in Figure 3.4 is only caused by the different timescales. To do that we took the observations where we detected kHz QPOs in segments of data shorter than 64 s (black points in Figure 3.4), we created PDS increasing the length of the data segments up to 160 s and we searched again for kHz QPOs. We then recalculated the frequency derivative and we compared it with the green points in Figure 3.4. We found that the two distributions of points are consistent with each other, which shows that the difference between the three groups

of points in Figure 3.4 is likely due to the different timescales over which we measured the QPO frequency.

Finally, in Figure 3.5 we show, respectively, the absolute value of the negative (frequency decrease) and positive (frequency increase) frequency derivative for kHz QPOs detected on timescales of up to 64 s. We fitted both relations with a linear function. We found that, within the errors, there is no significant difference between the trend of the positive and negative QPO-frequency derivative with QPO frequency.

3.4 Discussion

We detected kHz QPOs in 528 out of 1280 RXTE observations of the LMXB 4U 1636–53 (all RXTE data available of this source up to May 2010). 26 of these 528 observations showed simultaneously the lower and the upper kHz QPO, whereas in the remaining 502 observations we detected a single kHz QPO that we identified using the frequency vs. hard colour diagram (see section 3.2.1). Using measurements of the lower kHz QPO on timescales between 32 and 160 s we measured, for the first time, the rate at which the QPO frequency changes as a function of the QPO frequency itself. For this we used both the spread of the QPO frequency over groups of 10 consecutive measurements, sampling timescales between 320 and 1600 s, and the time derivative of the QPO frequency over timescales of 32 to 160 s. Both the QPO-frequency spread and QPO-frequency derivative decrease by a factor of ~ 3 as the QPO centroid frequency increases from ~ 600 to ~ 900 Hz. Above ~ 910 Hz the QPO-frequency spread appears to increase again, albeit the evidence for this is marginal. We found that the relation between QPO frequency, $\nu_{\rm QPO}$, and QPO-frequency derivative, $\dot{\nu}_{\rm QPO}$, depends upon the timescale over which the QPO frequency is measured: When $\nu_{\rm QPO}$ is between 600 and ~ 770 Hz, $\dot{\nu}_{\rm QPO}$ decreases by a factor of ~ 2 as the timescale over which we measure the frequency derivative increases from 64 s or less up to 160 s. Finally, we found that the positive and negative values of $\dot{\nu}_{\rm QPO}$ are consistently distributed in the whole frequency range (see Figure 3.5), even at high frequencies where the accretion disc should approach the ISCO.

Barret, Olive, & Miller (2006) found that in 4U 1636–53, the coherence of the lower kHz QPO increases from $\sim$10 to $\sim$220 as the frequency of the QPO increases from $\sim$600 to $\sim$850 Hz, and then it decreases rather abruptly as the frequency continues increasing up to 950 Hz[2]. Barret, Olive, & Miller (2006)

[2]Data in Figure 3.2 to 3.5 show no unusual change in the trend of the QPO frequency spread or the time derivative at around 850 Hz, where Barret, Olive, & Miller (2006) see the sudden drop of the coherence of the lower kHz QPO in 4U 1636–53. Similarly, there

were able to model the behaviour of the coherence of the kHz QPO in terms of the lifetime of blobs of matter that move in quasi-Keplerian orbits at the inner edge of a geometrically-thin disc, the width of the disc annulus where these blobs produce the kHz QPOs, and the advection speed of the gas in the disc. Barret, Olive, & Miller (2006) conclude that the abrupt drop of the QPO coherence at about 850 Hz is due to the presence of the ISCO around the neutron star in this and other systems.

Comparing our results with Figure 8 in Barret et al. (2006), we find that the variation of the QPO frequency on timescales between 320 and 1600 seconds contributes significantly to the QPO width in the frequency range between ∼750 and ∼870 Hz, whereas it does not contribute to the increase of the QPO width at higher QPO frequencies. Previous results show that variations on shorter timescales can have a large impact on the width of QPO. E.g., Yu et al. (2001), showed that in the neutron star system Sco X-1 the frequency of the upper kHz QPO changes by 20 Hz on timescales of 1/6 Hz, which they relate to flux variation on these timescales.

The trend of the QPO spread in Figure 3.2 shows a marginal increase of the spread at around 915 Hz, which is close to the frequency at which Barret, Olive, & Miller (2005c) identify the signature of the ISCO on the lower kHz QPO in 4U 1636–53. If this apparent rise was real, it could be related to the idea that the high-frequency drop of the QPO coherence is a signature of the disc reaching the ISCO.

Most of the models so far proposed assume that the kHz QPOs are produced in an optically-thick geometrically-thin accretion disc, and that the frequency of either the lower or the upper kHz QPO represents the Keplerian frequency at a given radius in the disc (e.g., Miller et al., 1998b; Stella & Vietri, 1998; Osherovich & Titarchuk, 1999). For instance, in the sonic-point model (Miller, Lamb, & Psaltis, 1998b) the frequency of the upper kHz QPO corresponds to the radius at which the gas starts spiralling inward at a supersonic radial velocity, and changes of the QPO frequency reflect changes of mass accretion rate (ram pressure and radiation drag). In other models (e.g., Stella & Vietri, 1998; Osherovich & Titarchuk, 1999) the frequency of the QPOs also depends upon the radius of the disc where the QPOs are produced, although the mechanism by which this radius changes is not specified. In those models mass accretion rate is also likely responsible for changes of the radius in the disc where the QPO is produced.

are no unusual features at frequencies corresponding to small integer ratios of the kHz QPO frequencies in the spread and $\dot{\nu}_{\rm QPO}$ relations (Abramowicz et al., 2003; Belloni et al., 2005)

3.4.1 Comparison with standard disc theory

We can compare our measurements of $\dot{\nu}_{\rm QPO}$ of the lower kHz QPO with what is expected in the case of a thin disc (Shakura & Sunyaev, 1973) if $\nu_{\rm QPO}$ is the Keplerian frequency very close to the inner edge of the disc. We will further assume that the disc is truncated by an unspecified mechanism. According to the standard disc model (Shakura & Sunyaev, 1973), matter in the disc moves radially with a speed given by:

$$v_r = 0.98\,\alpha_s^{4/5}\,\dot{M}^{3/10}\,M_\star^{-1/4}\,R^{-1/4}\,f^{-14/5}\,{\rm km/s}, \tag{3.1}$$

with $f = [1-(R_\star/R)^{1/2}]^{1/4}$, where $\alpha = 0.1\alpha_s$ is the viscosity parameter, $\dot{M}$ is the mass accretion rate in units of 2.6×10^{17} g/s, $M_\star = M/1.8M_\odot$, R is the radius of the inner edge of the disc in km, and $R_\star$ is the neutron star radius in units of 14 km, respectively[3]. This is the speed at which matter very close to the inner edge of the accretion disc will move inwards one the disc has been truncated. Combining this expression with the Keplerian formula, we find that the derivative of the Keplerian frequency can be expressed as:

$$|\dot{\nu}| \approx 300\,\alpha_s^{4/5}\,\dot{M}^{3/10}\,M_\star^{-2/3}\,\nu_{kHz}^{11/6}\,F(\nu_{kHz})\,{\rm Hz/s}, \tag{3.2}$$

where ν_{kHz} is the Keplerian frequency in units of 1000 Hz, and $F(\nu_{kHz})$ is the factor $f^{-14/5}$ expressed as a function of ν_{kHz}, and normalised by the same factor calculated for a frequency of 1000 Hz. Assuming a 1.8 $M_\odot$ neutron star, the function $F(\nu_{kHz})$ increases from ~ 0.6 to ~ 0.9 as the frequency increases from 650 to 930 Hz. From this equation it is apparent that the time derivative of the Keplerian frequency very close to the inner edge of a thin disc increases as the Keplerian frequency increases, contrary to what we observe in the case of the lower kHz QPO in 4U 1636–53. Not only that, but for nominal values of the parameters, the time derivative of the Keplerian frequency in the frequency range between 650 and 950 Hz, is about 4 orders of magnitude larger than what we observe for the lower kHz QPO in 4U 1636–53. As it is apparent from eq. (3.2), this difference cannot be accounted for by changing the mass and the radius of the NS.

One way to reconcile the observations with the expectations from a thin disc is if the viscosity parameter α is $\sim 10^{-5}$ (cf. Belloni et al., 2007), although this would not revert the trend of $\dot{\nu}_{\rm QPO}$ with the QPO frequency. The $\dot{\nu}_{\rm QPO}$ vs. $\nu_{\rm QPO}$ trend from our analysis could be in principle reproduced by eq.(3.2) if the product $\alpha\times\dot{M}$ depended upon the accretion-disc radius. If we assume

[3]We assumed an average luminosity value for 4U 1636–53 of about 0.1 $L_{\rm Edd}$ (Ford et al., 2000) for a distance of 5.5 Kpc (van Paradijs & White, 1995), where $L_{\rm Edd}$ is the Eddington luminosity for a 1.8-solar masses neutron star.

for simplicity that α is constant with radius, the trend in eq.(3.2) would be reversed if the mass accreted from the secondary flowed out of the disc at a rate that increases as the radius decreases. In order to fit the observations, in 4U 1636–53 the amount of accreted mass that crosses through the inner edge of the disc must be $\sim 5\,\%$ of the total accreted mass from the secondary. In other words, about 95 % of the mass accreted from the secondary should not flow onto the neutron star via de accretion disc. Although this scenario cannot be completely ruled out, it is very unlikely because such a process should leave some trace in the spectral properties of the system, e.g., extra low-energy absorption, that has not been observed so far.

The majority of the models of the kHz QPOs propose that it is the *upper* kHz QPO that is Keplerian (e.g., Miller, Lamb, & Psaltis 1998b, Stella & Vietri 1998). Since the upper kHz QPO in 4U 1636–53 is much broader and weaker than the lower one (e.g.; Barret, Olive, & Miller 2005b), the upper kHz QPO is in general less significant than the lower one when both are measured over the same timescale. We therefore were unable to recover the frequency profile of the upper kHz QPO on the same timescales as for the lower kHz QPO to compare the time derivative of the upper kHz QPO with that of the Keplerian frequency in a thin disc. However, Belloni et al. (2005) showed that in 4U 1636–53 the frequency of the lower and upper kHz QPOs, ν_l and ν_u, respectively, follow a linear relation $\nu_u = 0.673 \times \nu_l + 539$ Hz. If this relation still holds on short timescales, we can combine it with our measurements of the lower kHz QPO and estimate the time derivative of the upper kHz QPO frequency. We find that, similar to the case of the lower kHz QPO described above, the time derivative of the frequency of the upper kHz QPO decreases as the frequency of the upper kHz QPO increases, which is again at variance with what is expected from the thin disc model.

From the above we conclude that changes of the QPO frequency, at least for the case of 4U 1636–53, are not compatible with the dynamics of the inner edge of a standard α-disc.

3.4.2 Standard disc theory plus radiation drag

The positive and negative derivatives of the QPO frequency appear to follow the same trend as a function of the QPO frequency (see section 3.3 and Figure 3.5). This suggests that there is a coupling between the mechanisms that drive the inner edge of the disc inwards and outwards. In this subsection we explore the case in which the accretion disc is truncated at the so-called sonic-point radius, the position in the disc where the radial velocity of the inflowing gas changes from subsonic to supersonic (Miller, Lamb, & Psaltis, 1998b). In this scenario, mass accretion rate through the accretion disc pushes

the inner edge of the disc inwards in a similar way to the one we described in the previous subsection; but in this case, the radiation produced by the mass that eventually accretes onto the neutron-star surface removes angular momentum from the disc. The position of the inner radius of the accretion disc is therefore set by the interplay between radiation drag and viscosity. Using general relativistic calculations of the gas dynamics and radiation transport in the inner edge of the accretion disc, Miller, Lamb, & Psaltis (1998b) found that the sonic radius can be written approximately as:

$$R_{sr} \approx R + 5 \left(\frac{\dot{M}_i}{0.01 \dot{M}_E} \right)^{-1} \left(\frac{R}{10\mathrm{km}} \right) \left(\frac{h/r}{0.1} \right) \left(\frac{v^r}{10^{-5} c} \right), \tag{3.3}$$

where R is the NS radius in kilometres, $\dot{M}_i$ is the mass accretion rate through the disc, $\dot{M}_E$ is the Eddington mass accretion rate, h is the thickness of the disc at a radial distance r in the disc, and v^r is the radial velocity of the gas in the accretion disc. We can therefore write:

$$|\dot{\nu}_{sr}| = \frac{3}{4\pi} (GM)^{1/2} \, R_{sr}^{-5/2} \, |\dot{R}_{sr}|, \tag{3.4}$$

with

$$|\dot{R}_{sr}| \approx 0.05 \, \dot{M}_E \left(\frac{\dot{M}_i}{0.01 \dot{M}_E} \right)^{-2} \ddot{M}_i \left(\frac{R}{10\mathrm{km}} \right) \left(\frac{h/r}{0.1} \right) \left(\frac{v^r}{10^{-5}\mathrm{c}} \right), \tag{3.5}$$

where $\ddot{M}_i$ is the time derivative of the mass accretion rate through the disc. We can now in principle use equations (3.3) to (3.5) to calculate $\dot{\nu}_{\rm sr}$ vs. $\nu_{\rm sr}$, given the NS mass and radius. For that we also need to specify h/r, v^r and $\ddot{M}_i$. In systems in which accretion is the main source of radiation, the bolometric luminosity is proportional to the total mass accretion rate. To the extent that in LMXBs the X-ray intensity, $I_{\rm X}$, is a good measure of the bolometric luminosity (e.g., Ford et al., 2000), $\ddot{M}_i \propto \dot{I}_{\rm X}$. Putting all this together, and assuming that h/r and v^r are constant, we find that $\dot{\nu}_{\rm sr} \propto \nu_{\rm sr}^{5/3} \, \dot{I}_X / I_X^2$. Using the observed variations of $I_{\rm X}$ with time we find that $\dot{\nu}_{\rm sr}$ decreases by a factor ~ 2 as $\nu_{\rm sr}$ increases from ~ 650 to ~ 900 Hz, which is comparable to what we found in 4U 1636–53 (see Figure 3.3).

However, it is well known that, while on timescales of hours kHz QPO frequency correlates with $I_{\rm X}$, on timescales of days or longer the kHz QPO frequency can be the same even if $I_{\rm X}$ is a factor of ~ 2 different. This is the so-called parallel-track phenomenon (Méndez et al., 1999; van der Klis, 2001). If the frequency of (one of) the kHz QPOs reflects the Keplerian frequency at the inner edge of the disc, and the position of the inner edge of the disc

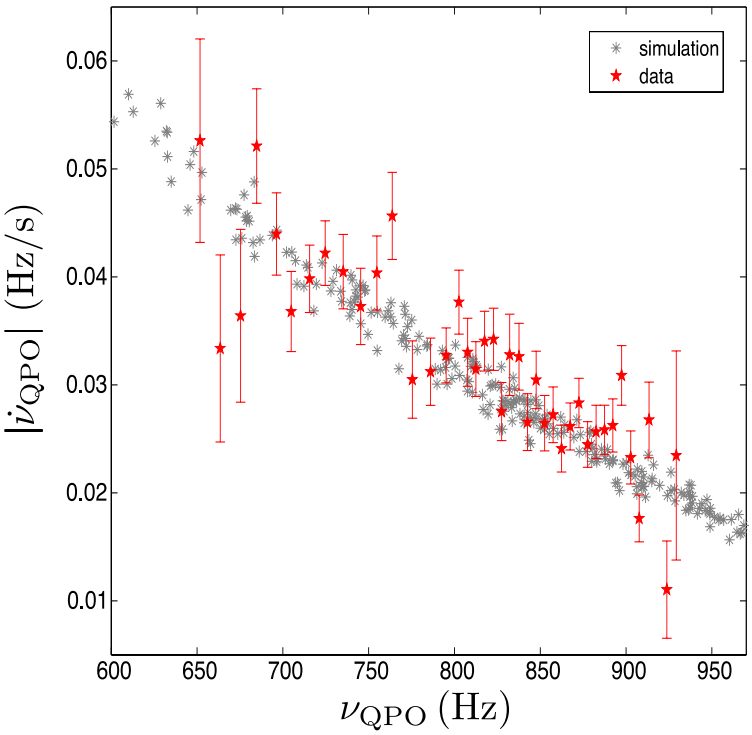

Figure 3.6: Comparison between the absolute value of the frequency derivative of the lower kHz QPO frequency in 4U 1636–53 (red points) and simulated values of the frequency derivative of the lower kHz QPO using the *sonic-point model* from Miller, Lamb, & Psaltis (1998b) (grey stars). See section 3.4.2 for more details about the simulation.

depends on $\dot{M}_i$ as in eq. (3.3), the parallel-track phenomenon means that there cannot be a one-to-one relation between $\dot{M}_i$ and $I_{\rm X}$, and that the procedure that we described in the previous paragraph is incorrect.

To overcome this problem, we proceeded as follows: Since the frequencies of the kHz QPOs appear to follow a random walk (Belloni et al., 2005; Barret & Vaughan, 2012), we generated values of $\dot{M}_i$ following a random walk[4] we calculated $\ddot{M}_i$, and we computed $\dot{\nu}_{\rm sr}$ vs. $\nu_{\rm sr}$ using eq. (3.3) to (3.5). Following Miller, Lamb, & Psaltis (1998b), we took $h/r = 0.1$ and $v^r = 10^{-5}c$, we assumed a NS with a radius of 13 km and a mass of 1.9 $M_\odot$, and generated

[4]We restricted $\dot{M}_i$ to be between 1% and 3% $\dot{M}_E$ generating uniformly random distributed steps between -10^{-4} and 10^{-4} $\dot{M}_E$.

values of $\dot{M}_i$ between 0.01 and 0.03 $\dot{M}_E$. We further assumed that the Keplerian frequency at the sonic-point radius is the upper kHz QPO (Miller, Lamb, & Psaltis 1998b; but see below), and converted the sonic-point Keplerian frequency to that of the lower kHz QPO using the relation $\nu_u = 0.673 \times \nu_l + 539$ Hz from Belloni et al. (2005), where ν_l and ν_u are, respectively, the frequencies of the lower and the upper kHz QPO. In Figure 3.6 we plot the observed relation $\dot{\nu}_{\rm QPO}$ vs. $\nu_{\rm QPO}$ (red points; these are the same data as in Figure 3.3) together with the relation between $\dot{\nu}_{\rm sr}$ and $\nu_{\rm sr}$ from this simulation (grey stars). From this Figure it is apparent that the simulation reproduces the observed data well. We note that although the range of $\dot{M}_i$ in our simulation is a factor of ~ 3 less than the range of luminosities spanned by 4U 1636–53 (e.g., Ford et al., 2000), this may be accounted for if we adjust the values of h/r and v^r accordingly. Finally, we note that we can reproduce the data equally well if we assume that the frequency at the sonic-point radius is the lower kHz QPO if, in this case, the neutron star has a radius of 14 km and a mass of 1.7 $M_\odot$.

In summary, assuming that the frequency of one of the kHz QPOs is equal to the Keplerian frequency at the inner edge of the accretion disc, the comparison between the observations and our simulations appears to lend support to the idea that the inner edge of the accretion disc is set by the interplay between viscosity and radiation drag. Our results, however, do not shed light about the mechanism that produces the kHz QPOs, or whether it is the lower or the upper kHz QPO the one that reflects the Keplerian frequency at the inner edge of the accretion disc. It remains to be seen whether other mechanisms (e.g., magnetic drag) can also reproduce the observations.

Acknowledgment. This research has made use of data obtained from the High Energy Astrophysics Science Archive Research Center (HEASARC), provided by NASA's Goddard Space Flight Center. This research made use of the SIM-BAD database, operated at CDS, Strasbourg, France and NASA's Astrophysics Data System. We thank the International Space Science Institute (ISSI) for their support. We thank Cole Miller, Didier Barret, Fred Lamb, Jeroen Homan, Phil Uttley and Luciano Burderi for interesting discussions on the topic. We are grateful to an anonymous referee for the comments that helped us improve the manuscript. TMB acknowledges support from grant INAF-ASI 1/009/10/0.

4 High-Frequency Quasi-Periodic Oscillations in black-hole binaries

— **Tomaso Belloni, Andrea Sanna, Mariano Méndez** —

MNRAS, 2012, 426, 1701

Abstract

We present the results of the analysis of a large database of X-ray observations of 22 galactic black-hole transients with the Rossi X-Ray timing explorer throughout its operative life for a total exposure time of ∼12 Ms. We excluded persistent systems and the peculiar source GRS 1915+105, as well as the most recently discovered sources. The semi-automatic homogeneous analysis was aimed at the detection of high-frequency (100-1000 Hz) quasi-periodic oscillations (QPO), of which several cases were previously reported in the literature. After taking into account the number of independent trials, we obtained 11 detections from two sources only: XTE J1550–564 and GRO J1655–40. For the former, the detected frequencies are clustered around 180 Hz and 280 Hz, as previously found. For the latter, the previously-reported dichotomy 300-450 Hz is found to be less sharp. We discuss our results in comparison with kHz QPO in neutron-star X-ray binaries and the prospects for future timing X-ray missions.

4.1 Introduction

The Rossi X-Ray Timing Explorer (RXTE) mission has provided thousands of high-quality observations of black-hole transients (BHTs), which have profoundly changed our knowledge of the properties of accretion onto stellar-mass black holes (see e.g., Belloni, 2010; Fender, 2010, Belloni et al. 2012). An important aspect has been the detection of Quasi-Periodic Oscillations (QPO) at frequencies higher than ∼40 Hz, which opened a new window onto fast phenomena in the frequency range expected from signals associated to Keplerian motion in the innermost regions of an accretion disk around a black hole. A small number of detections is available in the literature from a small number of sources: GRS 1915+105 (Morgan et al., 1997; Strohmayer, 2001a; Belloni et al., 2001; Remillard et al., 2002a; Belloni et al., 2006), GRO J1655–40 (Remillard et al., 1999; Strohmayer, 2001a), XTE J1550–564 (Homan et al., 2001; Miller et al., 2001; Remillard et al., 2002b), H1743–322 (Homan et al., 2005; Remillard et al., 2006b), XTE J1650–500 (Homan et al., 2003), 4U 1630–47 (Klein-Wolt et al., 2004), XTE J1859+226 (Cui et al., 2000) and IGR J17091–3624 (Altamirano & Belloni, 2012). The signals are very weak and some detections appear to have marginal statistical significance. Although these High-Frequency QPOs (hereafter HFQPOs) are very important as they constitute a promising way to detecting effects of General Relativity in the strong field regime, no systematic work on the existing bulk of RXTE data is available. In particular, it is important to compare quantitatively the existing results with those from kilohertz QPOs from neutron star X-ray binaries, where signals are stronger and the known phenomenology much better covered (see e.g. van der Klis, 2006, for a review). The similarities between the timing features of these two classes of sources are strong (see Wijnands & van der Klis, 1999; Psaltis et al., 1999; Belloni et al., 2002; van der Klis, 2006), but it is not clear how HFQPOs fit in this comparison. In this paper, we present a systematic analysis of a large sample of RXTE observations of BHTs, concentrating on the detection of HFQPOs. All major sources are present, with the exception of GRS 1915+105, which will be the subject of a separate paper due to the large number of available observations and its peculiarities) and IGR J17091–3624, which was observed by RXTE after the analysis part of this work was completed. An a posteriori bulk analysis of the data suffers from problems related to number of trials, which means that the sensitivity to detections will be reduced. In addition, our procedure was aimed only at detecting one peak in each Power Density Spectrum (PDS), which means that double detections do not appear. Finally, different observations were analysed separately without any merging, although merging was the way some of these

Table 4.1: Statistics of available data and obtained detections. Columns are: source name, total number of observations, number of observations analysed in each band, total exposure considered in each band, number of observations with single try probability $>3\sigma$ in each band, number of detections after manual analysis in each band and final number of detections.

Source name	N. obs.	Valid T.	Valid H.	Exp. T (ks)	Exp. H (ks)	$>3\sigma$ T	$>3\sigma$ H	Good T	Good H	Final
GX 339–4	1353	893	517	2190	1657	31	34	4	11	4
4U 1630–47	1002	846	701	1934	1672	31	27	11	7	4
GRO J1655–40	596	516	491	2295	2214	18	24	7	8	11
H 1743-322	504	386	300	1153	941	19	20	6	8	4
XTE J1550–564	409	319	280	860	790	46	31	15	14	16
Swift J1753.5–0127	278	240	172	671	527	14	8	3	3	0
XTE J1752–223	208	138	79	343	250	6	6	0	4	2
XTE J1650–500	182	101	69	219	155	17	5	4	2	0
Swift J1539.2–6227	156	61	42	153	122	1	3	1	1	0
XTE J1817–330	155	112	79	372	256	3	2	1	1	0
XTE J1859+226	131	115	102	314	281	6	4	2	2	1
4U 1543–47	104	53	38	161	125	6	3	0	1	0
XTE J1720-318	100	75	19	233	101	1	1	0	1	0
4U 1957+115	100	97	46	529	334	1	0	0	0	0
XTE J1118+480	94	62	50	174	154	0	3	0	1	0
MAXI J1659–152	66	63	54	148	135	1	1	0	1	0
SLX J1746–331	65	47	23	125	72	2	2	0	0	0
XTE J1652–453	57	30	1	67	2	1	0	0	0	0
XTE J1748–288	24	23	21	103	99	0	1	0	0	0
SAX J1711.6–3808	17	17	12	43	30	0	0	0	0	0
GS 1354–644	8	7	7	52	52	0	1	0	0	0
GRS 1737–31	5	4	3	40	28	0	0	0	0	0
Total	7108	4205	3106	12177	9996	204	176	54	65	42

oscillations were found. However, such a (semi-automatic) procedure is useful to assess what is available from RXTE data and to plan future observations with upcoming facilities like ASTROSAT and LOFT. The comparison with previous works is in many cases difficult as the starting conditions for the analysis are markedly different. Motivated selection of observations and/or merging, as well as the relaxation of the constraints imposed in our search (total number of available observations, frequency range considered, energy range for the accumulation, limits on the quality factor of the signal) can lead to more sensitive results.

4.2 Data & analysis

We selected all RXTE observations of known transient black-hole binaries available in the archive from the start of the mission until MJD 55601 (2011 February 9), concentrating on the data from the Proportional Counter Array (PCA) instrument. We analysed 22 sources, for a total of 7108 observations (see Tab. 4.1). The bright source GRS 1915+105 was not included for two reasons: its peculiarity and the fact that effectively during the RXTE lifetime it behaved as a persistent source. The analysis of data from GRS 1915+105

will be reported in a forthcoming paper. For the project presented here, it is important to establish a detailed analysis procedure in advance, in order to control and minimise the probability of spurious detections. The following multi-step procedure was applied.

(I) Two energy bands were considered for analysis: absolute channels 0-79 and 14-79 (corresponding to energies 1.51-21.30 keV and 4.07-21.30 keV at the beginning of the mission and to energies 2.06-33.43 keV and 6.12-33.43 keV a the end of the mission, due to gain changes in the detectors). We will refer to these as the total and hard band respectively. For some observations, these exact bands were not available due to the data modes, in which case we chose the closest approximation to those boundaries. In a few cases, the data modes were such that we used the full channel range and/or the total and hard band resulted to be identical. The choice of the hard band was made in order not to deplete too much the number of counts and allow the examination of more observations (see next bullet).

(II) When analysing a large number of observations, the issue of number of trials must be considered carefully. Of all observations in our sample, a sizeable number were of a source at the very start or at the end of an outburst, where count rate is low and the sensitivity to detect quasi-periodic features is very low. We decided not to analyse observations where the data are not expected to yield a positive detection for HFQPO. Rather than selecting a simple threshold in count rate to exclude the observations, we used the expression to estimate the significance (in number of sigmas, n_σ) of a broad feature in frequency domain

$$n_\sigma = \frac{1}{2} r_s^2 \frac{S^2}{(S+B)} \sqrt{\frac{T_{exp}}{\Delta\nu}}$$

(see van der Klis, 2004b) where r_s is the fractional rms variability of the feature, S is the source net count rate, B is the corresponding background count rate, T_{exp} is the exposure time and $\Delta\nu$ is the FWHM of the feature. We assumed a QPO with 6% fractional rms and 10 Hz FWHM and used the observed count rates and exposure time to estimate the expected sensitivity. We then excluded all hard or total observations which yielded $n_\sigma < 3$.

With this procedure we retained 4205 total observations and 3106 hard observations, for a cumulative exposure time of 12.2 Ms and 10.0 Ms re-

spectively (see Tab. 4.1). We consider a separate observation (or dataset) the data corresponding to a RXTE observation ID.

(III) The large number of observations made it necessary to perform an automatic search in order to select candidates for HFQPOs. For each observation, the adopted procedure, applied both to the total and hard energy band, was the following:

- We produced a PDS by dividing the dataset in intervals of 16s duration and averaging the corresponding PDS. The time resolution for all spectra was 4096 points per second, corresponding to a Nyquist frequency of $\sim$2 kHz. The PDS were normalised according to Leahy et al. (1983). The powers were rebinned logarithmically in such a way that each frequency bin was larger than the previous one by $\sim$2%.Uncertainties in the power values were estimated following van der Klis (2004b).
- Since the PDS of BHTs are rather complex and we were interested only in the high-frequency region, we considered only the frequency range 100-1000 Hz. This means that our implicit definition of HFQPO is limited to centroid frequencies larger than 100 Hz.
- We fitted the PDS with an automatic procedure with a model consisting of a power law (to account for the Poissonian noise component) and a Lorentzian. The slope of the power law was not fixed to 0 (constant component) in order to fit any possible remaining tail of low-frequency features. We did the fit by first fixing the Lorentzian centroid frequency to all values between 100 and 1000 Hz in steps by 1 Hz. The FWHM of the Lorentzian was bound between 0.5 Hz and 1000 Hz. A fit with a free centroid was then made around the frequency corresponding to the minimum chi square. This resulted in a single best fit for each observation. Notice that this procedure is aimed at detecting a single HFQPO in each PDS and would not be able to detect multiple peaks.
- From each fit, we estimated the significance of the detection by dividing the normalisation (integral) of the Lorentzian by its 1σ error on the negative side. Only features with this figure of merit larger than 3 were considered. The surviving number of observations can be seen in the 3σ columns of Tab. 4.1.
- Examining the best fit parameters, we were able to eliminate obvious meaningless fits. Those included fits where the FWHM had

reached one of the two imposed limits (see above), making the feature impossibly narrow or broad, and those where the centroid frequency was close to the search limits. In addition, we discarded all features with a quality factor $Q = \nu_0/FWHM$ significantly less than 2, as we are interested only in peaked signals. We checked all these cases visually in order not to miss peculiar features. None were found. In this way, the numbers of HFQPO candidates dropped to those in the "good" columns in Tab. 4.1.

- For all remaining PDS, we made a manual fit with the same model described above and we re-established the significance of the fit in the same way. In case we found a peak at a consistent frequency, both in the hard and total PDS, we retained the one with the highest significance. The final numbers of detections from this procedure are shown in the last column of Tab. 4.1. The total number was 42. For all fits, the reduced chi square was close to unity.

(IV) The resulting HFQPOs have a significance (estimated in the way described above) larger than 3σ for a single trial. We searched them in a number of PDS for each source and we considered a broad range of frequencies. Both these procedures translate in a number of trials. For each source, we considered how many PDS were searched (for the total plus hard band) and how many independent frequencies were considered: for each detection we divided the 900 Hz interval used for the search by the FWHM of the detected QPO. Keeping these two effects in mind of course lowers the significance.

We did this under the assumption that any frequency within the considered range would be accepted. If one wants to limit to certain frequencies, for instance considering only peaks around 180 Hz and 280 Hz for XTE J1550–564 as previously detected (Homan et al., 2001; Miller et al., 2001; Remillard et al., 2002b), the number of trials will change and so will the significance of the detections. For this reason, in Tab. 4.2 we show all 42 detections. In the following, we will restrict the discussion only to those with a high significance. We marked in boldface in the table the HFQPOs with a final chance probability less than 10^{-2}. Notice that a number of detections have a (rounded) final chance probability of 1, making them unlikely to be real. One has a rounded probability of 0, as it was so low that the spreadsheet we used could not approximate it.

(V) Notice that our procedure can only detect one peak per PDS. In principle, two different features can be detected in the total and hard PDS,

but this did not happen. No clear additional peaks were seen visually in the PDS containing a detection.

In addition, we produced a Hardness-Intensity Diagram (HID) for each source, one point per observation, by accumulating net energy spectra from PCU2 (the best calibrated of the five units of the PCA) using standard procedures [1]. The count rates were corrected for gain changes by dividing the spectra by a Crab spectrum (power law with photon index 2 and normalisation 10 ph/cm^{-2}s^{-1}keV^{-1} at 1 keV) simulated with the detector response at the day of the observation. Intensity is accumulated over PCA channels 8-49, corresponding to 3.2-19 keV at the end of the mission. Hardness is defined as H/S where S and H are the corrected rates in the channel bands 8-14 (3.2-6 keV) and 15-24 (6-10 keV) respectively.

4.3 Results

In this section we examine the results for each source for which HFQPOs have been detected. We study in detail only detections at more than 3σ significance after keeping number of trials into account.

4.3.1 XTE J1550–564

We selected sixteen features with a single-trial chance probability lower than that corresponding to 3σ: 1.35×10^{-3} (see Tab. 4.2). When we took into account the number of trials and considered detections of significance higher than 99%, we were left with 7 cases. Notice that some detections correspond to a very low count rate, but we nevertheless included them in the sample for completeness. Most of them are at a frequency close to either 180 Hz or 280 Hz, with the exception of the ones with the highest chance probability. In Figure 4.2, we show the HID of all observations of XTE J1550–564 with the detection of HFQPOs (depending on the chance probability). It is clear that all detections correspond to intermediate hardness and it is interesting to note that the observations lie on a diagonal line: the brighter the observed rate, the harder the energy spectrum, with the two detections at a lower frequency corresponding to softer spectra. The same applies to the grey points, with one exception. An examination of the full PDS for these observations indicates that the first one in Tab. 4.2 corresponds to the brightest observation, where there is a low-frequency QPO (LFQPO) which can be classified as type-A (although Remillard et al., 2002b, did not classified it at the time). The second

[1] http://heasarc.nasa.gov/docs/xte/data_analysis.html

Table 4.2: List of detected HFQPOs. Columns are: observation date (MJD), exposure time, band in which the QPO was detected (Total/Hard), centroid frequency, FWHM and fractional rms of the QPO, single trial and final chance probabilities, source observed count rate (in PCU2) and X-ray hardness.

MJD	Exp. (s)	B	ν_0 (Hz)	FWHM (Hz)	%rms	P_0	P_F	Rate	HR
XTE J1550–564									
51076.000	2960	T	**180.76** $^{+3.92}_{-4.37}$	95.12 $^{+16.12}_{-22.00}$	1.15 $^{+0.14}_{-0.12}$	2.87E-07	1.62E-03	15700	0.68
51101.607	1584	T	140.70 $^{+1.71}_{-1.92}$	16.51 $^{+19.85}_{-4.84}$	1.12 $^{+0.59}_{-0.17}$	6.64E-04	1.00E+00	3135	0.57
51108.076	9872	T	**182.27** $^{+3.25}_{-3.20}$	77.88 $^{+11.65}_{-9.77}$	1.74 $^{+0.20}_{-0.16}$	1.90E-08	1.31E-04	3636	0.53
51115.281	2048	H	272.43 $^{+3.42}_{-4.09}$	30.59 $^{+16.30}_{-8.95}$	4.02 $^{+0.78}_{-0.47}$	7.80E-06	1.28E-01	1785	0.41
51241.802	3104	H	**284.07** $^{+1.35}_{-1.36}$	26.86 $^{+3.88}_{-3.12}$	3.66 $^{+0.21}_{-0.17}$	8.77E-29	0.00E+00	4258	0.42
51242.507	1504	H	**280.00** $^{+2.87}_{-2.49}$	30.00 $^{+9.80}_{-6.85}$	3.78 $^{+0.46}_{-0.32}$	2.05E-09	3.69E-05	4107	0.43
51245.354	2752	T	180.75 $^{+2.02}_{-2.54}$	16.76 $^{+8.71}_{-6.21}$	1.08 $^{+0.25}_{-0.13}$	8.54E-06	2.40E-01	4718	0.54
51247.979	2816	T	185.20 $^{+6.73}_{-4.93}$	46.04 $^{+15.69}_{-12.13}$	1.32 $^{+0.30}_{-0.17}$	3.30E-05	3.21E-01	4509	0.54
51255.158	4080	H	**280.84** $^{+2.00}_{-1.92}$	24.37 $^{+8.53}_{-6.28}$	4.35 $^{+0.50}_{-0.41}$	7.20E-08	1.59E-03	2329	0.38
51258.497	1104	H	276.02 $^{+6.64}_{-6.20}$	36.77 $^{+23.00}_{-12.36}$	5.22 $^{+0.01}_{-0.76}$	2.91E-04	9.86E-01	1816	0.35
51259.253	880	H	274.87 $^{+4.30}_{-3.61}$	26.00 $^{+14.57}_{-8.68}$	5.09 $^{+1.00}_{-0.67}$	7.53E-05	7.90E-01	1710	0.39
51291.184	1536	T	134.75 $^{+1.76}_{-1.45}$	7.81 $^{+5.16}_{-3.25}$	6.84 $^{+1.28}_{-1.09}$	8.45E-04	1.00E+00	88	0.42
51664.409	2240	H	**274.40** $^{+3.43}_{-3.47}$	41.96 $^{+19.88}_{-10.66}$	6.66 $^{+1.23}_{-0.64}$	1.11E-07	1.42E-03	1347	0.29
51664.637	2864	H	**274.97** $^{+2.90}_{-3.21}$	33.51 $^{+13.97}_{-8.16}$	5.42 $^{+0.87}_{-0.51}$	4.65E-08	7.47E-04	1419	0.31
51665.406	2144	H	264.66 $^{+7.09}_{-3.19}$	42.87 $^{+22.01}_{-15.43}$	6.50 $^{+1.35}_{-1.02}$	6.87E-04	1.00E+00	1105	0.28
51668.829	2976	H	263.29 $^{+9.41}_{-9.96}$	53.90 $^{+30.55}_{-17.58}$	5.50 $^{+1.56}_{-0.75}$	1.36E-04	7.44E-01	856	0.26
GRO J1655–40									
50296.311	9056	T	**273.72** $^{+3.97}_{-3.96}$	70.33 $^{+19.40}_{-10.92}$	1.15 $^{+0.15}_{-0.08}$	1.15E-13	1.483E-9	7443	0.67
50301.665	6464	T	307.16 $^{+8.17}_{-6.77}$	68.46 $^{+0.00}_{-38.07}$	0.88 $^{+0.21}_{-0.11}$	3.91E-05	4.04E-01	6414	0.61
50311.391	1856	T	285.56 $^{+8.91}_{-11.19}$	63.78 $^{+42.48}_{-17.38}$	1.14 $^{+0.36}_{-0.16}$	1.93E-04	9.35E-01	5450	0.54
50317.441	6176	H	443.16 $^{+4.12}_{-3.79}$	41.44 $^{+20.27}_{-13.66}$	5.39 $^{+0.81}_{-0.64}$	1.28E-05	2.44E-01	5210	0.51
50324.380	4896	T	**289.67** $^{+6.26}_{-6.03}$	98.78 $^{+40.67}_{-17.67}$	1.41 $^{+0.30}_{-0.11}$	1.59E-10	1.46E-06	7267	0.65
50330.254	6144	H	453.72 $^{+6.29}_{-5.32}$	37.69 $^{+16.46}_{-12.16}$	5.69 $^{+0.89}_{-0.71}$	2.91E-05	5.03E-01	4964	0.49
50335.913	8160	H	**446.35** $^{+4.10}_{-4.15}$	38.74 $^{+9.80}_{-8.00}$	6.03 $^{+0.59}_{-0.54}$	9.01E-09	2.11E-04	4983	0.50
50383.565	6192	H	442.34 $^{+4.71}_{-4.28}$	31.50 $^{+15.62}_{-10.61}$	4.55 $^{+0.70}_{-0.62}$	1.31E-04	9.77E-01	6092	0.54
50394.884	5792	T	**313.45** $^{+9.38}_{-9.81}$	98.11 $^{+38.42}_{-19.10}$	1.17 $^{+0.25}_{-0.11}$	3.72E-08	3.44E-04	5497	0.59
53498.415	13968	T	125.81 $^{+1.10}_{-1.20}$	7.49 $^{+3.86}_{-2.91}$	0.65 $^{+0.11}_{-0.09}$	2.16E-04	1.00E+00	3190	0.29
53508.507	7504	T	266.63 $^{+7.96}_{-7.80}$	61.76 $^{+30.61}_{-13.60}$	0.76 $^{+0.19}_{-0.09}$	2.67E-05	3.24E-01	10164	0.57
XTE J1859+226									
51485.875	6064	H	269.44 $^{+5.03}_{-6.28}$	38.55 $^{+33.43}_{-13.53}$	4.91 $^{+1.57}_{-0.71}$	2.70E-04	7.46E-01	824	0.21
H 1743-322									
52803.517	6416	H	240.39 $^{+3.99}_{-4.26}$	33.11 $^{+14.35}_{-10.41}$	3.01 $^{+0.59}_{-0.36}$	1.66E-05	2.66E-01	1366	0.34
52805.425	5232	H	232.38 $^{+1.41}_{-1.38}$	7.65 $^{+6.43}_{-3.20}$	2.09 $^{+0.49}_{-0.31}$	3.13E-04	1.00E+00	1314	0.35
53207.602	2608	H	178.57 $^{+1.23}_{-0.93}$	6.01 $^{+4.09}_{-3.80}$	6.84 $^{+1.26}_{-1.10}$	9.04E-04	1.00E+00	316	0.14
55422.024	1440	T	208.36 $^{+1.50}_{-1.78}$	8.04 $^{+4.68}_{-3.38}$	5.39 $^{+0.51}_{-0.75}$	1.72E-04	1.00E+00	238	0.81
GX 339–4									
52387.556	11200	H	127.70 $^{+4.16}_{-5.57}$	44.21 $^{+26.18}_{-10.53}$	3.19 $^{+1.05}_{-0.35}$	2.95E-06	8.12E-02	977	0.82
52490.229	816	H	278.67 $^{+3.47}_{-3.09}$	15.48 $^{+10.47}_{-6.55}$	6.32 $^{+1.45}_{-1.01}$	8.74E-04	1.00E+00	1186	0.16
52690.841	3408	T	105.35 $^{+1.77}_{-1.50}$	8.87 $^{+4.46}_{-3.78}$	6.32 $^{+1.12}_{-1.01}$	8.45E-04	1.00E+00	74	0.09
54291.443	1264	T	208.44 $^{+2.81}_{-2.68}$	14.68 $^{+8.67}_{-5.19}$	12.53 $^{+2.43}_{-1.93}$	5.98E-04	1.00E+00	41	0.87
XTE J1752–223									
55135.406	2896	H	442.91 $^{+3.42}_{-3.90}$	20.23 $^{+16.19}_{-8.27}$	7.06 $^{+1.51}_{-1.06}$	4.50E-04	9.87E-01	391	0.94
55140.573	3424	H	114.87 $^{+0.76}_{-0.58}$	4.50 $^{+3.42}_{-2.39}$	2.22 $^{+0.49}_{-0.35}$	8.16E-04	1.00E+00	393	0.93
4U 1630–47									
50893.719	9936	T	287.73 $^{+3.18}_{-3.95}$	20.17 $^{+17.73}_{-8.60}$	2.85 $^{+0.78}_{-0.46}$	9.04E-04	1.00E+00	250	0.69
50972.126	880	T	267.55 $^{+5.32}_{-6.59}$	32.97 $^{+14.55}_{-12.50}$	15.30 $^{+2.64}_{-2.46}$	9.35E-04	1.00E+00	41	1.60
52929.482	1712	H	446.72 $^{+2.39}_{-2.95}$	14.22 $^{+8.77}_{-7.29}$	3.65 $^{+0.59}_{-0.57}$	6.41E-04	1.00E+00	1438	0.60
53215.429	1488	T	150.46 $^{+0.88}_{-1.14}$	4.91 $^{+3.36}_{-3.09}$	1.96 $^{+0.43}_{-0.30}$	4.83E-04	1.00E+00	799	0.48

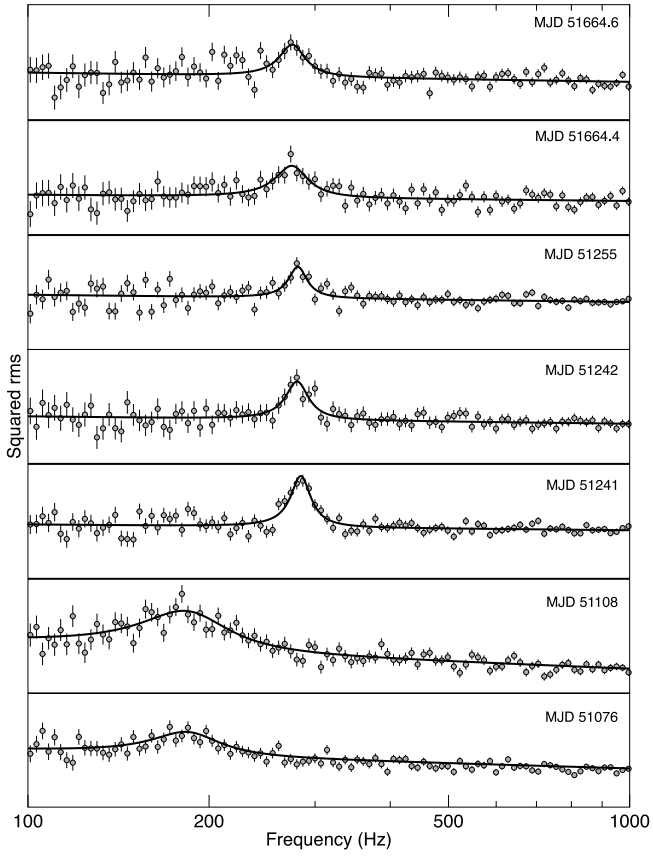

Figure 4.1: PDS of the seven good detections of HFQPO for XTE J1550–564 with the corresponding best fit models.

observation shows a very clear type-B QPO, while all the others have a type-A QPO. Overall, all observations can be considered part of the soft-intermediate state (SIMS, see Belloni, 2010). The centroid frequencies are clustered around two values: ∼180 Hz and ∼280 Hz, while their Q value is around 2 for the low-frequency peak and 6-10 for the high-frequency one. The fractional rms of the low-frequency peak is low, around 1% (total band), as opposed to that of the high-frequency peak which ranges from 3.6% to 6.7% (hard band). Notice that the two last observations belong to a different outburst than the first five, but the QPO centroid frequency is remarkably similar to the others.

There are 20 detections reported in Remillard et al. (2002b) from the 1998 outburst of XTE J1550–564. Ten of them appear also in our sample, whereas ten were not detected by our procedure. We checked them all visually and

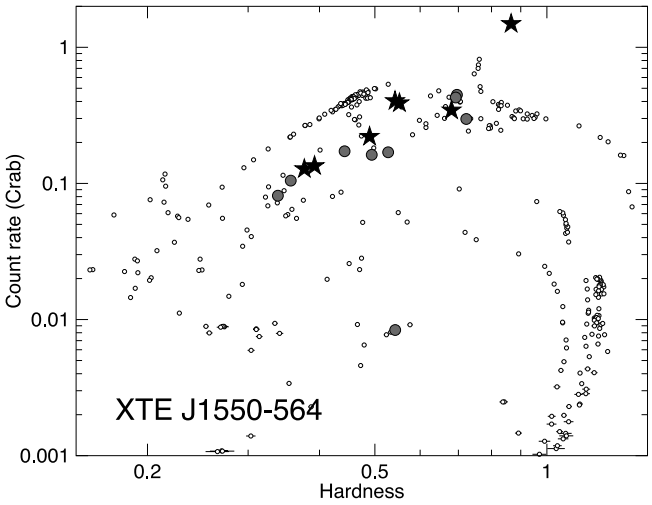

Figure 4.2: Hardness-Intensity Diagram for XTE J1550–564. Each point corresponds to a PCA observation. Grey circles correspond to HFQPO detections with final chance probability larger than 1%, black stars to those with smaller chance probability.

found that many of them resulted in very broad weak excesses superimposed to the tail of a noise component, which led to non significant detections in our analysis. Remillard et al. (2002b) do not report any parameter other than the centroid frequency and Q values (from 1 to 15 from their Fig. 7), and it is therefore difficult to make a deeper comparison. Remillard et al. (2002b) claim detections at 4σ level, but they give no indication as to how they estimated the significance.

Miller et al. (2001) report six detections of HFQPO from the 2000 outburst of XTE J1550–564. After taking into account a one-day shift in their Tab. 1, the first four of them correspond to our last four detections. The last two, at slightly lower frequency, are not in our final sample. An inspection of the PDS from those observations show that there is a feature, which our program detected at a significance slightly lower than 3σ.

4.3.2 GRO J1655–40

This is the only other source of our sample with multiple overall detections: 4 out of 11 single-trial detections. The frequency of the QPO is also bimodal: between 273 Hz and 313 Hz for the low-frequency peak (Q between 3 and 4, rms slightly above 1%) and 446 Hz for the high-frequency peak (Q=12 and 6%

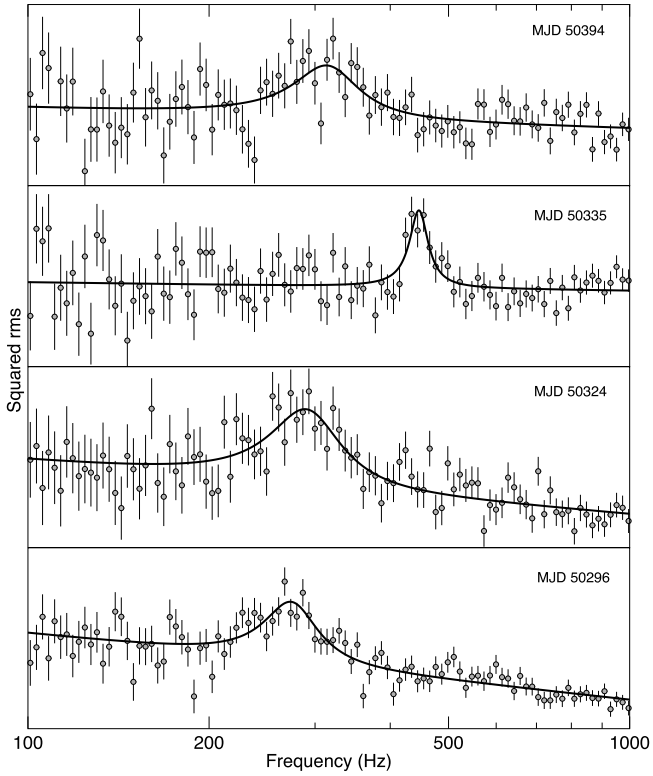

Figure 4.3: PDS of the four good detections of HFQPO for GRO J1655–40 with the corresponding best fit models.

rms). From Fig. 4.4 it is evident that all detections correspond to the "anomalous state" at very high fluxes (see Belloni, 2010). The PDS is also typical of that state. As in the case of XTE J1550–564, the HID points are distributed along a diagonal line. Overall, the four detections with high significance after correction for number of trials show quite a range of frequencies: 274, 290, 313 and 446 Hz.

Detections of HFQPO in the 1996 outburst of GRO J1655–40 were reported by Remillard et al. (1999). They detect six features in single observations, in addition to the analysis of sets of combined observations, obviously not comparable with our results. Four of their detections correspond to entries in our Tab. 4.2, one corresponds to our 443 Hz observation at MJD 50317, but at a different frequency (294 Hz); our detection is from the hard band, while theirs is from the total band. In the total band we do detect their signal, but just below 3σ single trial. The same is for the observation at MJD 50383.

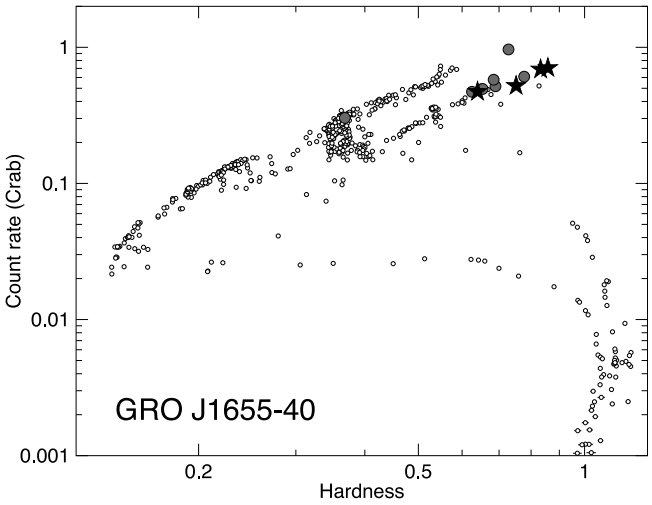

Figure 4.4: Hardness-Intensity Diagram for GRO J1655–40 (see Fig. 4.2).

As in the case of XTE J1550–564, Remillard et al. (1999) give no details on the detections, nor on the procedure followed. Two of our detections do not appear in their sample. The observation from MJD 50394 does not appear in their list, while that from MJD 50335 is a very significant peak at 446 Hz in our data, but in the hard band. Nothing can be seen in the total band, so our result is consistent with theirs. This last one is the observation where the ∼450 Hz QPO was discovered (Strohmayer, 2001a). All other observations from Strohmayer (2001a) appear in our sample, although for MJD 50311 the high-frequency peak found by Strohmayer appears slightly below our 3σ level.

4.3.3 XTE J1859+226

Only one feature appears in our sample, at a single trial probability of 2.7×10^{-4}, which translates in a very high final chance probability. This feature is very unlikely to be real. The source appears at intermediate hardness in the HID (see Fig. 4.5); the presence of a type-B QPO indicates that the source was in the SIMS. Cui et al. (2000) report three detections of HFQPOs. None of these QPO appears in our sample. Two of them appear to be below our $> 3\sigma$ single-trial threshold in their table (the significance is computed as the ratio between normalisation and its lower-side error, while using fractional rms as done by Cui et al. (2000) increases the value by a factor of two because of the error propagation), while the third one is a very broad feature which is automatically discarded by our procedure.

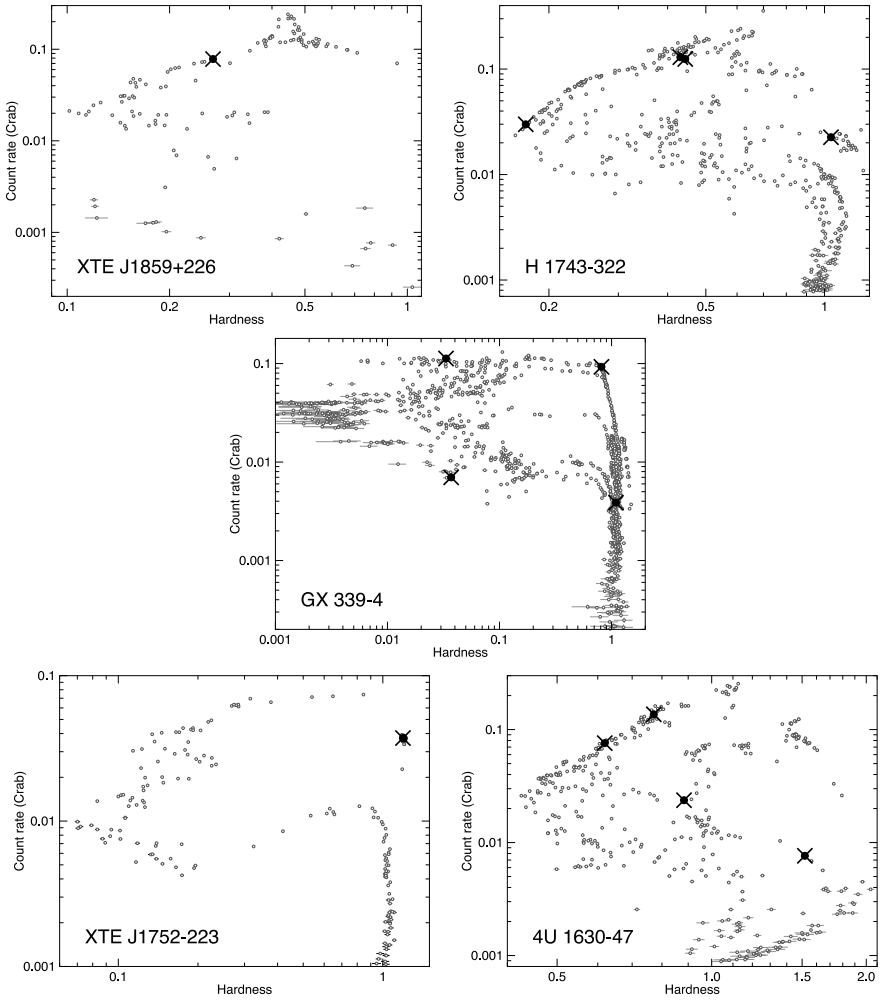

Figure 4.5: Hardness-Intensity Diagram for the remaining sources for which no HFQPO with chance probability $< 1\%$ was found after accounting for the number of trials. Observations with HFQPOs with chance probability $> 1\%$ are marked with thick circles and crosses.

4.3.4 H 1743-322

We detect four QPOs, with high final chance probability. From Fig. 4.5 we can see that in one case the source was in a very soft HSS, in one case the source was rather hard (the full PDS shows a type-C QPO, from which we conclude the source was in the HIMS), and in two cases the source showed intermediate hardness, and was in a similar location in the HID as the ones discussed for GRO J1655–40 and XTE J1550–564. In these last two cases the full PDS shows a strong type-B QPO, and therefore the source was in the SIMS.

HFQPOs were reported from H 1743-322 by Homan & Belloni (2005) at 163 and 240 Hz from the observations of MJD 52787. They do not appear in our sample, but accumulation of more than one observation is needed to obtain a detection, so our results are not inconsistent with theirs. The same applies to the detection of Remillard et al. (2006b).

4.3.5 GX 339–4 and XTE J1752–223

For GX 339–4, the fur detections form a square in the HID (see Fig. 4.5). The two hard ones are obviously LHS. The two soft ones are HSS. For XTE J1752–223 the two detections are at the same high value of hardness, in the LHS. In these two case the chance probability was, respectively, 0.23 and 0.035. These are most likely statistical fluctuations and therefore we do not discuss them further.

4.3.6 4U 1630–47

None of the four peaks in Tab. 4.2 appear to be statistically significant after the (large) number of trials is taken into account. Two peaks are detected when the source flux was low: in one case the source was in the LHS, while in the other case the full PDS shows very little noise, making it difficult to classify the state. The remaining two observations lie along a diagonal branch in the HID and also show low noise level. High-frequency features in this source were reported by Klein-Wolt et al. (2004). Those are very broad features which depend crucially on the subtraction of Poissonian noise. However, all of them were obtained after averaging observations corresponding to different intervals in the 1998 outburst and therefore cannot appear in our sample.

4.3.7 XTE J1650–500

We did not obtain detections for this source. Homan et al. (2003) report high-frequency features, some of which very broad like in the case of 4U 1630–47.

Once again, considerable averaging of more observations has been performed, which explains the absence of detections in our sample.

4.4 Discussion

We analysed 7108 RXTE/PCA observations of 22 black-hole transients searching for HFQPO. From the whole sample, after taking into account the number of trials due to the many observations for each source and the number of independent frequencies sampled, we obtain only 11 detections with a chance probability less than 1%. These detections belong to two sources: XTE J1550–564 (7) and GRO J1655–40 (4). The small number of detections (including single-trial detections at significance higher than 3σ there are only 42), confirms that these are very elusive signals, as already indicated by the small number of detections reported in the literature. A few additional detections were obtained by other authors by averaging observations according to hardness, but those cases will not be discussed here. From our detections, a number of aspects can be discussed.

All detections correspond to PDS from very specific states. Six out of seven detections for XTE J1550–564 are from the SIMS, while the last one corresponds to the high-soft state (HSS). One observation has a clear type-B QPO, three have a type-A QPO and one corresponds to the bright flare in 1998, where a LFQPO can be tentatively identified with type-A (see Remillard et al., 2002b). No type-C QPO is detected simultaneous to one of the HFQPO. The first five HFQPO are from the 1998 outburst, the last two from the 2000 outburst (see Rodriguez et al., 2004). The four detections from GRO J1655–40 correspond to the "anomalous state" described in Belloni (2010). Again, no type-C QPO can be identified in those four PDS. These detections come all from the 1996 outburst (Remillard et al., 1999). From the HIDs in Figs. 4.2 and 4.4, we see that the points corresponding to the HFQPO detections in both sources are distributed diagonally. However, it is difficult to relate this to precise spectral characteristics.

For XTE J1550–564, the centroid frequencies of the detected QPOs appear to cluster around two values: ∼180 Hz and ∼280 Hz. Interestingly, the low-frequency detections come from the total energy band, while the high-frequency detections come from the hard band, indicating that the high-frequency oscillation has a harder spectrum. Moreover, inspection of Fig. 4.3 shows that the low-frequency peaks are clearly broader than the high-frequency ones.

For GRO J1655–401, the dichotomy 300-450 Hz seems to be less sharp. Strohmayer (2001a) detected the ∼450 Hz feature simultaneous with the 300

Hz one when averaging observations, showing that the two peaks correspond to different time scales. We see also frequencies (∼270 and ∼290 Hz) significantly lower than 300 Hz. Also in this source the high-frequency detection is significantly narrower than those at lower frequencies.

The fact that the few available detections appear at more or less the same frequencies for XTE J1550–564, even for different outbursts, and that the upper peak is narrower than the lower make a comparison with kHz QPO in neutron-star binaries difficult. There, the centroid frequencies are observed to vary in a way consistent with a random walk (see Belloni et al., 2005, 2007) and the upper peak is broader than the lower one (see e.g. Belloni et al., 2005).

Two sources which are known to show HFQPOs were excluded from the analysis. GRS 1915+105 is a very peculiar system with many observations and many HFQPO detections. We will present our results on this source in a forthcoming paper. IGR J17091–3624 is a new "twin" of GRS 1915+105, in the sense that it is the only other known source to display its unusual variability. Results were already published in Altamirano et al. (2011).

It is interesting to compare our results with those of kHz QPOs in neutron-star LMXBs (see van der Klis, 2006, for a review). The neutron-star system 4U 1636–53 was observed regularly during the last few years of the RXTE lifetime, yielding a solid database from which to extract statistical information. In this source, ∼40% of the observations led to the detection of at least one high-frequency feature (see Sanna et al., 2012a) as opposed to 0.15% here.

Sunyaev & Revnivtsev (2000) showed that there is a systematic difference in power level between black-hole and neutron-star sources in the hard state, attributing it to the presence of a radiation-dominated spreading layer in the latter, the so-called boundary layer. As already suggested by these authors, the presence/absence of strong high-frequency QPOs can be part of the same picture. Following this line, Gilfanov et al. (2003) and Gilfanov & Revnivtsev (2005) analysed low-frequency and kHz QPOs in neutron-star binaries and concluded that the oscillations are caused by variations in the luminosity of the boundary layer. In this framework, it is the diminishing relative importance of the boundary-layer emission which weakens kHz QPO as they move to very high frequencies (see Méndez, 2006, for additional discussion). Moreover, our HFQPOs are detected in intermediate states. Belloni et al. (2007) and Sanna et al. (2012a) showed that in the neutron-star LMXB 4U 1636–53 kHz QPOs are not found in the observations when the source is the hardest, at intermediate hardness mostly the upper kHz QPO is detected and in the softest observations mostly the lower kHz QPO is present. It is difficult to make a comparison with our case: that no kHz QPOs are detected in the hard state is consistent with the black-hole case, while a detailed comparison between soft

states remains to be done.

The detection of only a few specific frequencies in the case of black-hole HFQPOs is something that does not apply to kHz QPOs in neutron-star binaries. The frequencies of kHz QPO are distributed along a very broad range (see van der Klis, 2006; Méndez, 2006; Barret et al., 2005b; Belloni et al., 2007; Barret et al., 2007). KHz QPOs in neutron stars are usually strong, more easily detected than HFQPO, which then leads to a much larger number of detections. Moreover, at most frequencies the lower kHz peak is narrower and more significant than the upper one. The question is whether the frequencies of the oscillations can be understood in terms of the same physical mechanisms in the two classes of sources. In order to check what frequencies would be observed if this was the case, in Fig. 4.6 we plot the distribution of upper and lower kHz QPOs in the full RXTE database of 4U 1636–53 (data from Sanna et al., 2012a). In both panels, the black histogram contains only the strongest detected peaks (we chose an rms threshold of 15% and 10% for the upper and lower peaks respectively in order to select only a handful of detections). A comparison with the HFQPOs of XTE J1550–564 is interesting. There, the lower-frequency HFQPO is weaker and broader than the higher-frequency one. Unfortunately, the only reported case of a double-detection in XTE J1550–564, obtained through averaging of many observations, does not allow a good determination of the quality factor of the two peaks (Miller et al., 2001). The black histograms show that on average the strongest upper kHz QPOs in 4U 1636–53 appear at a lower frequency than the strongest lower kHz QPOs. This is consistent with the spread of the frequencies we find in XTE J1550–564. Clearly, the limited number of detections of XTE J1550–564 does not allow a more precise comparison.

The width of the QPO peaks is another interesting quantity of a comparison with neutron-star binaries. In our detections, the Q factor of the upper-frequency peak is higher than that of the lower-frequency one. In neutron-star binaries it is generally the opposite (see e.g. Barret et al., 2007). This is a clear difference between the neutron-star and black-hole cases. If the process originating the oscillations is the same of the two classes of courses, the presence of the boundary layer is likely to be the reason for this difference, yielding another observational constraint for theoretical modelling (see Méndez, 2006).

Overall, we detected eleven significant features after analysing around 7000 observations, resulting in a detection efficiency of $\sim 10^{-3}$. Of course, since the HFQPOs are detected only in intermediate states and these states are the short-lived ones, observing with new instruments and concentrating on the most likely periods during outbursts can increase the probability of detection. In other words, to detect HFQPOs one does not need a good coverage of a

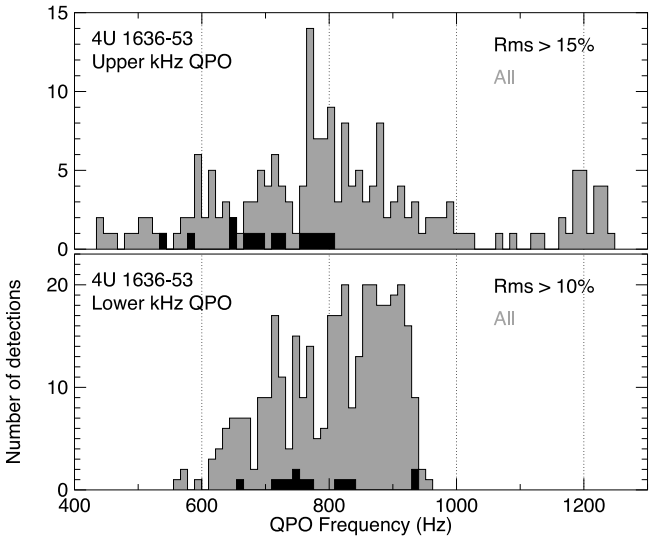

Figure 4.6: Frequency distributions for all detections of upper (top panel) and lower (bottom panel) kHz QPOs in the NS LMXB 4U 1636–53 (Sanna et al., 2012a) (grey histograms). The black histograms include only detections with rms >15% for the upper and >10% for the lower.

full outburst, but only of the intermediate states. The LAXPC instrument on board the upcoming ASTROSAT mission (Agrawal, 2006) will increase the effective area of the PCA above 10 keV, where the HFQPOs are stronger (see Morgan et al., 1997), but in order to be effective ASTROSAT will have to concentrate observations during bright intermediate states. The LOFT mission (Feroci et al., 2010), under evaluation by ESA at the time of writing, is planned with a very large effective area (around 12 m^2) and will allow sampling of these weak signals in all states.

Acknowledgment. The research leading to these results has received funding from the European Community's Seventh Framework Programme (FP7/2007-2013) under grant agreement number ITN 215212 'Black Hole Universe'. This paper was written during an extended stay of TMB at The University of Southampton, funded by a Leverhulme Trust Visiting Professorship. TMB thanks S. Motta for her help with source states.

5 Broad iron line in the fast spinning neutron-star system 4U 1636–53

— **Andrea Sanna, Beike Hiemstra, Mariano Méndez, Diego Altamirano, Tomaso Belloni, Manuel Linares** —

submitted to MNRAS

Abstract

We analysed the X-ray spectra of six observations, simultaneously taken with *XMM-Newton* and *Rossi X-ray Timing Explorer (RXTE)*, of the neutron star low-mass X-ray binary 4U 1636–53. The observations cover several states of the source, and therefore a large range of inferred mass accretion rate. These six observations show a broad emission line in the spectrum at around 6.5 keV, likely due to iron. We fitted this line with a set of phenomenological models of a relativistically broadened line, plus a model that accounts for relativistically smeared and ionised reflection from the accretion disc. The latter model includes the incident emission from both the neutron-star surface or boundary layer and the corona that is responsible for the high-energy emission in these systems. From the fits with the reflection model we found that in four out of the six observations the main contribution to the reflected spectrum comes from the neutron-star surface or boundary layer, whereas in the other two observations the main contribution to the reflected spectrum comes from the corona. We found that the relative contribution of these two components is not correlated to the state of the source. From the phenomenological models we found that the iron line profile is better described by a symmetric, albeit broad, profile. The width of the line cannot be explained only by Compton broadening, and we therefore explored the case of relativistic broadening. We further found that the direct emission from the disc, boundary layer, and corona generally evolved in a manner consistent with the standard accretion disc model, with the disc and boundary layer becoming hotter and the disc moving inwards as the source changed from the hard in to the soft state. The iron line, however, did not appear to follow the same trend.

5.1 Introduction

The X-ray spectrum of low-mass X-ray binaries (LMXBs) shows evidence of an accretion disc extending down close to the central object (see e.g., review by Done et al., 2007). The disc is assumed to be optically thick and geometrically thin, and is characterised by a thermal spectrum with typical temperatures of 0.2–1 keV (Shakura & Sunyaev, 1973). The thermal disc photons are Compton up-scattered in a hot coronal gas surrounding the disc and compact object, giving rise to the hard component usually seen in the spectrum (e.g., Barret et al., 2000, and references therein). However, a fraction of these Comptonized photons is backscattered, and they irradiate the accretion disc. After being absorbed, reprocessed and re-emitted, these photons produce a reflection spectrum consisting of a continuum plus a complex line spectrum (see review by Fabian & Ross, 2010). Due to the high fluorescence yield and abundance, an important feature of the reflection spectrum is the Fe Kα line at $\sim$6–7 keV. As a result of disc rotation and relativistic effects near the compact object, the reflection spectrum is blurred, with the Fe line being asymmetrically broadened (Fabian et al., 1989). As the disc moves close to the central compact object, the relativistic effects become stronger, and consequently, the red wing of the Fe line – mainly set by the gravitational redshift at the inner edge of the disc – extends to lower energies. Hence, modelling of the iron line profile allows us to measure the size of the inner disc radius, which determines other spectral and timing properties of the source (e.g., disc temperature, characteristic frequency of the variability). If the compact object is a black hole (BH), modelling of the Fe line profile in the disc-dominated spectral state provides an estimate of the BH spin (see e.g., Miller, 2007; Reynolds & Fabian, 2008), assuming that the disc is truncated at the innermost stable circular orbit (ISCO). In case of a neutron star (NS), a measurement of the inner edge of the disc sets directly an upper limit on the NS radius, as the inner disc radius has to be larger than, or equal to, the equatorial radius of the star (see e.g., Bhattacharyya & Strohmayer, 2007; Cackett et al., 2008).

Since the first detection of a broad and asymmetric Fe emission line in the Seyfert-1 galaxy MCG–6–30–15 (Tanaka et al., 1995), many similar lines have been observed in BH systems, both in Active Galactic Nuclei (AGN) and in X-ray binaries (see reviews by Fabian et al., 2000; Miller, 2007). In all cases the line appears to be produced very close to the BH. Broad Fe lines are also detected in NS systems although they are weaker than in BH systems. With instruments like *Chandra*, *XMM-Newton* and *Suzaku*, relativistically broadened Fe emission lines have been observed in many NS LMXBs (e.g., Piraino et al. 2007; Cackett et al. 2008; Pandel et al. 2008; di Salvo et al.

2009; Cackett et al. 2010; see also Ng et al. 2010 for an almost complete list of NS LMXBs with Fe lines detected with *XMM-Newton*).

Relativistically broadened Fe lines in NS spectra are usually fit using a phenomenological model for either a Schwarzschild or (maximum) Kerr metric, where the underlying continuum is modelled with a variety of direct emission components (see e.g. Bhattacharyya & Strohmayer, 2007; Lin et al., 2007; Pandel et al., 2008; Cackett et al., 2008). However, as the Fe emission line is a reflection signature, it should be accompanied with a reflection continuum extending over a wide bandpass; at the same time, the line and its reflection continuum should self-consistently determine the ionisation balance of the disc and include Compton scattering (e.g., George & Fabian, 1991; Ross & Fabian, 1993; Ross et al., 1999). An inappropriate modelling of the underlying continuum, as well as not including any of these processes in the analysis, could lead to incorrect results from the line modelling. Therefore, a self-consistent ionised reflection model should be used to study the continuum and Fe emission line in the spectra of LMXBs. (Note that, depending on the quality of the data, reflection and phenomenological models could describe the data equally well, even leading to reasonable results for the phenomenological model; see e.g., Cackett et al. 2010.) Furthermore, the shape of the reflection spectrum not only depends on the ionisation state of the surface layers of the disc, but also on the spectral shape of the emission illuminating the accretion disc. Comptonized emission from the (disc) corona is the commonly assumed source of irradiation, but in the case of an accreting NS, the emission from the NS surface/boundary layer, can be as well irradiating the accretion disc. Cackett et al. (2010) have studied a number of broad Fe emission lines in NS LMXBs where they used a blurred reflection model in which the blackbody component – used to mimic the emission from the boundary layer – was assumed to be the incident emission. Cackett et al. (2010) found that this model fits the data well in most cases, supporting the idea that the boundary layer is indeed illuminating the disc (see also D'Aì et al., 2010). In our analysis (below), we test whether a disc corona or boundary layer was the most likely source of irradiation. We note that relativistic (plus Compton) broadening is not the only physical explanation for the width and the profile of iron lines in compact objects. For instance, Titarchuk et al. (2003) proposed that asymmetric line profiles could originate from an optically thick flow launched from the disc, which expands or contracts at relativistic speeds. We will not explore this possibility in the paper, but refer the reader to the discussion in Ng et al. (2010).

We study the Fe emission line and the reflection spectrum in six observations of the NS-LMXB 4U 1636–53, taken with the *XMM-Newton* and the

RXTE satellites simultaneously. Besides the direct emission components, we fit these data using both phenomenological models and a relativistically-smeared ionised reflection model in which we investigated different sources of irradiation. In what follows, we first introduce the source 4U 1636–53, focusing on quantities relevant for this paper. In Section 5.2 we give details on the data used, and the procedure we followed to reduce them. In Section 5.3 we describe the models, and explain the specific aspects of the spectral analysis. Here we also summarise the most important findings. We discuss our results and their implication on the standard accretion disc model in Section 5.4. There we also address the impact of the NS surface/boundary layer, on the reflection spectrum for the different spectral states. Furthermore, in that section we also discuss the results from the phenomenological line models. In Section 5.5 we summarise our results.

5.1.1 4U 1636–53

Since its discovery in 1974 (Willmore et al., 1974; Giacconi et al., 1974), 4U 1636–53 has been observed over a wide range of wavelengths. Photometry of the optical counterpart (V801 Ara) revealed a short orbital period of ∼3.8 hr and a companion star with a mass of ∼0.4 $M_\odot$ (van Paradijs et al., 1990; Giles et al., 2002). X-ray studies of 4U 1636–53 have shown a variety of rapid time variability, including *i)* thermonuclear X-ray bursts (e.g., Hoffman et al., 1977; Galloway et al., 2006; Zhang et al., 2011), confirming the presence of a NS as the compact object, *ii)* millisecond oscillations during the X-ray bursts, indicating a spin frequency of ∼581 Hz (Zhang et al., 1997; Giles et al., 2002; Strohmayer & Markwardt, 2002), and *iii)* kHz quasi-periodic oscillations (kHz QPOs, e.g., Wijnands et al., 1997; Belloni et al., 2007; Altamirano et al., 2008a; Sanna et al., 2012a). From Eddington limited X-ray bursts, assuming a NS mass of 1.4 $M_\odot$ and a stellar radius of 10 km, Galloway et al. (2006) estimated the distance to 4U 1636–53 to be 6.0 ± 0.5 kpc. Combining burst oscillations with phase-resolved optical spectroscopy of 4U 1636–53, Casares et al. (2006) estimated the mass function and mass ratio to be $f(M) = 0.76 \pm 0.47 M_\odot$ and $q = 0.21$–0.34, respectively, where $q = M_2/M_1$ with M_2 the mass of the donor and M_1 the mass of the NS. Casares et al. (2006) also showed that for a 0.48 $M_\odot$ donor, the NS mass is 1.6–1.9 $M_\odot$ and the inclination $i \simeq 60$–$71°$. The latter result is in conflict with the model of Frank et al. (1987) as the lack of X-ray dips in the light curve of 4U 1636–53 sets an upper limit on the inclination of $i \leq 60°$. However, in this model the derived upper limit for the inclination depends on the location where the dips are formed, and since the exact geometry is not known the minimum inclination to observe dips could be slightly larger. On the other hand, the inclination could not be

larger than $\sim 75^{\circ}$ since this would probably cause eclipses, which are not seen in this source.

4U 1636–53 is a persistent X-ray source, although it shows variations in intensity up to a factor of 10, following a narrow track in the colour-colour diagram (CD) and hardness-intensity diagram (HID; Belloni et al., 2007; Altamirano et al., 2008a) with a ∼40-d cycle (Shih et al., 2005; Belloni et al., 2007). The transition through the CD (or HID) is thought to be driven by changes in the mass accretion rate. The two distinct spectral states (hard, at the top right of the CD, and soft, at the bottom of the CD) are attributed to a different accretion flow configuration. In the soft state, where the X-ray intensity is high, the disc is hot and ionised, with an inner radius extending down to the ISCO (or down to the stellar surface in case the ISCO is within the NS, see e.g., Done et al. 2007). As the intensity gradually decreases, the mass accretion rate eventually becomes too low to ionise the full accretion disc. The outer disc regions cool down, the viscosity decreases, and the overall mass accretion rate is reduced. Eventually, mass accretion rate at the inner regions of the disc decreases, leading to a receding inner edge and the X-ray intensity reaches its minimum. The inner regions are likely replaced by a hot corona, and the spectrum hardens, which is the characteristic that defines the hard state. In the mean time, the secondary keeps transferring mass to the disc causing the density and temperature to increase, hence enhancing the viscous stress, and the mass accretion rate increases again. Eventually the disc gets ionised, the source rebrightens and makes a transition to the soft state. Shih et al. (2005) have shown that this re-brightening cycle for 4U 1636–53 of ∼40 days is consistent with the viscous time-scale in the outer disc.

High signal-to-noise and moderate-resolution spectra of 4U 1636–53 revealed broad, asymmetric Fe emission lines. Pandel et al. (2008) analysed three *XMM-Newton/RXTE* observations, once when the source was in the transitional state (between the hard and the soft state), and twice when it was in the soft state. In all three spectra they found that the Fe line profile is consistent with a relativistically broadened line coming from the inner disc, which appeared to be at the ISCO for a non-rotating NS. This finding is partly contested by Cackett et al. (2010) who fit the same spectra with a blurred reflection model that includes effects like Compton broadening and line emission from relevant elements. Cackett et al. (2010) showed that fitting the spectrum with a self-consistent reflection model resulted in slightly larger values for the inner disc radius than when the spectrum was fit with the phenomenological DISKLINE model (Fabian et al., 1989) used by Pandel et al. (2008). Nonetheless, both the results of Pandel et al. (2008) and Cackett et al. (2010) are based on data which were not corrected for pileup effects. As demonstrated by Ng

et al. (2010), re-analyses of the same *XMM-Newton* data considering pileup and background effects, suggested a different iron line profile. Ng et al. (2010) found that the Fe lines in the three spectra of 4U 1636–53 used by Pandel et al. (2008) appeared to be symmetric and could be well fit with a Gaussian profile, although, due to the statistics, a relativistic origin of the line could not be excluded. However, Ng et al. (2010) did not include the simultaneous *RXTE* data in their fits, which can affect the Fe emission line profile that strongly depends on the underlying continuum. Triggered by the debate about the Fe line in 4U 1636–53, we obtained and analysed new *XMM-Newton/RXTE* observations of 4U 1636–53, and re-analysed the previous *XMM-Newton/RXTE* data of 4U 1636–53. We investigated and corrected for instrumental effects, used a wide bandpass spectrum (0.8–120 keV), and fit the Fe emission line with the most commonly used phenomenological model and with a relativistically blurred ionised reflection model which self-consistently includes Compton broadening. Additionally, for the first time in Fe line studies, we investigated the contribution of different sources of disc illumination that could produce the reflection spectrum, and their contribution in the different spectral states.

All together, 4U 1636–53 is an interesting source exhibiting several features that could be used to constrain key parameters like the NS mass and radius, as well as to test the standard NS accretion picture described by the colour-colour diagram. Comparing the properties of the Fe line as a function of spectral state – or even more specifically with the general properties of the spectrum like luminosity, blackbody temperature of disc and boundary layer – may help us to constrain the origin of the line emission region. Furthermore, kHz QPOs are seen to vary in frequency depending on the spectral state of the source (see e.g., Belloni et al., 2007; Altamirano et al., 2008a; Sanna et al., 2012a). Therefore, connecting the position in the CD with the Fe line properties and the kHz-QPO frequencies, may help to break the degeneracy in the models used to explain the spectral and timing features in accreting NS systems. In this paper, however, we focussed on the spectral analysis and the Fe line properties as this requires a careful investigation. In a companion paper (Sanna et al. 2013, in prep., Chapter 6) we combine the results of the spectral analysis presented in this paper with the timing analysis of the simultaneous *RXTE* observations.

5.2 Observations and data reduction

4U 1636–53 has been observed with *XMM-Newton* nine times in the last decade (between 2000 and 2009). The first two observations were taken with all CCD cameras operated in imaging mode and were strongly affected by pileup. In the

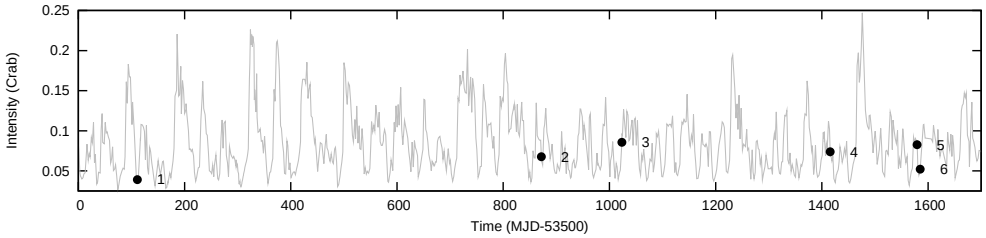

Figure 5.1: Long-term light curve of 4U 1636–53 based on pointed *RXTE*/PCA observations of the last ∼5 years. The intensity is the 2–16 keV Crab normalised PCA count rate (see Section 5.2.2). The numbered points mark the six *XMM-Newton* observations, with the numbers corresponding to the observations given in Table 5.1.

other seven observations, of all the CCD cameras only the EPIC-pn (hereafter PN; Strüder et al., 2001) camera was on, operating in timing mode. In this mode one of the dimensions of the CCD is compressed into one single row to increase the read out speed. In our spectral analysis we only used the *XMM-Newton* data taken with PN in timing mode. We did not include the high-resolution data from the Reflection Grating Spectrometer in the energy range 0.33–2.5 keV. We note that the *XMM-Newton* observation taken on March 14, 2009 had a flaring high-energy background during the full ∼40 ks exposure, and we therefore did not include this observation in our spectral analysis.

Since 1996 *RXTE* observed 4U 1636–53 more than a 1000 times; from March 2005 the source was regularly observed for ∼2 ks every two days (for the first results of this monitoring campaign see Belloni et al., 2007). For our spectral analysis we only included the ten *RXTE* observations that were taken simultaneously with *XMM-Newton*. In Table 5.1 we give an overview of the observations, labelled in a chronological order. Using the pointed *RXTE*/PCA observations of the last ∼5 years, in Figure 5.1 we show the long-term light curve of 4U 1636–53 on which we marked the moments of the *XMM-Newton* observations used in this paper.

5.2.1 XMM-Newton data reduction

For the *XMM-Newton* data reduction we used the tasks of the Science Analysis System (SAS) version 12.1, applying the latest calibration files (xmmsas_20120523). To generate the concatenated and calibrated PN event files we used the meta-task `epproc`. We corrected for rate-dependent charge trans-

Table 5.1: *XMM-Newton*/*RXTE* observations of 4U 1636–53 used in our analysis

Observation	Instrument	Identification Nr.	Start Date	Start Time	Exposure (ks)*
Obs. 1	*XMM-Newton*	0303250201	29-08-2005	18:24:23	25.7
	RXTE	91027-01-01-000		16:35:28	26.2 (PCA)
					9.0 (HEXTE)
Obs. 2	*XMM-Newton*	0500350301	28-09-2007	15:44:56	14.3
	RXTE	93091-01-01-000		14:47:28	26.9 (PCA)
					8.8 (HEXTE)
Obs. 3	*XMM-Newton*	0500350401	27-02-2008	04:15:37	34.7
	RXTE	93091-01-02-000		03:46:56	25.3 (PCA)
					8.3 (HEXTE)
Obs. 4	*XMM-Newton*	0606070201	25-03-2009	22:59:30	23.8
	RXTE	94310-01-02-03		23:00:32	1.9 (PCA)
	RXTE	94310-01-02-04	26-03-2009	00:39:28	1.6 (PCA)
	RXTE	94310-01-02-05		02:17:36	1.4 (PCA)
	RXTE	94310-01-02-02		03:54:24	1.3 (PCA)
					2.2 (HEXTE)^a
Obs. 5	*XMM-Newton*	0606070301	05-09-2009	01:57:03	32.8
	RXTE	94310-01-03-000		01:17:36	16.6 (PCA)
	RXTE	94310-01-03-00		08:20:32	7.3 (PCA)
					7.6 (HEXTE)^a
Obs. 6	*XMM-Newton*	0606070401	11-09-2009	08:48:11	21.1
	RXTE	94310-01-04-00		08:42:24	18.4 (PCA)
					5.7 (HEXTE)^a

* Final exposure time after excluding X-ray bursts, detector drops, and background flares; see Section 5.2.1 and 5.2.2 for more details.
^{a} Total exposure time of the combined HEXTE data; see Section 5.2.2 for more information.

fer inefficiency (CTI) effects using `epfast`, and we filtered out X-ray bursts, telemetry drops, and intervals of flaring high-energy background.

For the latter, we excluded time-intervals in which the 10–12 keV count rate for single events (PATTERN=0) was larger than 1 cts s^{-1}. We generated a time-averaged source spectrum per observation, using single and double events only (PATTERN ≤ 4), excluding events at the edge of the CCD and at the edge of a bad pixel (FLAG=0), and using events within a 17-column wide box, centred on the source position, for which the central 3 columns were excised in order to correct for pileup effects (removing $\sim$70% of the detected photons). We excised the central 5 columns for Obs. 2 and Obs. 3 (removing $\sim$90% of the detected photons; see Appendix 5.7 for details). We generated the response matrices using the task `rmfgen`. Following the recommendations given in the SAS User guide (Chapter 4.6.1)[1] for piled-up observations in timing mode, we produced the ancillary response files using the task `arfgen`. For PN timing mode observations, the point spread function (PSF) of the telescope extends further than the CCD boundaries, and extracting the background spectrum from the outer regions of the CCD leads to a spectrum contaminated with

[1] `http://xmm.esac.esa.int`

source photons (see Hiemstra et al., 2011; Ng et al., 2010, for a discussion on contaminated background spectra). To model the background, we extracted a spectrum from the outer region of the CCD (RAWX in 5–20) of a "blank field" observation instead (see Ng et al., 2010; Hiemstra et al., 2011). Based on similar sky coordinates and column density along the line of sight, we used the timing mode observation of the BH GX 339–4 (Obs 0085680601), in which the source was not significantly detected, as our "blank field" for all six *XMM-Newton* observations. Finally, we rebinned the source spectra such that we oversampled the PN energy resolution by a factor of 3 ensuring that we have a minimum of 25 counts per bin.

5.2.2 RXTE data reduction

Energy spectra

For the *RXTE* data reduction we used the HEASOFT tools version 6.10, following the recipes in the *RXTE* cook book[2]. Applying the standard screening criteria and excluding time-intervals of detector drop-outs and X-ray bursts, we used the tool `saextrct` to extract the PCA spectra from Standard-2 data, where we only included events from the third proportional counter unit (PCU2) being this the best-calibrated detector. We corrected for PCA deadtime, and applied a 0.6% systematic error to the PCA data. The PCA background was estimated with the tool `pcabackest` and the response files were generated using `pcarsp`. After excluding detector drop-outs and X-ray bursts, we produced the HEXTE spectra for cluster-B events only, using the script `hxtlcurv`. With the tool `hxtrsp` we generated the HEXTE response files. No systematic errors were added to the HEXTE data. For the observations starting on March 25 and September 5, 2009 (Obs. 4 and Obs. 5, respectively), *RXTE* did not cover the full *XMM-Newton* observation but several shorter exposures were taken instead. To speed up the fitting, we used the PCA spectrum with longest exposure, since all the spectra were consistent with each other within errors. However, in order to improve the poor HEXTE statistics we combined the individual HEXTE spectra with the tool `sumpha`. Net exposures of the final used PCA and HEXTE data are given in the last column in Table 5.1.

Intensity and Colours of 4U 1636–53

We calculated X-ray colours and intensity of 4U 1636–53 using the Standard-2 PCA data. The intensity represents the 2–16 keV count rate, and soft and hard

[2] `http://heasarc.gsfc.nasa.gov/docs/xte/recipes/cook_book.html`

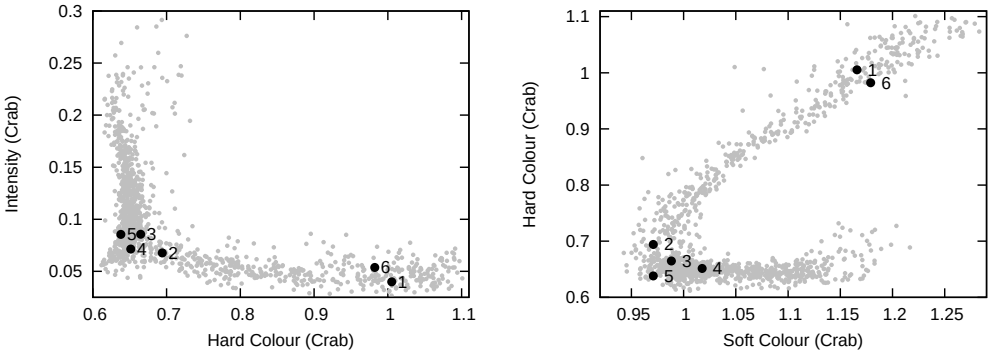

Figure 5.2: Hardness-Intensity diagram (*left*) and colour-colour diagram (*right*) of 4U 1636–53. Each grey point represents the averaged Crab-normalised colours and intensity per observation, for a total of 1281 observations (see text in Section 5.2.2 for details). The numbered black points mark the position of the six *XMM-Newton* observations, with the numbers corresponding to the observations given in Table 5.1.

colours are defined as the count rate ratio in the energy bands 3.5–6.0 keV / 2.0–3.5 keV and 9.7–16.0 keV / 6.0–9.7 keV, respectively. To obtain the exact count rate in each of these energy bands we interpolated linearly in channel space. To correct for the gain changes and differences in the effective area between the PCUs, as well as to correct for the differences due to changes in the channel-to-energy conversion of the PCUs as a function of time, we normalised by the Crab Nebula values obtained close in time to our observations (for details see Kuulkers et al., 1994; Altamirano et al., 2008a). We finally averaged the normalised colours and intensity per PCU for the full observation using all available PCUs.

In Fig 5.2 we show the HID and CD of 4U 1636–53, with each point representing the average intensity, hard and soft colours per observation for a total of 1281 observations, up to May 2010. In these diagrams we also marked the position of the source at the time of the *XMM-Newton* observations. Based on the position of the source in both diagrams, we concluded that Obs. 1 and Obs. 6 were in the hard state, also referred to as the transitional state (Lin et al., 2007), characterised by a relatively high hard colour and low X-ray intensity. The positions of Obs. 2–5 were consistent with the soft state (van der Klis, 2006; Lin et al., 2007), where both colours almost reach their minimum values and the X-ray intensity is moderate. Following Lin et al. (2007), in the rest of this paper we refer to Obs. 1 and Obs. 6 as the transitional-state observations, and we refer to Obs. 2–5 as the soft-state observations.

5.3 Spectral analysis and results

For the spectral fitting of the *XMM-Newton/RXTE* data of 4U 1636–53, we used XSPEC version 12.7.1 (Arnaud, 1996). To study the evolution of the Fe emission line and its underlying continuum as a function of the spectral state, we fit each of the individual observations with a set of phenomenological models and a relativistically smeared reflection model in addition to the direct emission components (see following Sections for the model description). In order to study the Fe line properly, we need to have a well-defined continuum on both sides of the Fe bandpass. For that reason we fit the *XMM-Newton/RXTE* spectra in the 0.8–120 keV bandpass, with PN covering the 0.8–11 keV range (from channel 27 up to channel 267, unless otherwise mentioned), PCA taken in the 10–25 keV band (from channel 22 and 53), and HEXTE covering the 20–120 keV range (between channels 11 and 45). Spectral uncertainties are given at 90% confidence ($\Delta\chi^2 = 2.706$ for a single parameter).

In all our fits we included a PHABS component to account for interstellar absorption, using the abundances and photo-electric cross section of Wilms et al. (2000) and Verner et al. (1996), respectively. Additionally, to account for flux calibration disparities between the different instruments, we added a multiplicative constant to the model.

5.3.1 Spectral model

Direct emission

Spectral modelling of accreting NSs has been, and still is, a controversial matter. A variety of models have been proposed in the past years. All models, however, include at least a soft/thermal and a hard/Comptonized component that vary according with the source state. The soft/thermal emission comes from the accretion disk and from the NS surface, and are typically modelled with a multicolour disk blackbody (Mitsuda et al., 1984) and a blackbody, respectively. The hard/Comptonized emission is probably created by the upscattering of soft photons coming either from the accretion disk, the NS surface, or both simultaneously, in the hot electron gas surrounding the central region of the system (usually referred as *corona*). The hard emission is modelled with a power law with or without cut off at high energies, although thermal comptonisation models are also widely used.

In this work we used a multicolour disc blackbody (DISKBB) to fit the thermal emission from the accretion disc, which was required by the fits, both in the soft and the transitional state. To model the thermal emission from the NS surface we used a single-temperature blackbody (see Lin et al., 2007).

For the hard emission we used the thermally comptonized continuum model NTHCOMP (Życki et al., 1999; Zdziarski et al., 1996), which compared to an exponentially cutoff power law describes more accurately the high energy shape and the low energy rollover, with similar number of parameters. This model allows to select the spectral shape of the source of seed photons between a (quasi)blackbody and a disk blackbody. During the fitting process we used either of the thermal components as source of seed photons for NTHCOMP. Both options gave statistically acceptable fits, however when we linked the emission from the NS surface/boundary layer to NTHCOMP the blackbody emission itself tuned out to be negligible raising an inconsistency in the model. We therefore opted for the disk blackbody as the source of seed photons for NTHCOMP.

Additionally, the emission coming from the inner parts of the accretion disc, close to the NS, may be modified by relativistic effects. For a rotating NS, these effects are similar as for a spinning BH (Miller et al., 1998a) and are approximately described by a Kerr metric characterised by the dimensionless angular momentum, $a_* = cJ/(GM^2)$. For the case of a NS, the metric also depends on the internal structure of the NS, set by the equation of state (EoS), which is unknown. However, the spin parameter for a NS can be approximated as $a_* = 0.47/P[\mathrm{ms}]$ (Braje et al., 2000). For 4U 1636–53, with $\nu = 581$ Hz (Strohmayer & Markwardt, 2002), the spin parameter is $\sim$0.27. This value is consistent with what Miller et al. (1998a) found where, for a 500 Hz rotating NS, a given EoS, and a NS mass of 1.4 $M_\odot$, the spin parameter is $\sim$0.23. Scaling this value up to a rotation of 581 Hz gives $a_* \simeq 0.27$. To test whether the direct disc emission in the spectrum of 4U 1636–53 is significantly affected by relativistic effects we tried, instead of the DISKBB, a multi-temperature blackbody model for a thin, general relativistic accretion disc in a Kerr metric, which also includes self-irradiation (KERRBB; Li et al., 2005). However, using the KERRBB, assuming a distance of 6.5 kpc, a NS mass of 1.4 $M_\odot$, and $a_* = 0.27$, did not significantly improve the fit. Moreover, the uncertainty in the distance and the NS mass of 4U 1636–53, makes the outcome of this model less reliable. Therefore, for the rest of our analysis we only used the DISKBB component to fit the direct disc emission.

To summarise: we fitted both the soft and the transitional state of the source with a multicolour disk blackbody (DISKBB), plus a single-temperature blackbody (BBODY) and the thermally comptonized component (NTHCOMP) with the soft seed photons coming from the accretion disk.

Phenomenological models

After fitting the continuum we found several residuals in the whole PN range, with the most prominent one in the energy range 4–9 keV around the Fe line

emission region. In order to fit these residuals we added a Gaussian emission line with the energy constrained between 6.4 keV and 6.97 keV (Fe K band), while the other parameters of the line (normalisation and width) were free to vary. In all six observations the data were well fitted by this component, however all the lines were very broad, showing widths ranging from ∼1.0 to ∼1.4 keV (see Table 5.8 for more details on the fit parameters). Triggered by this and by previous results on the Fe emission line in 4U 1636–53 (Pandel et al., 2008; Cackett et al., 2010; Ng et al., 2010), we used a set of phenomenological models describing relativistically-broadened lines. We selected three of the most commonly used models by the community: DISKLINE, LAOR, and KYRLINE.

DISKLINE is a relativistic model for a Schwarzschild metric, $a_* = 0$, (Fabian et al., 1989), thought to be suitable for NS with dimensionless angular parameter lower than 0.3 for which the metric should only marginally deviate from Schwarzschild (see Miller et al., 1998a, for details on the subject). Notice that the DISKLINE model does not include light bending corrections.

LAOR is a relativistic line model which includes the effects of a maximally rotating Kerr black hole, $a_* = 0.998$, (Laor, 1991), including light bending corrections. Although this model was meant for black holes, it has been largely used to fit disc lines in NS systems (see Bhattacharyya & Strohmayer, 2007, for comparison between DISKLINE and LAOR in the NS LMXB Serpens X-1).

The KYRLINE component includes all relativistic effects for the Kerr metric (Dovčiak et al., 2004). Differently from the previous two models, the metric changes with the spin parameter, and can be adjusted for any value of a_* between 0 and 0.998. The line profile is calculated for emission from outside the ISCO only, and includes the effects of limb darkening.

Reflection off an ionised disc

When X-rays irradiate an optically thick material such as the accretion disc, they produce a reflection spectrum including fluorescence lines, recombination and other emission (see e.g., Fabian et al., 1989; Ross & Fabian, 1993). When the illuminating flux is high enough (possibly combined with the thermal blackbody radiation intrinsic to the accretion flow) the surface of the accretion disc is expected to be ionised. The ionisation state of the reflecting material determines the shape of the reflection spectrum (e.g., Ross & Fabian, 1993), and thus it is important to solve for the thermal balance of the disc. In most X-ray sources the incident emission for the reflection spectrum is generally a hard power-law spectrum. However, in NS systems, the emission coming from the NS surface/boundary layer may contribute as well. As the shape of the reflection continuum also depends on the incident emis-

sion, it is important to investigate the different possible sources of irradiation. Several ionised reflection models are publicly available within XSPEC, which self-consistently compute the ionisation and thermal balance according to the radiation field. In our analysis we used simultaneously two different reflection models: RFXCONV and BBREFL.

RFXCONV is an updated version of the code in Done & Gierliński (2006), using the Ross & Fabian (2005) reflection `atables`. This model can be used with any input continuum and has therefore the advantage of not having a fixed exponential cut-off in the illuminating power law at 300 keV as in the model of Ross & Fabian (2005). We decided not to reflect the blackbody emission with RFXCONV because this component calculates the ionisation balance assuming that the ionising spectrum is a power law, and this is not appropriate for the case of the reflection of blackbody emission off the disc. Instead, we used BBREFL, which provides the reflection spectrum from a constant density disc illuminated by a blackbody (Ballantyne, 2004). Both components also include lines and edges of the most important elements and ions which are Compton and thermal broadened depending on the ionisation state of the reflecting material.

Since the reflection spectrum may be further smeared by relativistic effects in the inner regions of the accretion disc, we convolved the reflected emission with a Kerr-metric kernel which includes relativistic effects (KERRCONV; Brenneman & Reynolds, 2006), where we fixed the spin parameter to 0.27. In this work we explored how the corona and the boundary layer contributed individually to the reflection spectrum. Details on the specific parameters and their settings are given in Section 5.3.2, and the results are discussed in Section 5.3.4.

Residual absorption and emission features

After fitting the spectra with the continuum model plus the relativistic Fe line profile, the *XMM-Newton* data still showed some narrow residuals. especially at low energies. Besides the commonly seen residuals at the instrumental Si-K and Au-M edges at ∼1.8 keV and ∼2.2 keV, respectively, there were a few other clear features apparent in the residuals. All six observations showed absorption features at ∼0.9 keV, at ∼1.5 keV and at ∼ 9.2 keV. Taking into account the moderate PN energy resolution (∼70 eV at 1 keV), the ∼0.9 keV feature could be due to absorption by Ne IX (0.905 keV) or Fe XVIII (0.873 keV), and may possibly be of astrophysical origin. The energy of the ∼1.5 keV feature is either consistent with the Fe XXI–XXIV blend or with the Al-K edge. The effective area curves of the PN show a strong Al-K edge at ∼1.56 keV, which suggests that this feature is likely an artefact of the PN calibration.

The absorption feature at ∼9.2 keV is consistent with the Fe XXVI edge. The above residuals contributed to an enhanced χ^2. To improve the fit we modelled these residuals with a Gaussian absorption or emission component. Since the main focus of this paper is the spectrum at energies near and above the energy of the Fe line, we do not discuss these lines further. In Obs. 5 we further ignored 11 channels from the PN data (spread between channels 27 and 148), that appeared in the spectrum like very narrow absorption features.

Fitting procedure

We started fitting the energy range 0.8-100 keV using PN (0.8-10 keV), PCA (3-20 keV) and HEXTE (20-100 keV) data. From the fits with the phenomenological model KYRLINE for the line (see Sec. 3.1.1 for details about the model) we noticed a mismatch between PN and PCA data between 4 and 8 keV. To investigate the mismatch we allowed the phenomenological model of the line to vary between PN and PCA, and we found that, except for the normalisation, the parameters of the Fe line were consistent within errors. By letting the line normalisation free between the two instruments the fit improved significantly. The values of the normalisation in PN and PCA were, in both cases, significantly different from zero. We tested the fits excluding both PCA and HEXTE data, and we fitted the model previously described to the PN data only. We found that, for the observations in the transitional state the line parameters do not change much between PN, and PN+PCA+HEXTE, except for the normalisation of the line and the inner radius of the disc that are marginally larger in the case we used the three instruments. All continuum components were statistically required to fit the PN-only spectrum. In the soft spectra all the line parameters were consistent within the errors with being the same. In this case the direct emission from the corona is not statistically required by the fit. This is however understandable given that the PN only extends up to 10 keV and the hard emission is less important in the soft than in the transitional state.

Based on these comparisons, and to be able to properly constrain the underlying continuum and model the Fe line emission, we proceeded further by including all three instruments in our fits, excluding the PCA data below 10 keV, where we relied on the PN data. We further modelled the residual absorption between 9 and 10 keV using an edge with energy free between 9.2 and 9.3 keV, which could be due to Fe XXVI. The optical depth of the edge varied between 0.05 and 0.1. Not adding the edge to the fits does not affect the parameters of the line. The high level of ionisation required to create this feature contrasts with the Fe line energy values found from the fits, suggesting that this absorption edge might be due to a calibration mismatch between PN

and PCA.

5.3.2 Parameters and parameter settings

As we mentioned, we used the DISKBB, BBODY and NTHCOMP components to model the direct emission coming from the accretion disc, boundary layer, and corona, respectively. The parameters for these components are the disc temperature at the inner edge, $kT_{\rm in}$, the temperature of NS surface, $kT_{\rm BB}$, and the Comptonisation photon index, the electron temperature (high energy rollover), and the seed photon temperature (low energy rollover), Γ, $kT_{\rm e}$, and $kT_{\rm dbb}$, respectively. $N_{\rm dbb}$, $N_{\rm BB}$, and $N_{\rm NTH}$ are the normalisation parameters for the DISKBB, BBDOY and NTHCOMP components, respectively. All the direct emission parameters were free to vary (except $kT_{\rm dbb}$ which was set equal to $kT_{\rm in}$ of DISKBB), but were coupled between the different instruments.

Reflection model

The ionised reflection emission is characterised by three parameters: the scaling reflection factor, $\Omega_{\rm refl}$, from RFXCONV ($\Omega_{\rm refl} < 0$ represents only the reflected component), BBREFL normalisation (flux per emitting area), and the ionisation parameter, $\xi = 4\pi F/n_{\rm H}$, with F the total illuminating flux, and $n_{\rm H}$ the hydrogen number density. Under the assumption that the reflection region in the accretion disc has a constant ionisation parameter we coupled the ionisation parameter between RFXCONV and BBREFL.
The relativistic effects, determined by the metric and the disc properties, were included using the KERRCONV component which is parameterised by the spin parameter, a_*, the disc inclination, θ, the disc inner and outer radius, $R_{\rm in}$ and $R_{\rm out}$ (in units of the marginal stable radius, $R_{\rm ms}$), and the disc emissivity index, β. The latter could be different for the inner and outer disc, although we chose to have a disc described by a single emissivity index. $R_{\rm in}$, θ, and β were free to vary, but we fixed $R_{\rm out}$ to its default value (400 $R_{\rm ms}$) and a_* to 0.27 (see Section 5.3.1). Given this spin parameter, using equation (3) in Miller et al. (1998a), the ISCO is at ∼5.12 gravitational radii, $R_{\rm g}$ ($R_{\rm g} = GM/c^2$, this is the first-order approximation valid for spin frequencies below ∼400 Hz). All free parameters in the relativistically smeared reflection model were coupled between the different instruments.

The inclination in RFXCONV is given as a cosine function and we fixed $\cos\theta$ to a value consistent with the inclination angle in KERRCONV obtained from the initial fits of the relativistically smeared reflection model. For all observations this initial value for the inclination was in the range 63–69°, which is quite high but still consistent with the results of Casares et al. (2006). However, for

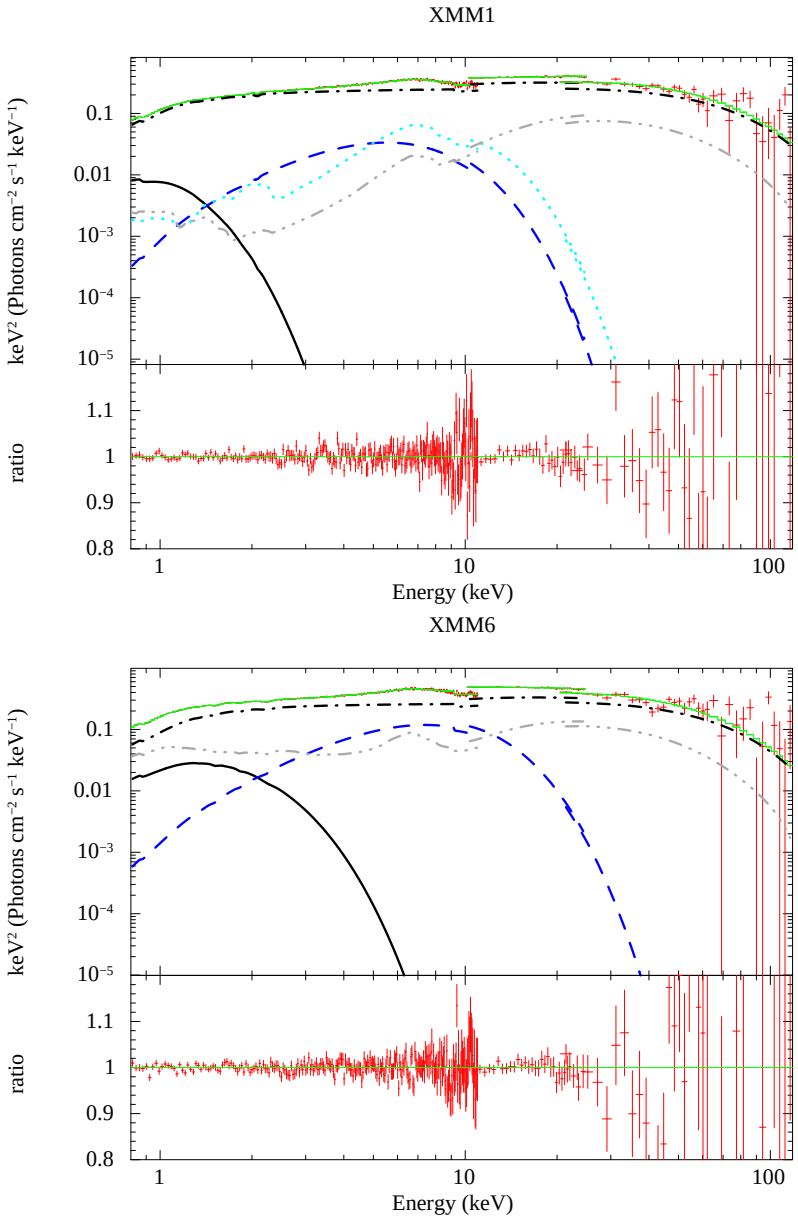

Figure 5.3: The two transitional-state spectra (*top*, Obs. 1, and *bottom*, Obs. 6) of 4U 1636–53. Each plot shows the simultaneously fitted *XMM-Newton/RXTE* spectra and unfolded model in the main panel, and the data/model ratio in the sub panel. To account for the direct emission from the accretion disc, NS surface/boundary layer, and corona, this model contains a DISKBB (black/line), BBODY (blue/dashed), and NTHCOMP (black/dashed-dotted) component, respectively. The relativistically smeared reflected emission is due to two incident components: the NS surface/boundary layer (cyan/dotted) and the corona (light grey/dashed-triple dotted).

most of the observations (except Obs. 2 and 4) we found that the best-fitting values for the inclination inferred from KERRCONV were larger than 80°, which is too high as no eclipses have been seen in this source. In Section 5.4.1 we examine this issue in more detail. Besides the parameters we directly got from the blurred reflection models, it is also common to provide the strength of the Fe line, usually expressed in terms of its equivalent width (EW). However, as the Fe line is part of the reflection spectrum, it is not possible to separate the emission line from the underlying reflection continuum. Therefore, we estimated the equivalent width of the reflection continuum in the region of the Fe line. As the line is broadened, we used the 4–9 keV range as our line region for all six observations. The equivalent width is defined as flux/contin; with flux being the (unabsorbed) 4–9 keV flux of the reflection spectrum, and contin the average (unabsorbed) 4–9 keV flux density of the direct continuum. In Table 5.2 we give the equivalent width obtained in this way. However, we note that these values probably overestimate the true equivalent width of the Fe line since flux not only includes the line photons but also the photons of the underlying reflection continuum.

Phenomenological line models

The phenomenological line models are parameterised by the inclination angle of the accretion disc, i, the rest energy of the line, $E_{\rm line}$, the inner and outer edge of the disc, $R_{\rm in}$ and $R_{\rm out}$, the emissivity index, β (KYRLINE has the option to allow the emissivity index to be different in the inner and outer disc regions; here we chose to have a disc described by a single emissivity index), and the normalisation of the line, $N_{\rm line}$, in photons cm^{-2} s^{-1}. We constrained $E_{\rm line}$ to range between 6.4 and 6.97 keV, and fixed the outer disc radius to be 1000 GM/c^2. Using KYRLINE we fitted the data fixing a_* to three different values: 0, 0.27 and 0.998, and limited the inner radius to the ISCO $R_{\rm in} \gtrsim 6$, 5.12, 1.23 GM/c^2, respectively.

5.3.3 Sources of irradiation

To investigate how the boundary layer and the corona contributed to the reflection spectrum in 4U 1636–53, we defined our model as: PHABS(DISKBB+BBODY+ +NTHCOMP+KERRCONV∗(BBREFL+RFXCONV∗NTHCOMP)) (hereafter, model 1), where both the BBODY and NTHCOMP components were reflected and relativistically smeared. We found acceptable fits for the observations, with the reduced χ^2 ranging from 1.06 to 1.12 for 278 d.o.f. However, for some observations, we found that one of the two reflection components was not contributing significantly to the total spectrum. We therefore investigated the

Table 5.2: Best-fitting results for the reflection model.

Component	Parameter	Obs. 1	Obs. 2	Obs. 3	Obs. 4	Obs. 5	Obs. 6
PHABS	$N_{\rm H}$ (10^{22})	0.40 ± 0.01	0.37 ± 0.03	0.39 ± 0.02	0.31 ± 0.01	0.28 ± 0.02	0.37 ± 0.01
DISKBB	$kT_{\rm in}$ (keV)	0.19 ± 0.01	0.68 ± 0.03	0.72 ± 0.01	0.70 ± 0.03	0.80 ± 0.01	0.40 ± 0.05
	$N_{\rm dbb}$	5026^{+21876}_{-520}	87^{+51}_{-26}	74^{+3}_{-54}	35^{+22}_{-2}	123^{+3}_{-4}	259 ± 78
	$\rm F_d$ (10^{-11})	$3.9^{+17.1}_{-0.9}$	$32.9^{+20.0}_{-11.1}$	$35.1^{+1.5}_{-25.6}$	$15.1^{+9.3}_{-1.4}$	$37.2^{+3.1}_{-2.4}$	$9.5^{+7.2}_{-5.2}$
BBODY	$kT_{\rm BB}$ (keV)	$1.40^{+0.02}_{-0.03}$	1.95 ± 0.02	$1.87^{+0.04}_{-0.01}$	$1.74^{+0.02}_{-0.04}$	$1.37^{+0.02}_{-0.23}$	1.89 ± 0.02
	$N_{\rm BB}$ (10^{-3})	$0.9^{+0.2}_{-0.1}$	5.7 ± 0.4	$2.9^{+1.0}_{-0.4}$	$6.2^{+0.5}_{-0.2}$	$3.0^{+3.1}_{-0.2}$	$3.1^{+0.5}_{-0.6}$
	$\rm F_b$ (10^{-11})	$7.4^{+1.5}_{-0.2}$	48.1 ± 0.8	$24.5^{+8.4}_{-3.4}$	$52.4^{+4.1}_{-1.8}$	$21.3^{+22.0}_{-1.3}$	$26.2^{+4.2}_{-5.1}$
NTHCOMP	Γ	1.94 ± 0.13	$2.42^{+0.20}_{-0.27}$	2.46 ± 0.19	2.90 ± 0.04	$2.00^{+0.76}_{-0.04}$	$1.95^{+0.04}_{-0.14}$
	kT_e (keV)	$17.9^{+3.1}_{-6.1}$	$9.5^{+0.9}_{-0.8}$	$4.5^{+0.3}_{-0.2}$	$16.5^{+35.9}_{-1.9}$	$3.0^{+0.3}_{-0.2}$	$16.4^{+6.7}_{-4.5}$
	$N_{\rm NTH}$	$0.21^{+0.01}_{-0.03}$	$0.12^{+0.08}_{-0.03}$	$0.36^{+0.04}_{-0.08}$	0.31 ± 0.02	$0.15^{+0.11}_{-0.01}$	0.18 ± 0.05
	$\rm F_{NTH}$ (10^{-9})	$1.8^{+0.4}_{-0.7}$	$0.9^{+0.6}_{-0.2}$	$2.4^{+0.3}_{-0.6}$	$1.8^{+0.2}_{-0.1}$	$0.8^{+0.7}_{-0.1}$	$1.8^{+0.5}_{-0.8}$
KERRCONV	β	$2.8^{+0.2}_{-0.1}$	$3.1^{+0.5}_{-0.3}$	$4.1^{+1.2}_{-0.6}$	2.5 ± 0.1	$2.8^{+0.2}_{-0.1}$	$4.5^{+0.0*}_{-2.5}$
	θ (deg)	$83.1^{+0.2}_{-2.7}$	$48.0^{+3.5}_{-2.6}$	$85.5^{+0.6}_{-1.0}$	$70.3^{+0.5}_{-1.9}$	$87.1^{+0.1}_{-1.5}$	$88.7^{+1.1}_{-0.6}$
	$R_{\rm in}$ ($\rm GM/c^2$)	$12.6^{+1.5}_{-1.8}$	$7.8^{+3.1}_{-2.7*}$	15.4 ± 2.7	$5.6^{+2.2}_{-0.3}$	5.4 ± 0.1	$19.1^{+7.6}_{-10.8}$
RFXCONV	$\Omega_{\rm refl}$	$-0.98^{+0.03}_{-0.12}$	$-2.1^{+0.2}_{-1.6}$	$-0.25^{+0.15}_{-0.12}$	-	$-0.92^{+0.1}_{-1.88}$	$-1.29^{+0.2}_{-0.4}$
	$\rm F_{rfx}$ (10^{-10})	$2.1^{+0.8}_{-1.5}$	11.9 ± 9.5	$1.9^{+1.4}_{-1.3}$	-	$0.8^{+0.5}_{-1.7}$	$5.6^{+2.1}_{-3.5}$
BBREFL	disknorm (10^{-24})	1.5 ± 0.1	-	0.013 ± 0.005	$1.72^{+0.03}_{-0.34}$	$5.79^{+0.06}_{-0.08}$	-
	$\log\xi$	$1.00^{+0.02}_{-0.00*}$	$3.75^{+0.0*}_{-0.5}$	$2.87^{+0.16}_{-0.30}$	1.21 ± 0.01	$1.00^{+0.03}_{-0.00*}$	2.49 ± 0.04
	$\rm F_{bbrefl}$ (10^{-10})	1.1 ± 0.1	-	$3.4^{+2.4}_{-2.7}$	$2.6^{+0.1}_{-0.6}$	$4.1.^{+3.9}_{-0.2}$	-
	χ^2_ν (χ^2/ν)	1.12 (313/278)	1.03 (288/279)	1.03 (286/278)	1.08 (301/279)	1.07 (287/268)	1.14 (320/279)
	Total flux (10^{-9})	$1.9^{+0.5}_{-0.8}$	$2.9^{+1.1}_{-0.9}$	$3.0^{+0.5}_{-0.7}$	2.4 ± 0.2	$2.6^{+0.8}_{-0.2}$	$2.7^{+0.5}_{-0.9}$
	EW (keV)	$0.21^{+0.04}_{-0.06}$	$0.63^{+0.47}_{-0.31}$	$0.41^{+0.30}_{-0.28}$	$0.18^{+0.02}_{-0.04}$	$0.36^{+0.29}_{-0.05}$	0.17 ± 0.09

NOTES.– A * denotes that the error has reached the maximum or minimum allowed value of the parameter. Uncertainties are given at a 90% confidence level. $\Omega_{\rm refl} < 0$ represents reflection only, where the actual reflection normalisation is $|\Omega_{\rm refl}|$. $N_{\rm dbb}$ is defined as $(R_{in}/D_{10})^2\cos\theta$, with R_{in} in km, D_{10} the distance in 10 kpc, and θ the inclination angle of the disc. $N_{\rm BB}$ is L_{39}/D^2_{10}, where L_{39} is the luminosity in units of 10^{39} erg $\rm s^{-1}$. $N_{\rm NTH}$ is in units of photons $\rm keV^{-1}$ $\rm cm^{-2}$ $\rm s^{-1}$ at 1 keV. All the flux values reported represent the unabsorbed flux in the energy range 0.5-130 keV, all in erg $\rm cm^{-2}$ $\rm s^{-1}$. EW represents the equivalent width of the reflection component in the 4-9 keV energy range.

scenario where only one of the two incident components, BBODY or NTHCOMP (hereafter model 2 and 3, respectively), contributed to the reflected emission.

In Table 5.3 we summarised the values of χ^2 and number of degrees of freedom for the different fitting models applied. For three out of the 6 observations (Obs. 1, 3 and 5) the best fit was obtained by including both reflection from the NS surface/boundary layer and the corona (model 1). For Obs. 2 and 4, both model 1 and 2 showed the same χ^2 with only 1 d.o.f. of difference. $\Omega_{\rm refl}$, in Obs. 2 and 4, was consistent with being zero, hence RFXCONV∗NTHCOMP in model 1 was not required to model the data. For Obs. 4 we then decided to use model 2. For Obs. 2, on the other hand, we finally opted for model 3. Fitting results from model 2 showed that the direct emission from the NS surface/boundary layer was consistent with zero within errors. According to this, the NS surface/boundary layer was strong enough to generate reflection off the accretion disc, but was not contributing to the direct emission spectrum. This could be due to the presence of a very optically thick medium around the NS surface which completely up-scatters the blackbody-like emission at high enough energy to ionise the accretion disc. If this is the case, the photons escaping from the NS surface might not be distinguishable from a corona-like emission, therefore only the NTHCOMP component would be enough to model the spectrum at those energies. It is more plausible that the model used to fit this spectrum has too many components, resulting in an over-parameterisation of the problem. Taking all this into account, for Obs. 2 we discarded models 1 and 2, although statistically preferred, and we selected model 3 instead. The case of Obs. 6, was very similar to that of Obs. 2 (see 5.3). Also in this case, fitting model 1 we found that only the BBREFL component was significantly contributing to the reflected emission, while switching to model 2 the direct emission from the NS surface/ boundary layer was not significantly required. As for Obs. 2, we decided to use model 3. In Figure 5.3 we show the spectra and the individual components of the best-fit models for the transitional observations fitted with the reflection model. The top and bottom panels of Figure 5.3 show Obs. 1 and 6, respectively. As previously mentioned, in Obs. 1 both the reflection from the NS surface/boundary layer (cyan-dotted line) and corona (light grey dashed-triple dotted line) contribute significantly, with the latter accounting for ∼30% of the reflection emission in the 4.0–9.0 keV range. On the other hand, Obs. 6 does not seem to require reflection contribution from the NS surface.

In Figure 5.4 we show spectra and individual components of the best-fit models for the soft-state observations (*top-left*, Obs. 2, *top-right*, Obs. 3, *bottom-left*, Obs. 4, and *bottom-right*, Obs. 5). Obs. 2 is the only soft-state observation where the reflected spectrum is entirely described by reflection from the corona

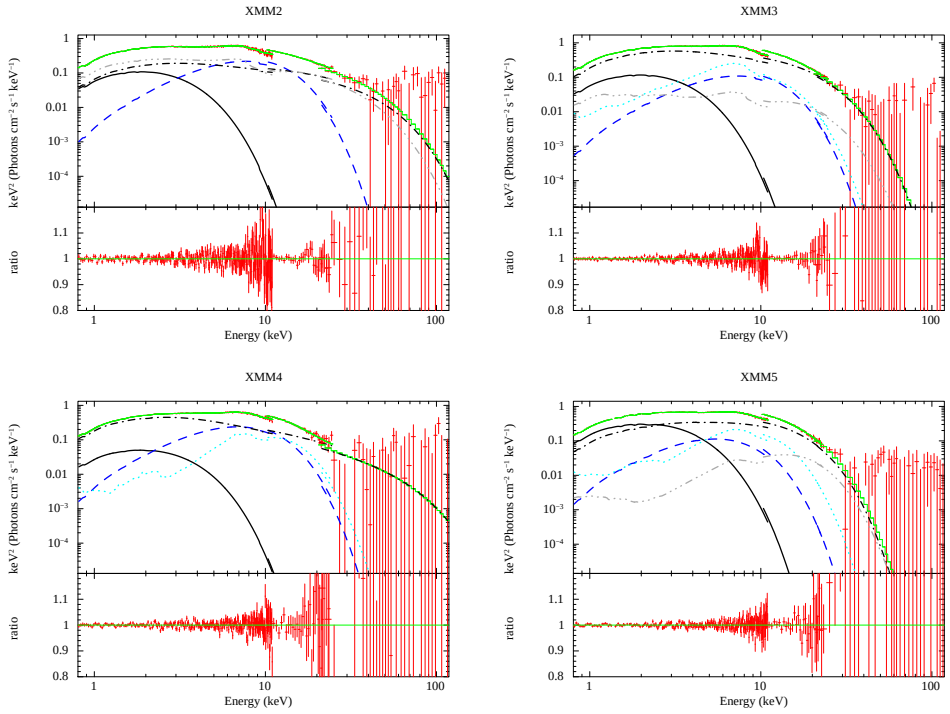

Figure 5.4: The four soft-state spectra (*top-left*, Obs. 2, *bottom-left*, Obs. 4, *top-right*, Obs. 3, and *bottom-right*, Obs. 5) of 4U 1636–53. Each plot shows the simultaneously fitted *XMM-Newton/RXTE* spectra and unfolded model in the main panel, and the data/model ratio in the sub panel. Lines and colours are the same as in Figure 5.3

(light grey dashed-triple dotted line). Obs. 3, as well as Obs. 5, show contribution from both reflection components, with the the corona (light grey dashed-triple dotted line) contributing ∼15% and ∼13%, respectively in the Fe line region. Finally, Obs. 4 is the only soft-state observation where the corona does not contribute to the reflected spectrum.

5.3.4 Evolution of continuum parameters and line

Continuum parameters

The continuum parameters from the reflection and phenomenological models are shown in Table 5.2 and Tables 5.5-5.6, respectively. In order to study the evolution of the individual spectral components in relation to the position of the source in the CD, we ordered the observations according to their colour-

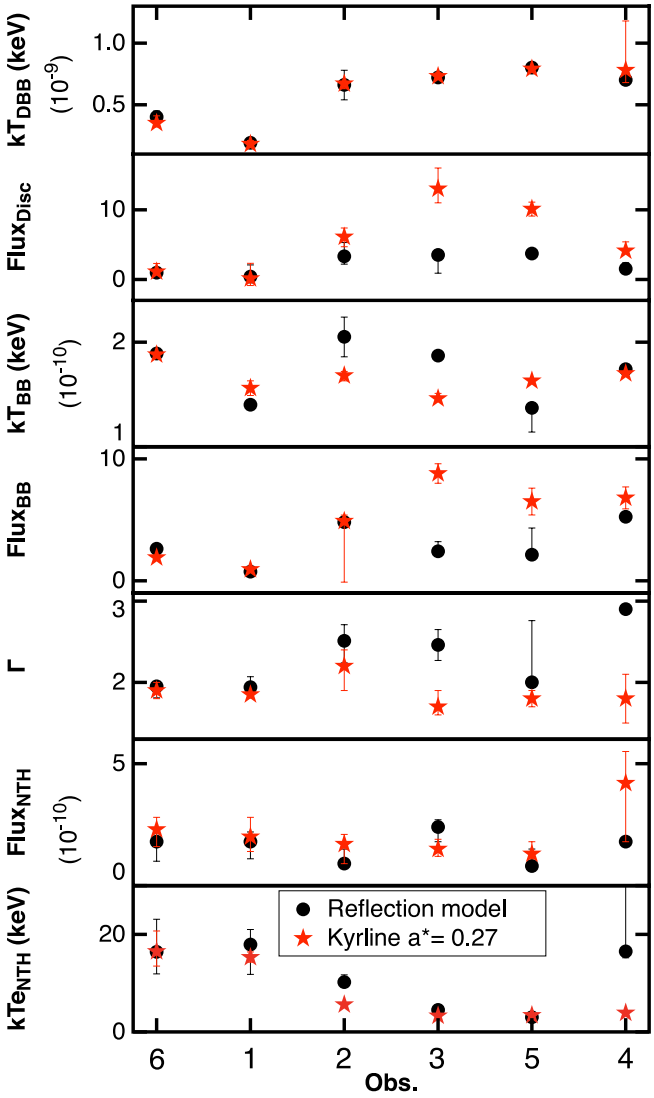

Figure 5.5: Evolution of several spectral parameters as the source moves through the CD. The observations are ordered according to their S_z coordinate. From top to bottom, the panels show respectively the evolution of the DISKBB temperature, the disc flux, the BBODY temperature, the blackbody flux, NTHCOMP photon index, NTHCOMP flux and NTHCOMP electron temperature. The fluxes are unabsorbed in the 0.5–130 keV range in erg cm^{-2} s^{-1}.

colour coordinate S_z, which is thought to be a function of the mass accretion rate (see e.g., Kuulkers et al., 1994). The order of the six *XMM-Newton/RXTE* observations according with their S_z value is: 6–1–2–3–5–4. Applying this order, in Figure 5.5 we show how several of the spectral parameters changed with the position in the CD, considering both the reflection model and a simple relativistic emission model (KYRLINE with angular parameter fixed to 0.27). From the first panel of Figure 5.5 we found that the disc temperature increased as the source became brighter, consistent with the standard accretion disc model (see e.g., Done et al., 2007, and reference therein). The disc flux (second panel) did not show a similar trend as the disc temperature, however it is apparent that the flux is on average lower in the transitional-state (Obs. 1 and 6) than in the soft state; although that is more evident when using the phenomenological model (red stars), it can still be noticed for the reflection model. From panels 3 and 4, we found that the flux and temperature of the NS surface/boundary layer did not show any clear trend with S_z in the fits with the reflection model. Notice, however, that the blackbody flux in the phenomenological model showed a clear increase between the two source states. The BBODY behaviour across the CD does not seem to follow the standard scenario, for which an increase in mass accretion rate should heat up the surface of the NS. Panels 5 to 7 show the corona emission properties across the CD. Both, photon index and flux of the component did not vary systematically as the source moved from transitional to soft state. Notice, however, Γ from the reflection model in average larger in the soft state. On the other hand, the electron temperature (kT_e) of the scattering cloud clearly decreased as mass accretion rate increased (with the exception of Obs.4 in the reflection model). The latter result is consistent with the scenario in which, as the source moves from transitional to soft state, the accretion disc becomes hotter emitting a larger number of soft photons that will cool down the electrons in the corona.

Emission line: phenomenological models

The line parameters from the phenomenological models are given in Table 5.8. In Figure 5.6 we show three representative spectra and individual components of a transitional-state observation (*top*, Obs. 1), and two soft-state observations (*middle*, Obs. 3, and *bottom*, Obs. 4) fitted with relativistic model KYRLINE with $a_* = 0.27$.

The first thing to notice from the table is the fact that the Fe line is very well modelled with a simple, symmetric, gaussian profile. Replacing the gaussian profile with a relativistic line model always lead to an increase of χ^2 (with the exception of Obs. 4), with a maximum $\Delta\chi^2$ between the gaussian and

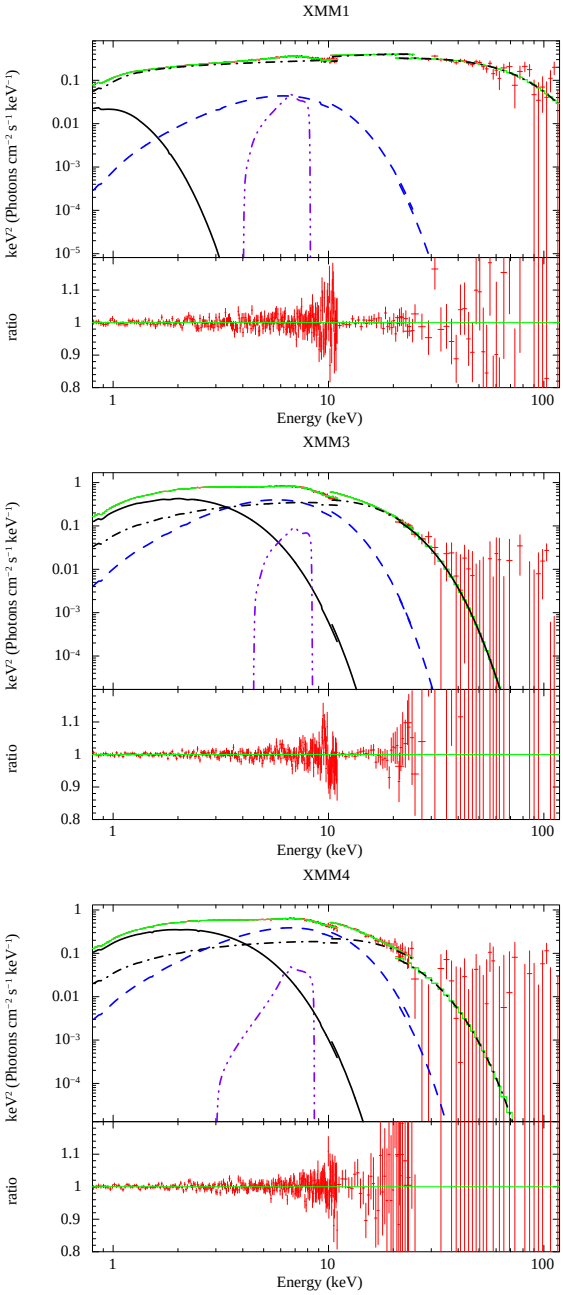

Figure 5.6: Transitional-state spectrum (*top*, Obs. 1) and two soft-state spectra (*middle*, Obs. 3 and *bottom*, Obs. 4) of 4U 1636–53. Each plot shows the simultaneously fitted *XMM-Newton/RXTE* spectra and unfolded model in the main panel, and the data/model ratio in the sub panel. The continuum emission components are represented as in Figure 5.3. The relativistically smeared Fe emission line is fitted with the phenomenological model KYRLINE with spin parameter $a_* = 0.27$ (violet/dashed-triple dotted).

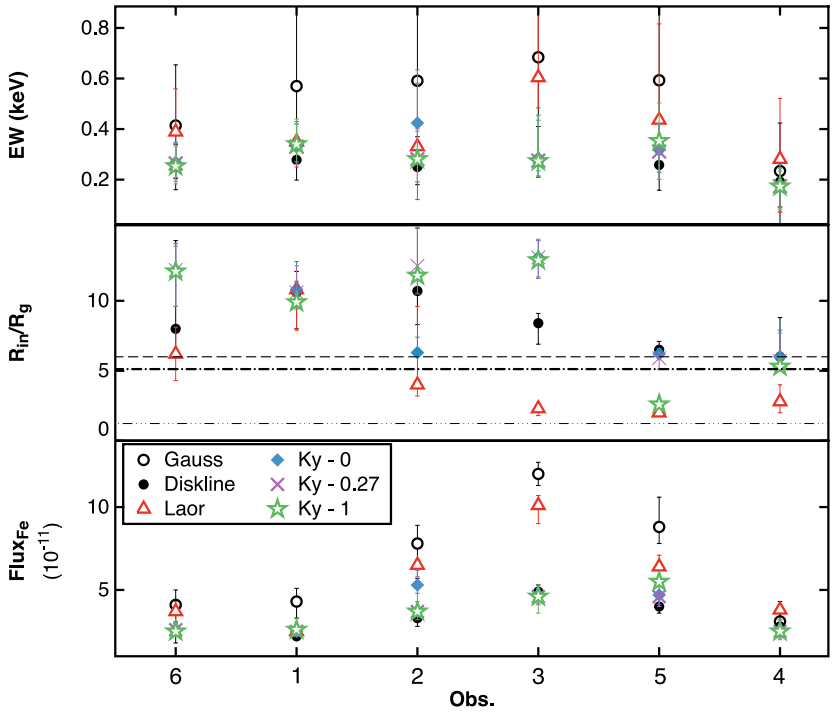

Figure 5.7: Evolution of the Fe emission parameters of different line models as the source moves through the CD. The observations are ordered according to their S_z coordinate. From top to bottom, the panels show respectively the evolution of the equivalent width, the inner radius in units of the gravitational radius, $R_g = GM/c^2$, and the line unabsorbed flux in units of 10^{-11} erg cm^{-2} s^{-1}. Dashed, dashed-dot, and dashed-dot-dot lines (middle panel) represent the 6 R_g, 5.12 R_g, and 1.23 R_g radii, respectively.

the other models of ∼32 (for 2 d.o.f. difference). The gaussian component, however, showed always a very broad profile, with a line width between 1 and 1.4 keV that seemed to increase as the source went from the transitional-state to the soft state, with the exception of Obs. 4 in which the width dropped to its lowest value of 1 keV. In Obs. 1, 2, 5 and 6, all the model consistently showed an energy line at 6.4 keV that implies neutral or lowly ionised iron. In Obs. 3, KYRLINE gave energy values of ∼6.7 keV while the other models place the line at ∼6.4 keV. Finally, in Obs. 4 DISKLINE and KYRLINE gave an energy value of ∼6.4 keV, while GAUSSIAN and LAOR gave values larger than 6.7 keV. The inclination was generally too high given that no dips or eclipses have been observed in 4U 1636–53. All the models showed inclinations larger

than 70 degree, with most of the values showing an upper confidence limit that pegged at 90°. We further found that the emissivity index of the disc was roughly the same for all observations for all the relativistic models.
In Figure 5.7, from top to bottom, we show the evolution of the EW, inner radius and line flux across the CD for the different components used to model the Fe K-α line. GAUSSIAN and LAOR showed the largest EW, although with big errors. Within errors, we found the values of the EW to be consistent between the different models, and not varying with the source state. In the middle panel of Figure 5.7 we show the inner radius in units of the gravitational radius, R_g. In the panel we plot 3 radii representing the ISCO for the Schwarzschild metric (6 R_g), the Kerr metric with $a_* = 0.27$ ($\sim$5.12 R_g) and the Kerr metric with $a_* = 1$ ($\sim$1.23 R_g). Interesting to notice is that only in Obs. 1 all the phenomenological models gave a consistent estimate of the inner radius of $\sim$ 11 R_g, while for the other observations the different models showed significantly different inner radii. Among the models, LAOR showed generally the lowest values of the radius. Although LAOR and KYRLINE with $a_* = 1$ are based on the same Kerr-metric kernel, in 4 out of 6 observations both gave significantly different values of R_{in}. A similar consideration is valid also for DISKLINE and KYRLINE with $a_* = 0$. Overall, the inner radius did not vary much from Obs. 6 to Obs. 3, and than significantly dropped in the last two observations.
Finally, the bottom panel of Figure 5.7 shows the unabsorbed line flux in the 0.5–130 keV energy range. The GAUSSIAN and LAOR components showed the largest flux values in all observations. Furthermore, the flux values of both these line models increased from Obs. 6 to Obs. 3, and then decreased down to flux values comparable to the transitional-state ones. DISKLINE and KYRLINE showed a more clear trend with Sz: the line fluxes increased from the transitional-state to the soft state with the only exception of Obs. 4 where the flux dropped.

Emission line: phenomenological models vs. reflection

We found that the inner radii inferred from the reflection model are consistent with the values from KYRLINE with $a_* = 0.27$. Furthermore, the reflection model gave very large inclination values, generally larger than 80°, consistent with KYRLINE (with the only exception of Obs. 2 in which the reflection model gave an inclination of $\sim$50°). Finally, we noticed that the EW in the 4-9 keV energy range from the reflection model was consistent within errors with the EW from the relativistic model KYRLINE.

Obs.	BBREFL+RFXCONV	BBREFL	RFXCONV
1	313/278	326/279	334/279
2	286/278	286/279	288/279
3	285/278	326/279	298/279
4	301/278	301/279	327/279
5	287/268	302/269	308/269
6	290/278	290/279	320/279

Table 5.3: χ^2 and number of degrees of freedom for 3 different configurations for the incident emission. BBREFL models a reflection spectrum from a disc illuminated by a blackbody. RFXCONV is used to create reflection assuming NTHCOMP as incident spectrum. The third option includes both contributions from BBODY and NTHCOMP direct emissions. In grey we highlighted the best fit models chosen for the analysis. See Section 5.3.2 for more details.

5.4 Discussion

We fitted the X-ray spectra of six simultaneous RXTE and XMM-Newton observations of the NS low-mass X-ray binary 4U 1636–53. For the first time we used a reflection model in which simultaneously both the NS surface/boundary layer and the corona were taken to be the source of irradiation to investigate the relative reflection of each of them. We further modelled the Fe emission line assuming different line profiles, both symmetric (GAUSSIAN) and relativistically-broadened (DISKLINE, LAOR, and KYRLINE).

We found that, both in the transitional state and the soft state, the corona is the most prominent component in the broadband spectrum. The emission from the NS surface/boundary layer is on average contributing an order of magnitude less than the corona to the continuum emission. However, the relative contribution of the NS surface/boundary layer increases going from the transitional to the soft state. In four out of six observations (Obs. 1 in the transitional state, and Obs. 3, 4 and 5 in the soft state) the NS surface/boundary layer is the main source of disc irradiation, accounting for ∼70% and ∼80% of the reflected spectrum in the Fe line region (based on the 4–9 keV unabsorbed flux) in the transitional and soft state, respectively. The NS surface/boundary layer reflection spectrum is even more predominant in Obs. 4, where the corona does not contribute at all to the reflection. For the other two observations (Obs. 2 in the soft state, and Obs. 6 in the transitional state) the reflection spectrum originates entirely from the corona emission. Cackett et al. (2010) analysed Obs. 1–3 using a blurred reflection model where only the NS surface/boundary layer (fitted with a blackbody component) was as-

sumed to illuminate the disc. We found that the line properties inferred from our fits with the reflection model are consistent within errors with Cackett et al. (2010) findings. The only discrepancy between the results is related to the ionisation parameter for Obs. 1, which we find to be ∼1 while Cackett et al. (2010) find an ionisation parameter of ∼2.5. It is not surprising, at least for Obs. 1 and 3, that our results matched Cackett et al. (2010) findings. As mentioned above, in Obs. 1 and 3, the NS surface/boundary layer is the predominant source of disc irradiation in the Fe line region, accounting for 70% and 85% of the reflected spectrum, respectively. On the other hand, it is interesting to mention that although in Obs. 2 we modelled the reflection spectrum assuming the corona as source of irradiation, the line parameters are still consistent with those of Cackett et al. (2010).

We modelled the Fe emission line assuming different line profiles, both symmetric (GAUSSIAN) and relativistically-broadened (DISKLINE, LAOR, and KYRLINE). We found that all the models fit reasonably well the data (see Table 5.8 for all the fitting parameters). The GAUSSIAN profile seemed to fit the line better, which suggests a symmetric profile for the Fe emission line. This result agrees with Ng et al. (2010), that found the lines from Obs. 1–3 to be symmetric, and that the GAUSSIAN and the relativistic profile LAOR could fit equally well the line. Ng et al. (2010) suggested that, contrary to previous claims, the width of the line can be explained by mechanisms other than relativistic effects, such as Compton broadening. Kallman & White (1989) showed that iron lines generated in the accretion disc corona (ADC) are characterised by a symmetric profile due to blending, Compton scattering and rotation. Kallman & White (1989) further estimated that Fe lines generated in the ADC could show EW values up to 100 eV assuming standard parameters. From the fits with the GAUSSIAN model we found EW values between ∼300 and ∼700 eV, which are significantly larger than Kallman & White (1989) estimates. This indicates that Compton scattering alone cannot explain the EW from the GAUSSIAN model. This is also confirmed by the reflection model: We find that excluding the convolution component KERRCONV, the reflection model fails to fit the Fe line in the spectrum. For completeness we should mention that the EWs reported by Ng et al. (2010) are significantly lower (between ∼30 and ∼200 eV) than the ones we report here, and that Ng et al. (2010) raised doubts on the Fe line with the largest EW (Obs. 1) being realistic. The fact that we use a wide bandpass energy spectrum (0.8–120 keV) to constrain the direct emission explains the differences between our results and those of Ng et al. (2010). That said, our results suggest that even though the Fe emission line profile is compatible with being symmetric, the broad profile requires a broadening mechanism other than Compton broadening, and therefore the

relativistically-broadened interpretation is still compatible with the data.

The inner disc radii measured from the relativistic models range between 2 and 13 R_g. We noticed some differences between models based on different space-time metrics. LAOR (for maximally rotating black holes) systematically showed the lowest values of R_{in}, in the range 2 to 6 R_g (with the exception of Obs. 1 where all the models measured R_{in} ∼11 R_g). DISKLINE, based on a Schwarzschild metric, showed R_{in} between 6 and 11 R_g, with one observation pegging to the lowest value. Between the two models, LAOR fits the data statistically better in most of the observations. Notice, however, that for rotating NS with $a_* < 0.3$ the metric is expected not to deviate much from Schwarzschild metric (see Miller et al., 1998a, for more details), which is probably the reason why LAOR under-estimated the inner disc radius. Cackett et al. (2010) fitted the emission line profile on Obs. 1–3 using the DISKLINE model. It is interesting to notice that the measurement for the inner radius and the EW from Cackett et al. (2010) are lower than what we reported here. On the other hand, line energy and emission index are consistent with being the same. The fact that Cackett et al. (2010) did not apply corrections for pileup effects and that only used the XMM-Newton data to fit the Fe line, may be the reasons of these discrepancies with our results.

Finally, we modelled the Fe line profile with KYRLINE that allows to set the spin parameter between 0 (equivalent to a Schwarzschild metric) and 1 (maximally rotating Kerr black hole). We tested three different spin parameter values, $a_* = 0$, 0.27 and 1 (see Section 5.3.1 for details). With these models we measured values of the inner disc radius mostly between 5 and 13 R_g (with the only exception of Obs. 5 where for KYRLINE with a_* =1 we found the radius to be at ∼2.5 R_g). We found consistent measurements of the inner radius for all three spin parameters, with only two exception in Obs. 2 and 5, where one of the models significantly deviated from the other two (see Table 5.8). It is interesting to mention that KYRLINE with a_* =1 and LAOR, that are based on the same Kerr metric showed in general significantly different values for the Fe line parameters (see Svoboda et al., 2009, for a detail comparison between the models). Very similar to that, also for KYRLINE with a_* =0 and DISKLINE we noticed discrepancies in the modelling of the line profile, although less significant.

None of the line parameters from the relativistic models show a clear trend with the source state. However, the inner radius of the disc appears to significantly change for two of the soft-state observations (Obs. 4 and 5), the two with the largest S_z values. The line flux increased going from the transitional-state to the soft-state. The inner radius inferred from the reflection model, which is consistent with R_{in} from KYRLINE with a_* =0.27, did not show any

clear correlation with the source state.

Our findings, both from reflection and phenomenological models, suggest that at least for 4U 1636–53 the Fe emission line does not always trace the inner edge of the accretion disc.

5.4.1 Caveats of the analysis

In all cases, the model we used to fit the six *XMM-Newton/RXTE* observations of 4U 1636–53, including relativistically smeared ionised reflection, described the data well, although there are a few caveats. Firstly, we generally found ionisation parameter values consistent with the presence of moderately ionised Fe ($\log \xi$ between 1.2 and 3), however the line energy values from the phenomenological models were mostly at 6.4 keV consistent with neutral Fe. This has been also observed by Cackett et al. (2010) between the reflection model and DISKLINE. The combination of the thermal emission from the disc and the incident emission are consistent with ionisation parameters we found, raising then doubts on the reliability of the line energy values from the phenomenological models. However, we should keep in mind that with phenomenological models we oversimplify the reflection spectrum between 4-9 keV by only fitting a emission line while in reality the spectrum is a superposition of a continuum plus a line spectrum.

Secondly, from all our fits to 4U 1636–53, we found a high disc inclination, which is at odds with the fact that no eclipses are detected in this source. From previous analyses of the first three observations in our sample, Pandel et al. (2008) and Cackett et al. (2010) also reported similar inclinations, always with an upper confidence limit pegged at 90°. The high inclination in the analysis of Pandel et al. (2008) and Cackett et al. (2010) maybe partly due to pileup effects, as pileup hardens the spectrum and possibly extends the blue wing of the Fe line. Pandel et al. (2008) also suggested that the broad line could be due to line blending of different ionisation stages of Fe. When they fit the Fe line with a multiple line model, they found the inclination to be slightly lower ($> 64°$), although it was still consistent with 90°. Nevertheless, even with a conservative pileup correction, and fitting a model that self-consistently includes line blending effects and Compton broadening (the latter was not included in the model used by Pandel et al., 2008), we still found very high inclination values. Although fits to PN timing mode data of other NS LMXBs have revealed well constrained and much lower inclination angles (see e.g., D'Aì et al., 2009; Iaria et al., 2009), it is possible that the PN timing mode data we have used here are still affected by calibration issues. It would be useful to perform a spectral analysis similar to the one presented in this work, but applying it to data taken in different data modes or with other X-ray

missions.

5.5 Summary

We analysed six *XMM-Newton/RXTE* observations of the NS LMXB 4U 1636–53; in two of the observations the source was in the transitional state, and in the other four the source was in the soft state. We used a relativistically smeared ionised reflection model to study the Fe emission line apparent in all six spectra, which we used to investigate the relative contribution of the corona and the NS surface/boundary layer to the reflection continuum. We found that the NS surface/boundary is the main source of irradiation in the Fe line region in four out six observations, both in the transitional and soft state. In the other two observations (one in the transitional and the other in the soft state), the whole reflected spectrum is due to the corona illuminating the accretion disc.
We also fitted the Fe emission line with a set of phenomenological models including symmetric as well as relativistically-broadened profiles. We found that, although the relativistic line models fitted well the data, the symmetric GAUSSIAN profile gave the best fit in statistical terms. The best-fitting Gaussian line was, however, in all cases very broad. Our results suggested that such a broad line profile is unlikely to be produced by Compton broadening, and that relativistic broadening may still be necessary. We found that relativistic models did not consistently modelled the Fe line; this is especially true for the LAOR model. Values of the inner radius estimated form the reflection models are consistent with the results from KYRLINE with $a_* = 0.27$. However, the reflection model did not help solving the issue of the too high inclination values derived from the Fe line profile.
Finally, we also explored the variation of the direct continuum emission and the properties of the Fe line as a function of the source state. According to the standard accretion disc model, as mass accretion rate increases the disc moves inwards. We found that the continuum emission overall matched consistently with that picture, however the inner disc radius inferred from the Fe line did not show any significant correlation with the source state.

5.6 Acknowledgments

We are grateful to Chris Done for providing the RFXCONV model and for useful comments and discussion regarding the model and the manuscript. AS and MM wish to thank ISSI for their hospitality. TB acknowledges support from ASI-INAF grant I/009/10/0.

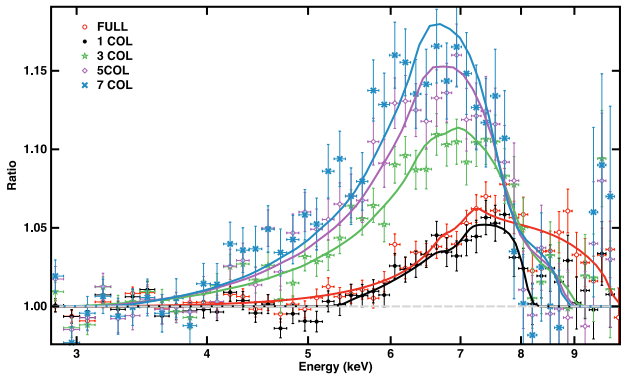

Figure 5.8: Data/model ratios in the 3–9 keV energy range, for different extraction regions used to generate the PN spectra for Obs. 2. Different colour points represent data from different extraction regions, while coloured-solid lines represent the best-fit line profiles. We simultaneously fitted six PN spectra, including also the simultaneous PCA and HEXTE data. We modelled the Fe emission line using the relativistic line model KYRLINE with $a_* = 0.27$. The residuals are represented after setting the line normalisation to 0.

5.7 Appendix: Pileup correction for PN data

As reported by, e.g., Ng et al. (2010), data can suffer from pileup even when the average PN count rate is below the critical pileup level reported by the XMM-Newton User handbook (800 cts s^{-1}). Triggered by that we inspected the dataset for pileup effects. In addition to the spectra created for the full 17-column wide box centred on the source position, we extracted spectra selecting the same events as before but now excising the central, 1, 3, 5 and 7 columns, respectively. We then used the task `epatplot` to determine whether each of these spectra have significant pileup. For Obs. 1 (with a count rate of $\sim$250 cts s^{-1}), we found that excising only the single central column was sufficient to significantly reduce the pileup. For the other five ($>$ 300 cts s^{-1}) observations, we had to excise the 3 central columns to correct for pileup. Unfortunately, the task `epatplot` does not provide a quantitative measure of how pileup affects the spectrum, nor whether the Fe emission line suffers from that. To investigate the effect of pileup on the Fe emission line, we fitted the spectra of all datasets using a phenomenological model for the Fe line (for practical reasons we will only discuss results about Obs. 2, that represents the soft state). We fitted simultaneously all the spectra previously used for the `epatplot` investigation, where we excised 0, 1, 3, 5 and 7 columns. We left the continuum spectral shape parameters (see Section 5.3.1 for details on the

model) free to vary, but we linked them across different spectra. By doing that we forced the continuum emission to maintain the same spectral shape. We only left the normalisation of all the continuum components free to vary in all the spectra. We modelled the Fe emission line with the relativistic model KYRLINE assuming a_*=0.27. The line parameters where free in all spectra. The main assumption here is that if the data are not affected by pileup, the continuum spectral shape will not vary while excising central columns from the PSF. This, in principle, should also apply to the Fe line profile. In Figure 5.8 we show the data/model ratio in the energy range 3–9 keV, after setting the normalisation of the iron line to 0. Different colour represent different excising regions, going from none (black points) to 7 column excised (light-blue points), and solid lines represent the best-fit Fe line profile. From Figure 5.8 we notice that the line profile significantly changes with the number of excised columns. More specifically, we find that the line energy quickly drops from 6.97 to 6.4 keV as the number of columns excised goes from 0 to 3. On the other hand excising 5 and 7 columns still gives line energies around 6.4 keV. The inner radius shows a similar behaviour, as we can notice from the line profile. Figure 5.8 shows that pileup strongly affects the Fe line. From this test, we decided for this specific observation to correct for pileup by excising 5 central columns of the PSF. Summarising, based on the `epatplot` task and this test, we decided to excise 3 central columns for Obs. 1, Obs. 4–6, and we excised 5 columns for Obs. 2 and Obs. 3. Our extraction regions for Obs. 1–3 are more conservative in comparison with the regions used in previous analysis of the same data (see Ng et al., 2010).

Table 5.4: Obs. 1-2 – Phenomenological models parameters: Continuum components

Obs. 1	Model comp	Parameter	Gaussian	Diskline	Laor	Kyrline 0	Kyrline 0.27	Kyrline 1
	phabs	$N_{\rm H}$ (10^{22} cm^{-2})	0.42 ± 0.08	$0.34^{+0.05}_{-0.09}$	$0.41^{+0.11}_{-0.10}$	$0.41^{+0.06}_{-0.11}$	$0.40^{+0.07}_{-0.10}$	$0.47^{+0.05}_{-0.04}$
	diskbb	$kT_{\rm in}$ (keV)	$0.19^{+0.03}_{-0.02}$	0.18 ± 0.06	$0.17^{+0.03}_{-0.01}$	$0.18^{+0.04}_{-0.02}$	$0.18^{+0.03}_{-0.02}$	$0.20^{+0.02}_{-0.01}$
		$N_{\rm dbb}$	16648^{+15985}_{-9988}	11238^{+18530}_{-995}	27086^{+18564}_{-19156}	17387^{+17190}_{-11320}	18114^{+23283}_{-11337}	10498^{+7584}_{-5862}
		$F_{\rm d}$ (10^{-11})	$14.9^{+23.0}_{-11.3}$	$7.4^{+30.2}_{-6.8}$	$12.9^{+21.4}_{-10.1}$	$11.5^{+25.6}_{-10.0}$	$12.0^{+22.0}_{-9.9}$	$12.5^{+12.2}_{-7.6}$
	bbody	$kT_{\rm BB}$ (keV)	$1.30^{+0.15}_{-0.06}$	$1.56^{+0.05}_{-0.06}$	$1.56^{+0.11}_{-0.08}$	1.56 ± 0.07	1.56 ± 0.07	1.56 ± 0.08
		$N_{\rm BB}$ (10^{-3})	0.9 ± 0.2	1.33 ± 0.2	1.1 ± 0.2	1.1 ± 0.2	1.1 ± 0.1	1.1 ± 0.1
		$F_{\rm b}$ (10^{-10})	0.8 ± 0.2	1.2 ± 0.1	0.9 ± 0.2	0.9 ± 0.2	0.9 ± 0.1	0.9 ± 0.2
	nthcomp	Γ	1.85 ± 0.02	1.84 ± 0.06	1.85 ± 0.01	1.85 ± 0.01	1.85 ± 0.01	1.86 ± 0.01
		$kT_{\rm e}$ (keV)	$15.4^{+1.3}_{-1.0}$	$15.2^{+1.1}_{-0.9}$	$15.4^{+1.3}_{-1.1}$	$15.4^{+1.1}_{-0.9}$	$15.3^{+1.1}_{-1.0}$	$15.5^{+1.2}_{-1.0}$
		$N_{\rm NTH}$	$0.198^{+0.008}_{-0.007}$	$0.193^{+0.004}_{-0.008}$	$0.201^{+0.007}_{-0.008}$	$0.199^{+0.004}_{-0.007}$	$0.198^{+0.005}_{-0.002}$	0.200 ± 0.004
		$F_{\rm NTH}$ (10^{-9})	2.1 ± 0.1	$2.0^{+0.3}_{-0.4}$	2.1 ± 0.1	$2.0^{+0.2}_{-0.1}$	$2.0^{+0.8}_{-0.6}$	2.0 ± 0.7
		χ^2_ν (χ^2/ν)	1.08 (306/284)	1.18 (333/282)	1.09 (307/282)	1.11 (312/282)	1.11 (312/282)	1.12 (317/282)
		Total flux (10^{-9})	$2.2^{+0.3}_{-0.2}$	2.2 ± 0.4	$2.2^{+0.2}_{-0.1}$	$2.2^{+0.3}_{-0.1}$	$2.2^{+0.2}_{-0.1}$	2.2 ± 0.1
Obs. 2	Model comp	Parameter	Gaussian	Diskline	Laor	Kyrline 0	Kyrline 0.27	Kyrline 1
	phabs	$N_{\rm H}$ (10^{22} cm^{-2})	0.30 ± 0.05	0.32 ± 0.02	0.31 ± 0.03	0.31 ± 0.03	0.31 ± 0.03	$0.32^{+0.02}_{-0.03}$
	diskbb	$kT_{\rm in}$ (keV)	$0.65^{+0.03}_{-0.08}$	0.67 ± 0.02	0.65 ± 0.04	0.68 ± 0.04	$0.67^{+0.02}_{-0.04}$	$0.67^{+0.05}_{-0.03}$
		$N_{\rm dbb}$	107^{+29}_{-15}	188^{+24}_{-19}	127^{+22}_{-14}	159^{+22}_{-23}	172^{+28}_{-23}	173^{+18}_{-23}
		$F_{\rm d}$ (10^{-11})	$33.3^{+11.5}_{-15.6}$	$66.7^{+12.3}_{-11.7}$	$39.6^{+13.4}_{-10.4}$	$60.1^{+18.6}_{-16.3}$	$61.0^{+12.9}_{-14.0}$	$61.4^{+22.9}_{-13.6}$
	bbody	$kT_{\rm BB}$ (keV)	1.76 ± 0.05	1.64 ± 0.03	1.75 ± 0.05	1.68 ± 0.05	$1.68^{+0.04}_{-0.05}$	$1.68^{+0.04}_{-0.03}$
		$N_{\rm BB}$ (10^{-3})	$3.8^{+0.8}_{-0.5}$	$6.1^{+0.6}_{-0.3}$	$4.4^{+0.1}_{-0.2}$	5.3 ± 0.7	$5.8^{+0.6}_{-0.5}$	$5.8^{+0.6}_{-0.5}$
		$F_{\rm b}$ (10^{-10})	$3.2^{+0.7}_{-0.4}$	$5.1^{+0.5}_{-0.2}$	3.7 ± 0.2	4.5 ± 0.6	4.9 ± 0.5	4.9 ± 0.5
	nthcomp	Γ	2.3 ± 0.1	$2.1^{+0.1}_{-0.2}$	2.3 ± 0.1	2.2 ± 0.2	$2.2^{+0.2}_{-0.3}$	$2.2^{+0.2}_{-0.1}$
		$kT_{\rm e}$ (keV)	$6.1^{+0.8}_{-0.3}$	5.4 ± 0.2	$6.2^{+0.3}_{-0.2}$	$5.6^{+1.4}_{-0.4}$	$5.6^{+0.3}_{-0.5}$	$5.6^{+0.9}_{-0.5}$
		$N_{\rm NTH}$	$0.29^{+0.06}_{-0.02}$	$0.19^{+0.01}_{-0.02}$	$0.27^{+0.06}_{-0.03}$	$0.21^{+0.02}_{-0.06}$	$0.21^{+0.03}_{-0.05}$	$0.21^{+0.04}_{-0.03}$
		$F_{\rm NTH}$ (10^{-9})	$2.1^{+0.4}_{-0.3}$	$1.7^{+0.2}_{-0.5}$	$2.0^{+0.5}_{-0.3}$	$1.7^{+0.3}_{-0.5}$	$1.7^{+0.4}_{-0.8}$	$1.7^{+0.4}_{-0.3}$
		χ^2_ν (χ^2/ν)	1.05 (298/284)	1.07 (304/282)	1.06 (299/282)	1.07 (301/282)	1.07 (303/282)	1.07 (302/282)
		Total flux (10^{-9})	$2.8^{+0.5}_{-0.4}$	$2.8^{+0.2}_{-0.6}$	$2.8^{+0.5}_{-0.3}$	$2.8^{+0.4}_{-0.7}$	$2.8^{+0.4}_{-0.8}$	$2.8^{+0.5}_{-0.3}$

NOTES.– A * means that the error was pegged at the hard limit of the parameter range. All uncertainties are given at 90% confidence level. $N_{\rm dbb}$ is defined as $(R_{in}/D_{10})^2 \cos\theta$, with R_{in} in km, D_{10} the distance in 10 kpc, and θ the inclination angle of the disc. $N_{\rm BB}$ is L_{39}/D^2_{10}, where L_{39} is the luminosity in units of 10^{39} erg s^{-1}. $N_{\rm NTH}$ is in units of photons keV^{-1} cm^{-2} s^{-1} at 1 keV. All fluxes represent the unabsorbed 0.5–130 keV flux in units of erg cm^{-2} s^{-1}.

Table 5.5: Obs. 3-4 – Phenomenological models parameters: Continuum components

Obs. 3	Model comp	Parameter	Gaussian	Diskline	Laor	Kyrline 0	Kyrline 0.27	Kyrline 1
	phabs	$N_{\rm H}$ (10^{22} cm^{-2})	0.30 ± 0.01	$0.36^{+0.04}_{-0.08}$	0.36 ± 0.01	0.36 ± 0.01	0.37 ± 0.09	$0.36^{+0.02}_{-0.03}$
	diskbb	$kT_{\rm in}$ (keV)	$0.79^{+0.02}_{-0.08}$	0.73 ± 0.01	0.71 ± 0.03	$0.73^{+0.03}_{-0.01}$	$0.73^{+0.03}_{-0.01}$	$0.73^{+0.05}_{-0.03}$
		$N_{\rm dbb}$	162^{+70}_{-3}	237^{+3}_{-4}	244 ± 51	245^{+5}_{-3}	253 ± 38	244^{+18}_{-23}
		$F_{\rm d}$ (10^{-9})	$1.2^{+0.5}_{-0.4}$	1.2 ± 0.1	1.1 ± 0.3	$1.2^{+0.2}_{-0.1}$	$1.3^{+0.3}_{-0.2}$	$1.2^{+0.4}_{-0.2}$
	bbody	$kT_{\rm BB}$ (keV)	$1.43^{+0.10}_{-0.43}$	1.48 ± 0.03	1.33 ± 0.07	$1.46^{+0.06}_{-0.03}$	$1.46^{+0.05}_{-0.03}$	$1.46^{+0.04}_{-0.03}$
		$N_{\rm BB}$ (10^{-3})	6.9 ± 0.2	$9.9^{+0.1}_{-0.4}$	$8.2^{+0.5}_{-2.1}$	$9.8^{+0.1}_{-1.0}$	$10.4^{+0.1}_{-0.1}$	$10.3^{+0.6}_{-0.5}$
		$F_{\rm b}$ (10^{-10})	5.8 ± 1.7	$8.3^{+0.1}_{-0.3}$	$6.9^{+0.4}_{-1.8}$	$8.3^{+0.1}_{-0.8}$	8.8 ± 0.8	$8.7^{+0.5}_{-2.6}$
	nthcomp	Γ	$1.85^{+0.05}_{-0.02}$	$1.82^{+0.03}_{-0.02}$	$1.82^{+0.01}_{-0.02}$	$1.80^{+0.10}_{-0.03}$	$1.7^{+0.2}_{-0.1}$	$1.8^{+0.2}_{-0.1}$
		$kT_{\rm e}$ (keV)	3.3 ± 0.1	3.4 ± 0.1	3.2 ± 0.1	3.3 ± 0.1	3.3 ± 0.1	$3.3^{+0.9}_{-0.5}$
		$N_{\rm NTH}$	0.15 ± 0.01	$0.13^{+0.04}_{-0.02}$	$0.15^{+0.03}_{-0.01}$	0.13 ± 0.01	0.11 ± 0.01	$0.11^{+0.04}_{-0.03}$
		$F_{\rm NTH}$ (10^{-9})	1.7 ± 0.2	$1.5^{+0.5}_{-0.2}$	$1.6^{+0.3}_{-0.1}$	$1.5^{+0.2}_{-0.1}$	$1.5^{+0.4}_{-0.3}$	$1.3^{+0.6}_{-0.4}$
		χ^2_ν (χ^2/ν)	1.09 (306/281)	1.19 (333/279)	1.12 (314/279)	1.16 (325/279)	1.17 (326/279)	1.17 (328/279)
		Total flux (10^{-9})	3.4 ± 0.5	$3.5^{+0.5}_{-0.2}$	$3.5^{+0.5}_{-0.4}$	$3.5^{+0.3}_{-0.2}$	$3.5^{+0.5}_{-0.4}$	$3.5^{+0.7}_{-0.5}$
Obs. 4	Model comp	Parameter	Gaussian	Diskline	Laor	Kyrline 0	Kyrline 0.27	Kyrline 1
	phabs	$N_{\rm H}$ (10^{22} cm^{-2})	0.30 ± 0.01	0.30 ± 0.01	0.31 ± 0.02	0.30 ± 0.03	0.30 ± 0.01	0.30 ± 0.01
	diskbb	$kT_{\rm in}$ (keV)	0.76 ± 0.03	0.77 ± 0.02	0.74 ± 0.02	0.78 ± 0.02	$0.78^{+0.04}_{-0.01}$	0.78 ± 0.01
		$N_{\rm dbb}$	149^{+11}_{-13}	142^{+7}_{-4}	136^{+10}_{-13}	150^{+8}_{-4}	153^{+8}_{-6}	151 ± 8
		$F_{\rm d}$ (10^{-10})	$3.4^{+0.8}_{-0.7}$	$3.5^{+0.6}_{-0.5}$	2.7 ± 0.5	$4.0^{+0.6}_{-0.5}$	$4.1^{+1.3}_{-0.3}$	4.0 ± 0.4
	bbody	$kT_{\rm BB}$ (keV)	1.67 ± 0.03	$1.73^{+0.02}_{-0.08}$	1.72 ± 0.04	1.70 ± 0.02	1.70 ± 0.02	1.71 ± 0.02
		$N_{\rm BB}$ (10^{-3})	$8.6^{+1.6}_{-2.6}$	9.3 ± 1.3	7.8 ± 0.9	9.6 ± 1.6	10.1 ± 1.3	$10.1^{+1.3}_{-3.1}$
		$F_{\rm b}$ (10^{-10})	$5.8^{+1.1}_{-1.8}$	6.2 ± 0.9	$5.2^{+0.6}_{-0.7}$	6.4 ± 1.1	6.8 ± 0.9	$6.7^{+0.9}_{-2.1}$
	nthcomp	Γ	$1.9^{+0.3}_{-0.1}$	2.0 ± 0.2	$2.1^{+0.4}_{-0.2}$	$1.9^{+0.4}_{-0.2}$	1.8 ± 0.3	$1.8^{+0.3}_{-0.2}$
		$kT_{\rm e}$ (keV)	$3.8^{+1.3}_{-0.2}$	4.2 ± 0.2	4.1 ± 0.2	4.0 ± 0.2	$3.9^{+0.3}_{-0.1}$	$4.0^{+1.7}_{-0.2}$
		$N_{\rm NTH}$	0.10 ± 0.02	0.09 ± 0.01	$0.14^{+0.03}_{-0.02}$	0.07 ± 0.01	0.06 ± 0.01	0.06 ± 0.02
		$F_{\rm NTH}$ (10^{-10})	$6.1^{+1.9}_{-1.4}$	$5.0^{+0.9}_{-1.3}$	$6.9^{+2.3}_{-1.8}$	$4.3^{+1.4}_{-1.3}$	$4.2^{+1.3}_{-2.4}$	$4.2^{+1.7}_{-1.3}$
		χ^2_ν (χ^2/ν)	1.08 (304/281)	1.06 (297/279)	1.09 (304/279)	1.06 (295/279)	1.06 (296/279)	1.06 (296/279)
		Total flux (10^{-9})	$1.5^{+0.2}_{-0.3}$	$1.5^{+0.1}_{-0.2}$	1.5 ± 0.2	1.5 ± 0.2	$1.5^{+0.2}_{-0.3}$	$1.5^{+0.2}_{-0.3}$

NOTES.– A * means that the error was pegged at the hard limit of the parameter range. All uncertainties are given at 90% confidence level. $N_{\rm dbb}$ is defined as $(R_{in}/D_{10})^2 \cos\theta$, with R_{in} in km, D_{10} the distance in 10 kpc, and θ the inclination angle of the disc. $N_{\rm BB}$ is L_{39}/D_{10}^2, where L_{39} is the luminosity in units of 10^{39} erg s^{-1}. $N_{\rm NTH}$ is in units of photons keV^{-1} cm^{-2} s^{-1} at 1 keV. All fluxes represent the unabsorbed 0.5–130 keV flux in units of erg cm^{-2} s^{-1}.

Table 5.6: Obs. 4-6 – Phenomenological models parameters: Continuum components

Obs. 5	Model comp	Parameter	Gaussian	Diskline	Laor	Kyrline 0	Kyrline 0.27	Kyrline 1
	phabs	$N_{\rm H}$ (10^{22} cm^{-2})	0.28 ± 0.02	$0.30^{+0.01}_{-0.03}$	$0.29^{+0.05}_{-0.01}$	0.29 ± 0.02	0.29 ± 0.01	0.29 ± 0.01
	diskbb	$kT_{\rm in}$ (keV)	0.75 ± 0.04	0.75 ± 0.01	0.73 ± 0.02	0.79 ± 0.02	$0.79^{+0.01}_{-0.02}$	$0.79^{+0.05}_{-0.03}$
		$N_{\rm dbb}$	71^{+19}_{-29}	146^{+7}_{-10}	120^{+14}_{-9}	146^{+11}_{-7}	154^{+10}_{-8}	148^{+11}_{-15}
		$F_{\rm d}$ (10^{-10})	$1.5^{+0.6}_{-0.7}$	3.1 ± 0.3	$6.1^{+1.0}_{-0.8}$	$10.4^{+1.4}_{-1.2}$	10.1 ± 1.0	$10.5^{+3.2}_{-1.9}$
	bbody	$kT_{\rm BB}$ (keV)	1.97 ± 0.13	1.68 ± 0.02	$1.67^{+0.04}_{-0.17}$	1.63 ± 0.03	1.63 ± 0.02	1.64 ± 0.03
		$N_{\rm BB}$ (10^{-3})	$4.9^{+0.6}_{-0.4}$	$6.7^{+1.6}_{-0.2}$	4.4 ± 0.7	7.4 ± 1.1	7.7 ± 1.3	$7.4^{+4.0}_{-0.4}$
		$F_{\rm b}$ (10^{-10})	$3.0^{+0.4}_{-0.3}$	$4.5^{+1.0}_{-0.1}$	3.7 ± 0.6	6.2 ± 0.9	6.5 ± 1.1	$6.2^{+3.3}_{-0.3}$
	nthcomp	Γ	2.4 ± 0.2	2.0 ± 0.1	2.1 ± 0.1	$1.9^{+0.1}_{-0.2}$	1.8 ± 0.1	1.9 ± 0.1
		$kT_{\rm e}$ (keV)	$4.2^{+0.9}_{-0.7}$	$3.6^{+0.1}_{-0.8}$	$3.4^{+0.8}_{-0.1}$	$3.5^{+0.2}_{-0.7}$	3.4 ± 0.1	3.5 ± 0.1
		$N_{\rm NTH}$	$0.29^{+0.11}_{-0.04}$	$0.18^{+0.04}_{-0.02}$	$0.23^{+0.01}_{-0.03}$	0.12 ± 0.01	$0.11^{+0.03}_{-0.01}$	0.12 ± 0.01
		$F_{\rm NTH}$ (10^{-9})	$1.1^{+0.5}_{-0.3}$	1.0 ± 0.2	$1.9^{+0.2}_{-0.3}$	$1.3^{+0.2}_{-0.4}$	$1.3^{+0.5}_{-0.2}$	1.3 ± 0.2
		χ^2_ν (χ^2/ν)	1.12 (304/272)	1.22 (331/270)	1.15 (310/270)	1.17 (317/270)	1.18 (320/270)	1.21 (327/270)
		Total flux (10^{-9})	$3.0^{+0.5}_{-0.3}$	$3.0^{+0.3}_{-0.2}$	$3.0^{+0.2}_{-0.3}$	$3.0^{+0.2}_{-0.5}$	$3.0^{+0.5}_{-0.3}$	$3.0^{+0.5}_{-0.3}$
Obs. 6	Model comp	Parameter	Gaussian	Diskline	Laor	Kyrline 0	Kyrline 0.27	Kyrline 1
	phabs	$N_{\rm H}$ (10^{22} cm^{-2})	0.32 ± 0.05	$0.27^{+0.03}_{-0.09}$	$0.32^{+0.05}_{-0.09}$	$0.31^{+0.03}_{-0.06}$	$0.31^{+0.04}_{-0.08}$	$0.29^{+0.06}_{-0.04}$
	diskbb	$kT_{\rm in}$ (keV)	0.32 ± 0.05	$0.41^{+0.04}_{-0.02}$	$0.33^{+0.06}_{-0.05}$	$0.34^{+0.06}_{-0.03}$	$0.35^{+0.06}_{-0.03}$	0.37 ± 0.05
		$N_{\rm dbb}$	713^{+466}_{-251}	360^{+187}_{-28}	644^{+435}_{-124}	611^{+217}_{-54}	581^{+422}_{-114}	466^{+599}_{-69}
		$F_{\rm d}$ (10^{-10})	$0.9^{+1.1}_{-0.6}$	$1.5^{+1.1}_{-0.4}$	$1.0^{+1.3}_{-0.6}$	$1.1^{+1.2}_{-0.4}$	$1.1^{+1.2}_{-0.2}$	$1.2^{+2.0}_{-0.3}$
	bbody	$kT_{\rm BB}$ (keV)	1.79 ± 0.13	$1.73^{+0.04}_{-0.12}$	1.90 ± 0.11	1.89 ± 0.08	1.88 ± 0.02	1.86 ± 0.08
		$N_{\rm BB}$ (10^{-3})	1.7 ± 0.3	$2.5^{+0.3}_{-0.2}$	1.8 ± 0.2	2.2 ± 0.1	2.2 ± 0.2	2.2 ± 0.2
		$F_{\rm b}$ (10^{-10})	1.4 ± 0.2	$2.1^{+0.3}_{-0.6}$	1.5 ± 0.2	1.9 ± 0.2	1.9 ± 0.2	1.9 ± 0.2
	nthcomp	Γ	1.9 ± 0.1	1.9 ± 0.1	$1.9^{+0.2}_{-0.1}$	1.9 ± 0.1	1.9 ± 0.1	1.9 ± 0.1
		$kT_{\rm e}$ (keV)	$15.7^{+4.2}_{-2.6}$	14.5 ± 1.8	$16.8^{+5.0}_{-2.8}$	$16.8^{+4.2}_{-3.0}$	$16.5^{+4.5}_{-2.7}$	$16.2^{+3.8}_{-2.7}$
		$N_{\rm NTH}$	0.23 ± 0.02	0.19 ± 0.01	0.23 ± 0.02	0.22 ± 0.02	$0.22^{+0.01}_{-0.03}$	0.21 ± 0.01
		$F_{\rm NTH}$ (10^{-9})	$2.3^{+0.5}_{-0.7}$	$2.1^{+0.4}_{-0.6}$	$2.4^{+0.8}_{-0.7}$	$2.3^{+0.5}_{-0.7}$	$2.3^{+0.5}_{-0.7}$	$2.3^{+0.4}_{-0.6}$
		χ^2_ν (χ^2/ν)	0.93 (259/278)	1.06 (291/276)	0.94 (260/276)	0.97 (268/276)	0.97 (268/276)	0.98 (270/276)
		Total flux (10^{-9})	$2.6^{+0.5}_{-0.7}$	$2.6^{+0.4}_{-0.5}$	$2.6^{+0.8}_{-0.7}$	$2.6^{+0.5}_{-0.7}$	$2.6^{+0.5}_{-0.7}$	$2.6^{+0.5}_{-0.6}$

NOTES.– A * means that the error was pegged at the hard limit of the parameter range. All uncertainties are given at 90% confidence level. $N_{\rm dbb}$ is defined as $(R_{in}/D_{10})^2 \cos\theta$, with R_{in} in km, D_{10} the distance in 10 kpc, and θ the inclination angle of the disc. $N_{\rm BB}$ is L_{39}/D_{10}^2, where L_{39} is the luminosity in units of 10^{39} erg s^{-1}. $N_{\rm NTH}$ is in units of photons keV^{-1} cm^{-2} s^{-1} at 1 keV. All fluxes represent the unabsorbed 0.5–130 keV flux in units of erg cm^{-2} s^{-1}.

Table 5.7: Phenomenological model parameters: Fe line

	Model	E_{line} (keV)	σ (keV)	incl (°)	R_{in}/R_g	β	Norm (10^{-3})	Flux (10^{-11})	EW (keV)	χ^2/dof
	GAUSS	$6.40^{+0.07}_{-0.0*}$	$1.27^{+0.10}_{-0.14}$	–	–	–	$4.2^{+0.8}_{-1.0}$	$4.3^{+0.8}_{-1.0}$	$0.57^{+0.36}_{-0.31}$	306/284
	DISKLINE	$6.40^{+0.02}_{-0.0*}$	–	$90.0^{+0.0*}_{-15.9}$	$10.6^{+1.5}_{-2.6}$	-2.7±0.1	2.1±0.2	2.2±0.2	$0.28^{+0.06}_{-0.08}$	333/282
	LAOR	$6.44^{+0.08}_{-0.04*}$	–	$86.3^{+0.1}_{-0.3}$	$10.8^{+0.6}_{-2.9}$	$4.4^{+1.9}_{-0.8}$	$2.5^{+0.4}_{-0.3}$	$2.5^{+0.4}_{-0.3}$	$0.35^{+0.08}_{-0.10}$	307/282
Obs. 1	KY a_*=0	$6.40^{+0.06}_{-0.0*}$	–	$86.1^{+0.7}_{-0.9}$	$10.8^{+2.0}_{-1.3}$	$3.3^{+0.4}_{-0.3}$	2.4±0.3	$2.5^{+0.3}_{-0.5}$	$0.33^{+0.09}_{-0.07}$	312/282
	KY a_*=0.27	$6.40^{+0.06}_{-0.0*}$	–	$85.9^{+0.7}_{-0.9}$	$10.6^{+1.9}_{-1.2}$	$3.3^{+0.2}_{-0.3}$	2.4±0.3	$2.5^{+0.4}_{-0.3}$	$0.33^{+0.09}_{-0.07}$	312/282
	KY a_*=1	$6.40^{+0.06}_{-0.0*}$	–	$85.1^{+0.8}_{-0.9}$	$9.9^{+1.9}_{-1.1}$	$3.1^{+0.3}_{-0.2}$	2.5±0.3	2.6±0.3	$0.34^{+0.10}_{-0.07}$	317/282
	GAUSS	$6.40^{+0.07}_{-0.0*}$	1.3±0.1	–	–	–	$7.6^{+1.1}_{-2.0}$	$7.8^{+1.1}_{-2.1}$	$0.59^{+0.43}_{-0.26}$	298/284
	DISKLINE	$6.40^{+0.07}_{-0.0*}$	–	$72.5^{+17.5*}_{-11.7}$	$10.7^{+4.5}_{-2.4}$	-2.7±0.2	3.2±0.5	3.3±0.5	$0.25^{+0.12}_{-0.07}$	304/282
	LAOR	$6.40^{+0.24}_{-0.0*}$	–	$86.8^{+3.2*}_{-0.4}$	$4.0^{+5.6}_{-0.8}$	$4.0^{+1.4}_{-0.7}$	6.4±0.1	6.5±0.3	$0.33^{+0.25}_{-0.21}$	299/282
Obs. 2	KY a_*=0	$6.40^{+0.2}_{-0.0*}$	–	$88.9^{+1.1*}_{-0.9}$	$6.3^{+1.1}_{-0.3*}$	$3.1^{+0.5}_{-0.4}$	$5.3^{+0.9}_{-0.7}$	$5.3^{+0.9}_{-0.7}$	$0.42^{+0.21}_{-0.11}$	301/282
	KY a_*=0.27	$6.40^{+0.1}_{-0.0*}$	–	$83.9^{+2.1}_{-7.9}$	$12.5^{+2.9}_{-2.0}$	$3.0^{+0.7}_{-0.4}$	$3.6^{+2.0}_{-0.6}$	$3.7^{+2.1}_{-0.5}$	$0.28^{+0.12}_{-0.09}$	303/282
	KY a_*=1	$6.40^{+0.1}_{-0.0*}$	–	$83.0^{+2.1}_{-5.8}$	$11.8^{+3.2}_{-1.7}$	$2.9^{+0.5}_{-0.3}$	$3.6^{+0.6}_{-0.3}$	$3.7^{+0.6}_{-0.3}$	$0.28^{+0.11}_{-0.09}$	302/282
	GAUSS	$6.40^{+0.06}_{-0.0*}$	1.4±0.1	–	–	–	11.7±0.7	12.0±0.7	$0.68^{+0.51}_{-0.42}$	306/281
	DISKLINE	$6.40^{+0.03}_{-0.0*}$	–	$90.0^{+0.0*}_{-15.9}$	$8.4^{+0.7}_{-1.5}$	-2.7±0.8	4.6±0.4	$4.9^{+0.4}_{-0.5}$	$0.27^{+0.14}_{-0.06}$	333/279
	LAOR	$6.40^{+0.05}_{-0.0*}$	–	$87.5^{+2.5*}_{-0.5}$	$2.3^{+0.2}_{-0.5}$	3.5±0.2	$9.6^{+0.5}_{-1.0}$	$10.1^{+0.6}_{-1.1}$	$0.60^{+0.55}_{-0.12}$	314/279
Obs. 3	KY a_*=0	$6.67^{+0.06}_{-0.07}$	–	$86.2^{+0.6}_{-0.8}$	$13.1^{+1.2}_{-1.4}$	$3.6^{+0.5}_{-0.3}$	4.4±0.4	$4.7^{+0.4}_{-0.5}$	$0.29^{+0.15}_{-0.05}$	325/279
	KY a_*=0.27	6.68±0.07	–	$86.1^{+0.7}_{-0.9}$	$13.1^{+1.3}_{-1.5}$	$3.5^{+0.4}_{-0.3}$	4.3±0.4	$4.6^{+0.4}_{-0.5}$	$0.28^{+0.18}_{-0.06}$	326/279
	KY a_*=1	6.70±0.1	–	$85.6^{+2.1}_{-5.8}$	$12.9^{+3.2}_{-1.7}$	$3.4^{+0.5}_{-0.3}$	$4.3^{+0.6}_{-0.3}$	$4.6^{+0.1}_{-1.0}$	$0.27^{+0.18}_{-0.06}$	328/279

NOTES.– A * means that the error was pegged at the hard limit of the parameter range. All uncertainties are given at 90% confidence level. β represents the power law dependence of the disc emissivity. The normalisation of all the models is the line flux in photons cm^{-2} s^{-1}. Line flux represents the unabsorbed 0.5–130 keV flux in units of erg cm^{-2} s^{-1}. Inner radius is in units of gravitational radius $Rg = (GM/c^2)$.

Table 5.8: Phenomenological model parameters: Fe line

	Model	E_{line} (keV)	σ (keV)	incl (°)	R_{in}/R_g	β	Norm (10^{-3})	Flux (10^{-11})	EW (keV)	χ^2/dof
	GAUSS	$6.86^{+0.11*}_{-0.10}$	1.0±0.2	–	–	–	$2.9^{+1.1}_{-0.8}$	$3.1^{+1.2}_{-0.9}$	$0.23^{+0.19}_{-0.21}$	304/281
	DISKLINE	$6.43^{+0.05}_{-0.03*}$	–	$73.4^{-4.6}_{-5.9}$	$6.0^{+2.8}_{-0.0*}$	-2.6±0.1	$2.6^{+1.0}_{-0.4}$	$2.8^{+1.0}_{-0.4}$	0.19±0.10	297/279
	LAOR	$6.72^{+0.15}_{-0.32*}$	–	$88.1^{+1.9*}_{-1.8}$	$2.8^{+1.2}_{-0.8}$	$3.3^{+0.9}_{-0.3}$	3.5±0.1	$3.8^{+0.1}_{-0.2}$	$0.28^{+0.24}_{-0.21}$	304/279
Obs. 4	KY a_*=0	$6.43^{+0.1}_{-0.03*}$	–	$72.3^{+9.2}_{-4.9}$	$6.0^{+1.9}_{-0.0*}$	$2.4^{+0.2}_{-0.1}$	$2.4^{+0.6}_{-0.5}$	2.6±0.6	$0.18^{+0.08}_{-0.09}$	295/279
	KY a_*=0.27	$6.43^{+0.07}_{-0.03*}$	–	$72.1^{+9.2}_{-5.2}$	$5.7^{+2.0}_{-0.6*}$	$2.4^{+0.2}_{-0.1}$	$2.4^{+0.6}_{-0.4}$	$2.5^{+0.7}_{-0.4}$	$0.17^{+0.06}_{-0.10}$	296/279
	KY a_*=1	$6.44^{+0.07}_{-0.04*}$	–	$74.3^{+7.3}_{-5.6}$	$5.3^{+1.4}_{-1.9}$	$2.4^{+0.2}_{-0.1}$	$2.3^{+0.6}_{-0.4}$	$2.5^{+0.6}_{-0.5}$	$0.17^{+0.07}_{-0.09}$	296/279
	GAUSS	$6.41^{+0.09}_{-0.01*}$	1.4±0.1	–	–	–	$8.6^{+1.8}_{-1.0}$	$8.8^{+1.8}_{-1.0}$	$0.59^{+0.29}_{-0.23}$	304/272
	DISKLINE	$6.40^{+0.02}_{-0.0*}$	–	$89.9^{-89.9*}_{-14.5}$	$6.5^{+0.6}_{-0.5*}$	-2.6±0.1	$3.8^{+0.6}_{-0.4}$	$4.0^{+0.5}_{-0.4}$	0.29±0.10	331/270
	LAOR	$6.40^{+0.06}_{-0.0*}$	–	$90.0^{-0.0*}_{-1.7}$	$2.0^{+0.4}_{-0.2}$	3.4±0.1	6.1±0.7	6.4±0.7	$0.44^{+0.38}_{-0.12}$	310/270
Obs. 5	KY a_*=0	$6.40^{+0.04}_{-0.0*}$	–	$87.4^{+0.9}_{-1.0}$	$6.2^{+0.4}_{-0.2*}$	2.8±0.2	4.6±0.5	$4.7^{+0.1}_{-0.5}$	$0.32^{+0.10}_{-0.9}$	317/270
	KY a_*=0.27	$6.40^{+0.04}_{-0.0*}$	–	86.7±1.5	$5.9^{+0.4}_{-0.8*}$	$2.7^{+0.2}_{-0.1}$	$4.5^{+0.6}_{-0.5}$	4.6±0.6	0.31±0.11	320/270
	KY a_*=1	$6.40^{+0.03}_{-0.0*}$	–	$89.0^{+1.0*}_{-1.3}$	2.6±0.1	2.4±0.2	5.4±0.6	5.5±0.2	$0.35^{+0.15}_{-0.12}$	327/270
	GAUSS	$6.40^{+0.05}_{-0.0*}$	1.2±0.1	–	–	–	4.0±1.0	$4.1^{+0.9}_{-1.1}$	$0.41^{+0.24}_{-0.21}$	259/278
	DISKLINE	$6.40^{+0.02}_{-0.0*}$	–	$90.0^{+0.0*}_{-21.5}$	$8.0^{+6.3}_{-2.0*}$	-2.5±0.1	$2.4^{+0.3}_{-0.7}$	$2.5^{+0.3}_{-0.7}$	0.25±0.09	291/276
	LAOR	$6.40^{+0.07}_{-0.0*}$	–	$86.4^{+0.3}_{-0.1}$	6.2±1.9	$3.8^{+1.3}_{-0.5}$	3.7±0.6	3.7±0.6	$0.39^{+0.17}_{-0.12}$	260/276
Obs. 6	KY a_*=0	$6.40^{+0.07}_{-0.0*}$	–	$86.8^{+0.7}_{-0.9}$	$12.2^{+1.9}_{-2.6}$	$3.3^{+0.6}_{-0.4}$	$2.6^{+0.3}_{-0.2}$	$2.6^{+0.4}_{-0.2}$	$0.27^{+0.08}_{-0.06}$	268/276
	KY a_*=0.27	$6.40^{+0.07}_{-0.0*}$	–	$86.5^{+0.7}_{-0.9}$	$12.2^{+1.7}_{-2.6}$	$3.3^{+0.6}_{-0.4}$	2.5±0.3	2.6±0.3	$0.26^{+0.08}_{-0.07}$	268/276
	KY a_*=1	$6.40^{+0.09}_{-0.0*}$	–	$85.8^{+0.9}_{-1.0}$	$12.1^{+2.0}_{-2.1}$	$3.1^{+0.5}_{-0.3}$	2.5±0.3	2.5±0.3	$0.25^{+0.08}_{-0.07}$	270/276

NOTES.– A * means that the error was pegged at the hard limit of the parameter range. All uncertainties are given at 90% confidence level. β represents the power law dependence of the disc emissivity. The normalisation of all the models is the line flux in photons cm^{-2} s^{-1}. Line flux represents the unabsorbed 0.5–130 keV flux in units of erg cm^{-2} s^{-1}. Inner radius is in units of gravitational radius $Rg = (GM/c^2)$.

6 Broad iron emission line and kilohertz quasi-periodic oscillations in the neutron-star system 4U 1636–53

— **Andrea Sanna, Mariano Méndez, Diego Altamirano, Tomaso Belloni, Beike Hiemstra** —

Based on Sanna et al., in preparation

Abstract

Both the broad iron line and the frequency of the kilohertz quasi-periodic oscillations (kHz QPOs) in neutron-star low-mass X-ray binaries can potentially provide independent measures of the inner radius of the accretion disc. We use, for the first time, *XMM-Newton* and simultaneous *RXTE* observations of the LMXB 4U 1636–53 to test this hypothesis. We study the properties of the Fe-Kα emission line as a function of the spectral state of the source and in relation to the frequency of the kHz QPOs. We find that the inner radius of the accretion disc deduced from the frequency of the upper kHz QPO varies as a function of the position of the source in the colour-colour diagram, in accordance with the standard scenario of accretion-disc geometry. On the contrary, the inner disc radius deduced from the profile of the iron line is not correlated with the spectral state of the source. The actual values of the inner radii inferred from kHz QPOs and iron lines, in four observations, do not lead to a consistent value of the neutron star mass, regardless of the model used to fit the iron line. Our results suggest that either the kHz QPO or the iron emission line interpretation does not apply for this system. The simultaneous detection of kHz QPOs and broad iron lines are at odds with models in which the broadening of the iron line is due to the reprocessing of photons in an outflowing wind.

6.1 Introduction

The energy and power density spectra of low-mass X-ray binaries (LMXBs) change with time in a correlated way, generally following changes of the source luminosity, supporting the scenario in which these changes are a function of mass accretion rate in the system (e.g., Wijnands et al., 1997; Méndez et al., 1999; Gierliński & Done, 2002). Evolution of the broad-band energy spectra in low-luminosity systems is thought to reflect changes in the configuration of the accretion-disc flow (see review by Done et al., 2007, and references therein). Gierliński & Done (2002) find a strong correlation in the LMXB 4U 1608–52 between the position of the source in the colour-colour diagram and the truncation radius of the inner accretion disc, which is likely driven by the average mass accretion rate through the disc. At low luminosity, the spectrum is consistent with emission from an accretion disc truncated far from the neutron star; as the luminosity increases the spectrum softens and the inner radius of the accretion disc moves inwards.
In a very similar way, changes of the power density spectra appear to be driven by mass accretion rate. At low luminosity, when the energy spectrum of the source is hard, all timing component in the power spectrum have relatively low characteristic frequencies. These frequencies increase with luminosity, as the energy spectrum softens (see e.g., van der Klis, 1997; Méndez & van der Klis, 1997; Méndez et al., 1999, 2001; Homan et al., 2002; van Straaten et al., 2002, 2003, 2005; Altamirano et al., 2005, 2008a,b; Linares et al., 2005, 2007). The fact that fits to the energy spectra suggest that the accretion disc moves closer to the NS, and that the characteristic frequencies in the power density spectra increase as the luminosity increases, supports the idea of a correlation between those frequencies and the dynamics of matter in the accretion disc. The kilohertz quasi-periodic oscillations (kHz QPOs) are especially interesting because of the close correspondence between their frequencies and the Keplerian frequency at the inner edge of the accretion disc (e.g., Miller et al., 1998b; Stella & Vietri, 1998). On short time-scales (within a day or less), the frequency of the kHz QPOs increases monotonically as the source brightens, and the inferred mass accretion rate increases. However, on longer time-scales this correlation breaks down and the intensity-frequency diagram shows the so-called "parallel tracks" (Méndez et al., 1999).

Broad asymmetric iron lines have been often observed in systems with a compact object spanning a large range of masses, from supermassive black holes in AGNs (see Fabian et al., 2000, for an extensive review) to stellar-mass black holes (e.g., Miller et al., 2002, 2004) and neutron star systems (Di Salvo et al., 2005; Piraino et al., 2007; Pandel et al., 2008; Cackett et al.,

2008; di Salvo et al., 2009; Cackett et al., 2010; Ng et al., 2010). The Fe K-α emission line at 6–7 keV is an important feature of the spectrum that emerges from the accretion disc as a result of reflection of the Comptonized and the NS surface/boundary layer photons off the accretion disc. The mechanism responsible for the broad asymmetric profile of the line is still under discussion. Fabian et al. (1989) proposed that the line is broadened by Doppler and relativistic effects due to motion of the matter in the accretion disc. Di Salvo et al. (2005) and Bhattacharyya & Strohmayer (2007) discovered broad iron lines in the NS LMXBs 4U 1705–44 and Serpens X-1, respectively. Cackett et al. (2008) confirmed Bhattacharyya & Strohmayer (2007) results using independent observations, and also discovered broad, asymmetric, Fe K-α emission lines in the LMXBs 4U 1820–30 and GX 349+2. All these authors interpreted the broadening of the line as due to relativistic effects. Relativistic Fe lines have been observed at least in a dozen NS binary systems in the last decade (Di Salvo et al., 2005; Bhattacharyya & Strohmayer, 2007; Cackett et al., 2008; Pandel et al., 2008; Cackett et al., 2009; Papitto et al., 2009; di Salvo et al., 2009; Reis et al., 2009; Iaria et al., 2009; D'Aì et al., 2009; Cackett et al., 2010; D'Aì et al., 2010; Egron et al., 2011; Cackett et al., 2012). A different interpretation for the broadening of the line has been suggested by Ng et al. (2010) who re-analysed almost all the NS systems showing Fe K-α emission lines. Ng et al. (2010) claim that for most of the lines there is no need to invoke special and general relativity to explain the broad profile, and that a simple Compton broadening mechanism is enough.

If the relativistic interpretation of the broadening mechanism of the Fe line is correct, we can directly test accretion disc models by studying the line properties, as the shape of the asymmetric profile depends on the inner and the outer disc radius. We expect then the iron line to be broader in the soft state – when the inner radius is smaller and the relativistic effects stronger – than in the hard state.

Accretion disc models can also be tested using simultaneous measurements of kHz QPOs and iron lines (Piraino et al., 2000; Cackett et al., 2010). If both the Keplerian interpretation of the kHz QPOs frequency and the broadening mechanism (Doppler/relativistic) of the Fe line are correct, these two observables should provide consistent information about the accretion disc. Furthermore, if the overall spectral changes also reflect changes of the inner edge of the accretion disc, the Fe line should vary in correlation with the frequency of the kHz QPOs (see, e.g., Bhattacharyya & Strohmayer, 2007). Understanding the relation between kHz QPOs, Fe emission line and spectral states goes beyond the accretion disc physics. As discussed by Piraino et al. (2000), Bhattacharyya & Strohmayer (2007), and Cackett et al. (2008),

measurements of the line could also help constraining the mass and radius of the neutron star, parameters needed to determine the neutron star equation of state. With all this in mind, in this paper we investigate the correlation between iron line, kHz QPOs and spectral states in the LMXB 4U 1636–53, with the aim to understand whether the existing interpretations of these phenomena are consistent.

The fact that 4U 1636–53 is well sampled with *XMM-Newton*, and *RXTE* observations, is one of the most prolific sources of kHz QPOs, shows strong iron-Kα lines, and shows regular hard-to-soft-to-hard state transitions on time scales of weeks, makes this source an excellent candidate to study the relation between all these three diagnostics.

6.2 Observations

The NS LMXB 4U 1636–53 has been observed with *XMM-Newton* between 2000 and 2009. The first 2 observations (in 2000 and 2001) were performed in imaging-mode, and suffered from severe pile-up and data loss due to telemetry drop outs; we therefore excluded these two observations from the analysis. In Sanna et al. (2012b) we reanalysed the 2005, 2007 and 2008 observations (Pandel et al., 2008; Cackett et al., 2010) and we analysed for the first time four new observations taken in 2009. The observation taken on March 14th, 2009 had a flaring high-energy background during the full $\sim$40 ks exposure, and we therefore excluded this observation from the analysis (see Sanna et al., 2012b, form more details on the analysis of the *XMM-Newton* observations). In this paper we make use of the results reported there.

Since 1996, 4U 1636–53 was observed $\sim$1300 times with *RXTE*; from March 2005 the source was regularly observed for $\sim$2 ks every other day (except for periods with solar viewing occultation). The first results of this monitoring campaign have been reported by Belloni et al. (2007). We took all the information related to the kHz QPOs used for this paper from Sanna et al. (2012a). Following Sanna et al. (2012b), we refer to the 2005, 2006, 2007, 25th March 2009, 5th September 2009, and 11th September 2009 *XMM-Newton* observations as Obs. 1–6, respectively. We will use the same labelling (Obs. 1, etc.) for the simultaneous *RXTE* observations used to study the X-ray variability. When these names are used in the context of power spectral components, spectral hardness, intensities and colours, we refer to the *RXTE* observations.

6.3 Data analysis

We used data from 1280 *RXTE* observations with the Proportional Counter Array (PCA, Zhang et al., 1993), covering 14 years of data since 1996. We produced light curves and colours using the Standard 2 data as in Altamirano et al. (2008a): we used 16-s time-resolution Standard 2 data to calculate the hard and soft colours, defined as the 9.7–16.0 keV / 6.0–9.7 keV and 3.5–6.0 keV / 2.0–3.5 keV count rate ratio, respectively. We measured the intensity in the 2.0–16.0 keV range. We normalised the colours by the corresponding Crab Nebula colour values (e.g., Kuulkers et al., 1994; van Straaten et al., 2003).

We produced Fourier power density spectra (PDS) using the 2–60 keV data from the ∼125 μs (1/8192 s) time resolution Event mode. We created Leahy-normalised PDS for each 16-s data segment with time bins of 1/8192 s, such that the lowest available frequency is 1/16 Hz, and the Nyquist frequency is 4096 Hz. We fitted the PDS in the 50–4000 Hz range using a combination of one or two Lorentzians to fit the kHz QPOs, a constant for the Poissonian noise, and if needed, an extra Lorentzian to fit the broad-band noise at frequencies between 50 Hz and the frequency range spanned by the kHz QPOs.

6.4 Results

6.4.1 Long term spectral behaviour of 1636–53

In Figure 6.1 we show the colour-colour (top), hard colour vs. intensity (bottom left), and the soft colour vs. intensity (bottom right) diagrams for all the available *RXTE* pointed observations. We use different symbols and colours to mark the source during the *XMM-Newton* observations as estimated by the simultaneous *RXTE* observations (see Section 6.2).

Although 4U 1636–53 is a persistent X-ray source, it shows variations in intensity up to a factor of 10, following a narrow track in the colour-colour and colour-intensity diagrams (Belloni et al., 2007; Altamirano et al., 2008a). Using data from the all-sky monitor (ASM) onboard *RXTE*, Shih et al. (2005) found a long-term modulation with a period of 30–40 days, which corresponds to the regular transition between the hard and soft states (Belloni et al., 2007).

The *XMM-Newton* observations sample different parts of the diagrams shown in Figure 6.1. During Obs. 1 and 6, the intensity was low and the spectrum was hard (see Table 4 and 5 in Sanna et al. 2012b for more details on the spectral properties). Observations 2 to 5 were all done when the source was bright, and the source spectrum was relatively soft. The shape of the colour-colour diagram in the top panel of Figure 6.1 shows that 4U 1636–53 belongs to the so-called Atoll class (Hasinger & van der Klis, 1989). The upper right corner

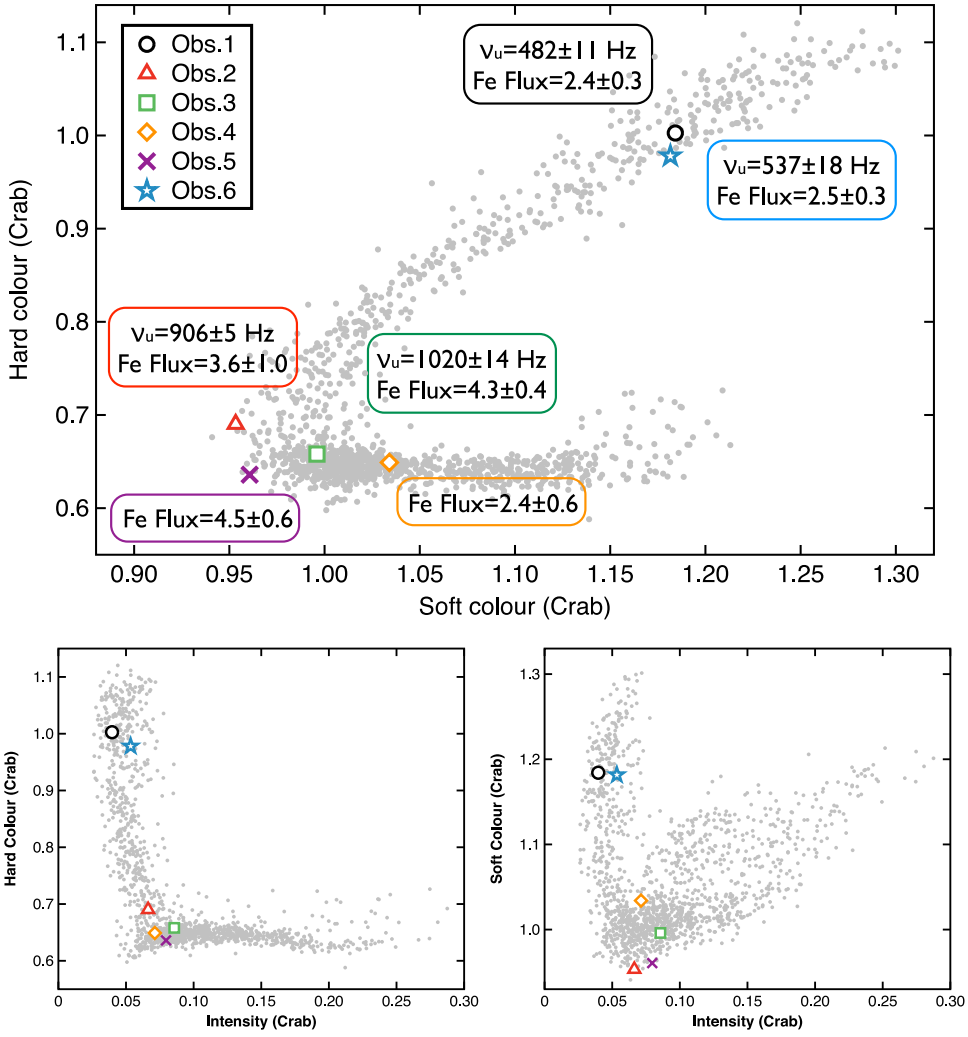

Figure 6.1: Colour-colour, hard colours vs. intensity and soft colours vs. intensity diagrams (upper, lower left and lower right panels, respectively) of 4U 1636–53 for all available *RXTE* pointed observations (grey circles). Colours and intensities during *XMM-Newton* observations computed from pointed *RXTE* observations (see Section 6.2) are marked with different symbols following the legend at the upper-left corner. For each observation we report the frequency of the upper kHz QPO (when detected) and the flux of the line (Fe Flux) in units of 10^{-3} photons cm^{-2} s^{-1} (for fits with a KYRLINE model with $a_* = 0.27$ – see Sanna et al., 2012b, for more details).

Table 6.1: Inner radius inferred from the iron line measurements sorted as a function of the S_z parameter (from Sanna et al. 2012b)

	Obs. 6 $R_{in}(GM/c^2)$	Obs. 1 $R_{in}(GM/c^2)$	Obs. 2 $R_{in}(GM/c^2)$	Obs. 3 $R_{in}(GM/c^2)$	Obs. 5 $R_{in}(GM/c^2)$	Obs. 4 $R_{in}(GM/c^2)$
DISKLINE	$8.0^{+6.3}_{-2.0*}$	$10.6^{+1.5}_{-2.6}$	$10.7^{+4.5}_{-2.4}$	$8.4^{+0.7}_{-1.5}$	$6.5^{+0.6}_{-0.5*}$	$6.0^{+2.8}_{-0.0*}$
LAOR	6.2 ± 1.9	$10.8^{+0.6}_{-2.9}$	$4.0^{+5.6}_{-0.8}$	$2.3^{+0.2}_{-0.5}$	$2.0^{+0.4}_{-0.2}$	$2.8^{+1.2}_{-0.8}$
KYRLINE a_*=0	$12.2^{+1.9}_{-2.6}$	$10.8^{+2.0}_{-1.3}$	$6.3^{+1.1}_{-0.3*}$	$13.1^{+1.2}_{-1.4}$	$6.2^{+0.4}_{-0.2*}$	$6.0^{+1.9}_{-0.0*}$
KYRLINE a_*=0.27	$12.2^{+1.7}_{-2.6}$	$10.6^{+1.9}_{-1.2}$	$12.5^{+2.9}_{-2.0}$	$13.1^{+1.3}_{-1.5}$	$5.9^{+0.4}_{-0.8*}$	$5.7^{+2.0}_{-0.6*}$
KYRLINE a_*=1	$12.1^{+2.0}_{-2.1}$	$9.9^{+1.9}_{-1.1}$	$11.8^{+3.2}_{-1.7}$	$12.9^{+3.2}_{-1.7}$	2.6 ± 0.1	$5.3^{+1.4}_{-1.9}$
REFLECTION	$19.1^{+7.6}_{-10.8}$	$12.6^{+1.5}_{-1.8}$	$7.8^{+3.1}_{-2.7}$	15.4 ± 2.7	5.4 ± 0.1	$5.6^{+2.2}_{-0.3}$

Notes: A * means that the radius pegged at the hard limit of the range.

of the diagram represents times when the source is at low luminosity, in the so-called island state. As the luminosity increases, the source first moves down to the left of the diagram, and then to right along the so-called banana branch (see, e.g., van der Klis, 2006). The *XMM-Newton* observations did not uniformly sample the full range of source colours and intensities, but covered two small regions of the diagram. Obs. 1 and 6 sampled the source in the island state (hard), while Obs. 2–5 covered the soft state, probably the transition from the island state to the banana branch. In order to study the evolution of the iron emission lines and the kHz QPOs in relation to the position of the source in the colour-colour diagram, we sorted the observations according to their colour-colour coordinate S_z, which likely follows the mass accretion rate behaviour (see e.g., Hasinger & van der Klis, 1989; Kuulkers et al., 1994; Méndez et al., 1999). As reported in Sanna et al. (2012b), the order of the six *XMM-Newton/RXTE* observations, going from the hard state to the soft state, according with their S_z values is: 6–1–2–3–5–4.

6.4.2 Iron line and measurements of the inner accretion radius

Sanna et al. (2012b) fitted the iron emission line, using a set of phenomenological line models, and a relativistically-smeared ionised reflection model. In Table 6.1 we report the values of the inner disc radius for the different models used to fit the line. The observations in Table 6.1 are sorted according to their S_z values. As already noted in Sanna et al. (2012b), the inner disc radius inferred from the relativistic profile of the iron line in 4U 1636–53 does not change in correlation with the position in the colour-colour diagram as

predicted in the standard accretion disc model (see e.g., Done et al., 2007, and reference therein). Sanna et al. (2012b) also found that other parameters used to fit the line, such as line energy, source inclination and equivalent width, do not show any clear correlation with the source state (see Figure 6 in Sanna et al., 2012b).

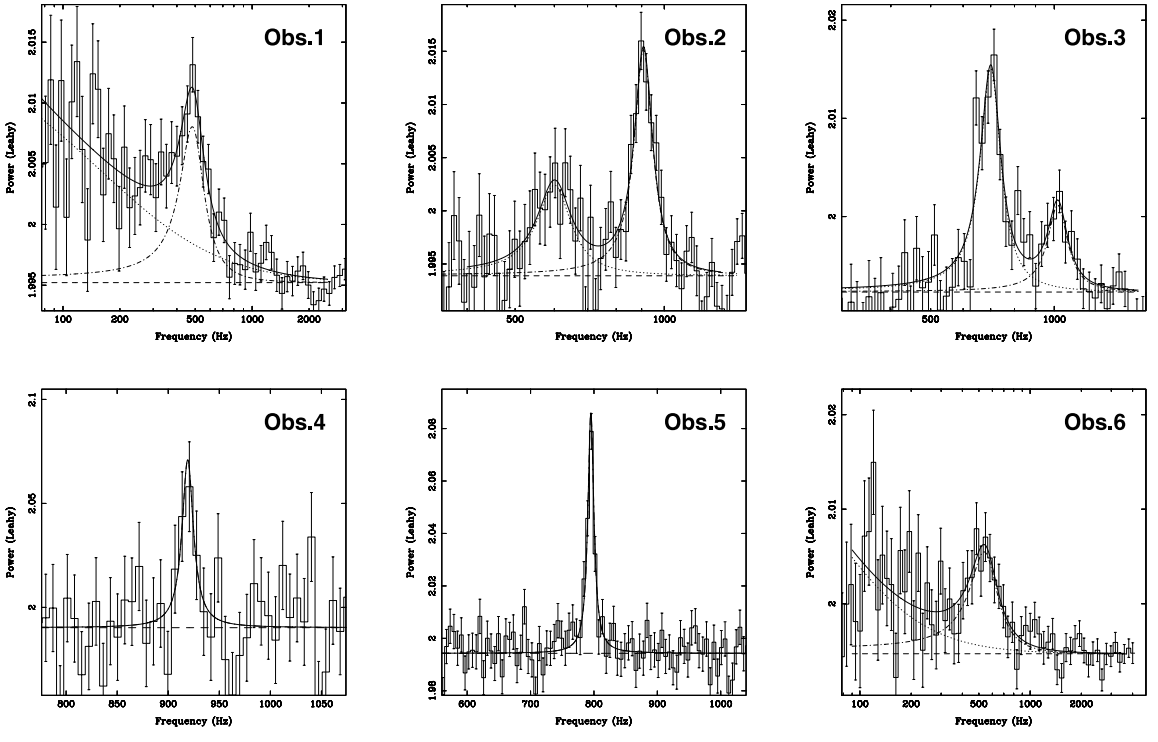

Figure 6.2: Leahy normalised power density spectra for Obs. 1–6 of 4U 1636–53, calculated from the *RXTE* observations. The power density spectra were fitted with a model consisting of a constant, one or two Lorentzians to fit the kHz QPOs, and (if required) a Lorentzian to model the residual broad band noise at low frequencies. The kHz QPO in Obs. 5 is the result of the shift-and-add method (Mendez et al., 1998).

Table 6.2: Parameters of the kHz QPOs in 4U 1636–53 sorted as a function of the S_z parameter

		Obs. 6	Obs. 1	Obs. 2	Obs. 3	Obs. 5	Obs. 4
L_ℓ	ν (Hz)	–	–	597 ± 13	700 ± 5	795.1 ± 0.5	917 ± 3
	FWHM (Hz)	–	–	115^{+42}_{-29}	99 ± 14	11.5 ± 1.3	15 ± 6
	rms (%)	–	–	6.7 ± 0.8	8.5 ± 0.4	11.7 ± 0.3	6.8 ± 0.9
L_u	ν (Hz)	537 ± 18	482 ± 11	906 ± 5	1020 ± 14	–	–
	FWHM (Hz)	247^{+72}_{-58}	178 ± 45	99 ± 13	140^{+48}_{-37}	–	–
	rms (%)	14.1 ± 1.4	11.5 ± 1.5	9.8 ± 0.5	6.3 ± 0.7	–	–

Notes: L_ℓ and L_u stand for the lower and the upper kHz QPO, respectively. For Obs. 5 we report the kHz QPO parameters after applying the shift-and-add method (Mendez et al., 1998).

6.4.3 kHz QPOs and measurements of the inner accretion-disc radius

We detected one or two kHz QPOs in the average PDS of each *RXTE* observation that was performed simultaneously with an *XMM-Newton* observation. In Obs. 1 and 6 we detected a strong broad-band noise component extending up to few hundred Hz plus a single kHz QPO at ∼480 and ∼540 Hz, respectively. The kHz QPOs in Obs. 1 and 6 have rms amplitudes of ∼12% and ∼14%, respectively. The overall power-spectral shape in both cases (not shown) is similar to those previously observed in the hard state of 4U 1636–53 (e.g., intervals A–C in Altamirano et al., 2008a) and other sources (e.g., van Straaten et al., 2002, 2003). In Obs. 4 we detected a single kHz QPO at ∼920 Hz, with an rms amplitude of about 7%. Twin kHz QPOs at ∼600 and ∼905 Hz are present in Obs. 2 with rms amplitudes of ∼7% and ∼10%, respectively, and at around 700 and ∼1020 Hz in Obs. 3, both with rms amplitudes of ∼6%. In Obs. 5 we detected two peaks with a frequency separation significantly lower than the average frequency difference between the lower and the upper kHz QPOs previously reported for this source (Mendez et al., 1998; Jonker et al., 2002; Méndez & Belloni, 2007; Altamirano et al., 2008a). We investigated the evolution of the QPO frequency with time in this observation, and we found that the QPO signal appears sporadically during the long observation, and when it is detectable the frequency changes with time between ∼750 Hz and 880 Hz. It is likely that Obs. 5 showed only one kHz QPO that moved in frequency, we therefore applied the shift-and-add method (Mendez et al., 1998) to recover the properties of the QPO. Notice that we did not find the upper kHz QPO, and that the frequency reported for the kHz QPO in Obs. 5 is the weighed average of the frequencies spanned by the QPO during

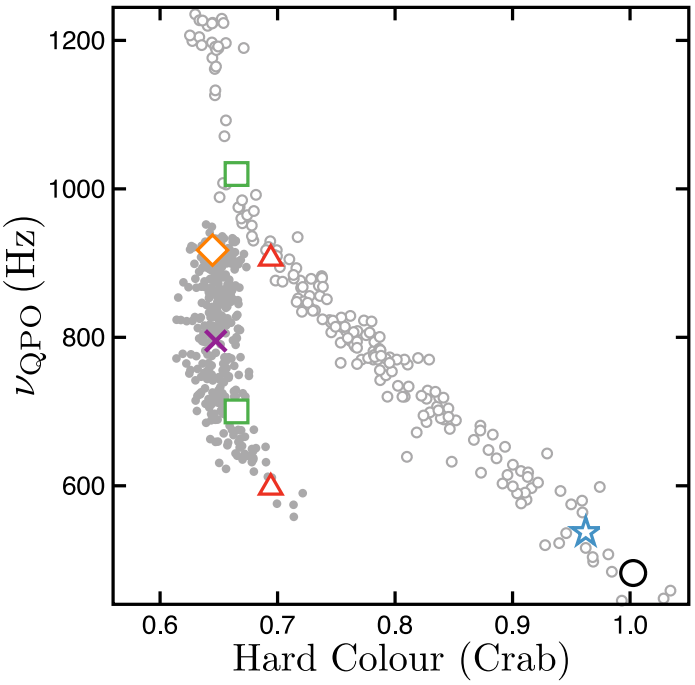

Figure 6.3: Frequency of the kHz QPOs in 4U 1636–53 as a function of hard colours. Grey filled and empty bullets represent the lower and the upper kHz QPOs, respectively (see Sanna et al., 2012a). With large symbols we represent the kHz QPOs detected in Obs. 1–6. The symbols have the same meaning as in Figure 6.1.

the observation. In Figure 6.2 we show the Leahy normalised power density spectra at high frequencies for all six observations, and in Table 6.2 we give the best-fitting parameters of the kHz QPOs. In those observations in which we detected two simultaneous QPOs we can readily identify the lower and the upper kHz QPOs. For the other observations we used the frequency vs. hard colour digram that, as shown in Sanna et al. (2012a) (see also Belloni et al., 2007), can be used to identify the lower and upper kHz QPOs in 4U 1636–53. In Figure 6.3 we show the centroid frequency of the kHz QPOs detected in 4U 1636–53 as a function of hard colour, with different symbols for the lower (grey filled bullets) and the upper (grey empty bullets) kHz QPOs. On top of that we show the kHz QPOs detected in Obs. 1–6. As expected, Figure 6.3 confirms that the two simultaneous QPOs detected in Obs. 2 and 3, are indeed the lower and the upper kHz QPOs. Figure 6.3 also shows that the QPOs detected in Obs. 1 and 6 are both upper kHz QPOs, while the QPOs in Obs. 4 and 5 are both the lower kHz QPOs.

In order to investigate whether the frequency of the detected kHz QPOs re-

mains approximately constant in time, we studied the dynamical power spectra (e.g., Berger et al., 1996) using different frequency and time binning factors. We were unable to follow the time evolution of the upper kHz QPO in any of the observations. We were able to trace the frequency of the lower kHz QPO only in two cases: During Obs. 3 the QPO frequency varied between ∼620 Hz and ∼810 Hz while, as already mentioned, during Obs. 5 the QPO moved between ∼750 Hz and ∼880 Hz.

In accordance with the scenario of an accretion disc truncated at large radii in the hard state, and a disc extending very close to the NS surface in the soft state (Gierliński & Done, 2002; Done et al., 2007), the frequency of the upper kHz QPO is smaller (larger inner radius) in Obs. 6 and 1 (hard state) than in Obs. 2 and 3 (soft state).

6.4.4 Iron lines and kHz QPOs as tracers of the inner radius of the accretion disc

Both kHz QPOs and relativistically-broadened iron lines seem to reflect properties of the accretion matter in the inner edge of the accretion disc (e.g., Fabian et al., 1989; Miller et al., 1998b). To investigate whether the two interpretations match, we compared the inner radius estimated from the frequency of the kHz QPO and the profile of the iron line when both were detected simultaneously. Most models predict that the upper kHz QPO frequency in LMXBs represents the orbital frequency at the inner edge of the accretion disc (e.g., Miller et al., 1998b; Stella & Vietri, 1998). The expression for the orbital frequency in the space time outside a slowly and uniformly rotating NS is $\nu_\phi = \nu_k(1 + a_*(r_g/r)^{3/2})^{-1}$ where $\nu_k = (1/2\pi)\sqrt{GM/r^3}$ is the Keplerian frequency, $a_* = Jc/GM^2$ is the angular momentum parameter, $r_g = GM/c^2$ is the gravitational radius, G is the gravitational constant, M the mass of the NS star, r the radial distance from the center of the NS star, and c is the speed of light. In order to estimate the inner radius we need both the angular momentum parameter and the NS mass. As reported in Sanna et al. (2012b), taking into account the spin frequency of 581 Hz of the NS in 4U 1636–53 (Zhang et al., 1997; Giles et al., 2002; Strohmayer & Markwardt, 2002), we estimated a_* to be 0.27. On the other hand, the mass of the NS in this system is unknown, therefore we calculated the accretion disc radius as a function of the NS mass. The lack of information on the NS mass does not allow us to directly compare R_{in} inferred from the kHz QPO and the iron line simultaneously, however we can compare the trend of R_{in} as a function of other properties of the source, e.g., position in the colour-colour diagram or intensity, and test whether there is a single value of the mass of the NS for which different estimates of the inner disc radius agree.

Figure 6.4

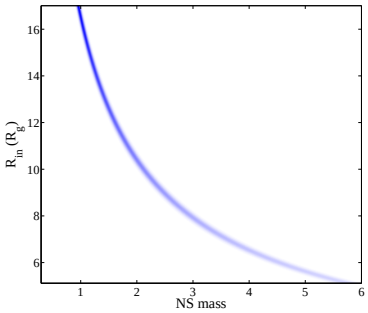

(a) Probability distribution function of the inner radius of the accretion disc as a function NS mass in 4U 1636–53, inferred from the upper kHz QPO in Obs. 1. Colours represent the confidence level.

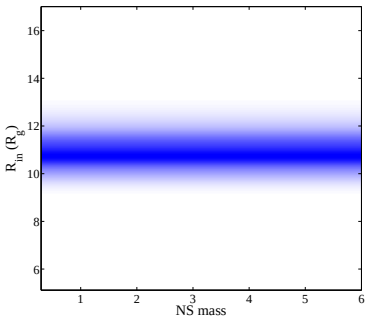

(b) Probability distribution function of the inner radius of the accretion disc as a function of NS mass in 4U 1636–53, inferred from the fit of the iron emission line in Obs. 1 using the relativistic line model KYRLINE with $a_* = 0.27$. Colours represent the confidence level.

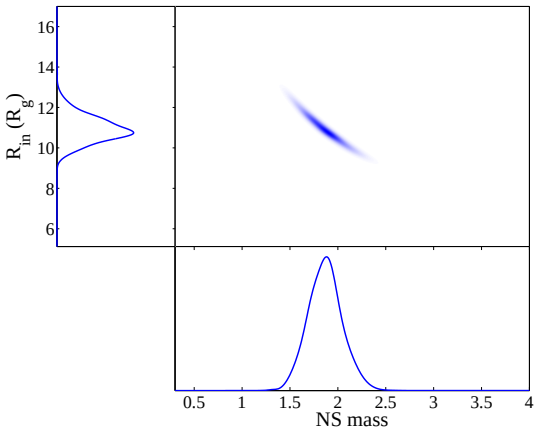

(c) Joint probability distribution function (top-right panel), marginal probability distribution functions for the inner disc radius (top-left panel) and the NS mass (bottom panel) for 4U 1636–53, calculated combining the probability density distribution functions from Figures 6.4a and 6.4b.

To explain in more details how we compared the simultaneous timing and spectral information, in Figure 6.4 we show a step-by-step example for the representative case of Obs. 1. As reported in Table 6.2, Obs. 1 showed an upper kHz QPO at a frequency of ∼480 Hz. In Figure 6.4a we show the accretion disc radius in units of R_g versus the NS mass inferred from the relation between ν_ϕ, M and R_{in}. Colours represent the probability density distribution (PDF) of the inner radius taking into account the uncertainties from the fit of the QPO frequency. In Figure 6.4b we show the inner radius in units of R_g inferred from the modelling of the iron emission line with the relativistic line model KYRLINE with $a_* = 0.27$ (Sanna et al., 2012b). Similar to Figure 6.4a, the PDF of the inner radius is shown in colours. Note that the radius derived from the iron line does not depend upon the NS mass; however, for practical purposes, we plotted the PDF of the inner radius using a similar layout as for the kHz QPO. In Figure 6.4c (central panel) we show the joint probability distribution function of the inner radius and the NS mass derived from the iron line profile and the frequency of the kHz QPO. In Figure 6.4c we also show the marginal distribution for the NS mass and the inner disc radius in units of R_g, calculated by integrating the joint PDF over the radius and the mass, respectively. From this example, we find that the estimates from the kHz QPO frequency and the iron line modelling are consistent for a NS mass of ∼1.9 $M_\odot$ in 4U 1636–53 and an accretion disc extending down to ∼11 R_g; the NS mass is slightly high, but still consistent with most NS equations of state (see, e.g., Lattimer & Prakash, 2007). The fact that the NS mass estimate is consistent with theoretical expectations suggests that, for this particular case, the kHz QPO and iron line interpretations both hold. Since we have observations mapping different position in the colour-colour diagram, we can test whether the kHz QPOs, iron line and accretion properties of the source give a consistent value of the NS mass. To do that we used the four observations, two in the hard state (Obs. 1 and 6) and two in the soft state (Obs. 2 and 3), where we detected both the upper kHz QPOs and the broad iron line simultaneously. Furthermore, we used the inner radius estimated from fits of the iron line profile with different line models (see Table 6.1 for the list of models; see Sanna et al., 2012b, for more discussion on the topic).

In Figure 6.5 we show, for different line models, the marginal probability distribution functions of the NS mass for the four observations with both the upper kHz QPOs and the iron emission line. We notice that the mass values derived from different observations do not yield consistent results, regardless of the iron line model. We further notice that the NS mass values in 4U 1636–53 span a range between ∼0.5 $M_\odot$ and ∼3.0 $M_\odot$, with the exception of the mass inferred from the fits of the line with the LAOR model, which spans a

wider range (1.2–10 $M_\odot$).

6.5 Discussion

We detected kHz QPOs in all the *RXTE* observations simultaneous with the six *XMM-Newton* observations of the NS LMXB 4U 1636–53 for which Sanna et al. (2012b) studied the broad iron line in the X-ray spectrum. Combing the measurements of the frequency of the kHz QPOs and the parameters of the iron lines in 4U 1636–53 we investigated, for the first time, the hypothesis that both the iron line and the kHz QPOs originate at (or very close to) the inner radius of the accretion disc in this system. From these observations we found that the inner disc radius, deduced from the upper kHz QPO frequency, decreases as the spectrum of the source softens, and the inferred mass accretion rate increases. On the other hand, the inner radius estimated from the modelling of the relativistically-broadened iron line did not show any clear correlation with the source state, except for the line model LAOR for which the inferred inner disc radius consistently decreases going from the hard state to the soft state (see Table 6.1). Combining the disc radius inferred from the frequency of the upper kHz QPO and the iron line profile, we found that the range of masses of the NS in 4U 1636–53 obtained in the four observations are inconsistent with being the same. The latter result implies that either the upper kHz QPO frequency does not reflect the orbital disc frequency, the iron line is not relativistically broadened (or both) or, if both the kHz QPO and iron line interpretations are correct, then the two phenomena are not produced in the same region of the accretion disc.

So far we assumed that the upper kHz QPO is the one which reflects the orbital frequency at the inner edge of the of the accretion disc (e.g., Miller et al., 1998b; Stella & Vietri, 1998). There are, however, alternative models that associate instead the lower kHz QPO to the orbital disc frequency (e.g., Meheut & Tagger, 2009). If this is the case, then the radius profile showed in Figure 6.4a would shift to higher values of R_{in} and therefore, the mass for which R_{in} from kHz QPOs and iron lines would match will also shift to higher values. Since the difference in frequency between upper and lower kHz QPOs is more or less constant across the colour-colour diagram (e.g., Mendez et al., 1998; Jonker et al., 2002), using the lower kHz QPOs would lead to similar results as those shown in Figure 6.5, with NS masses shifted toward higher values.

Under the assumption that the kHz QPOs are generated in the accretion disc, and considering circular orbits in the equatorial plane for Kerr space-time, the only characteristic frequency (other than the orbital frequency) that

matches the observed kHz QPO frequency range is the periastron precession frequency. Although the radial profile differs from the one of the orbital frequency, both frequencies decrease as the disc radius increases. Therefore interpreting the upper kHz QPO as the periastron precession frequency and combining the inner radius estimates with the iron line findings would lead to similar inconsistencies regarding the mass of the NS.

The kHz QPOs may still reflect a Keplerian frequency in the disc other than the vicinity of the inner edge of the disc. This mechanism, for instance, could amplify the Keplerian frequencies of matter orbiting within a narrow ring in the disc to produce the QPO. The process could be similar to the lamp-post model by Matt et al. (1991). Such mechanism, however, must be extremely focused, such that only a narrow range of radii in the disc is picked to produce the QPOs, given that in some cases the QPO is quite coherent (e.g., Barret et al., 2005b). For instance, for a 1.8 solar mass neutron star with a QPO at 800 Hz, if this is the Keplerian frequency in the disc, the putative mechanism should pick a ring of $\sim$600 m to produce a QPO with $Q = 200$. Besides generating the kHz QPOs, this mechanism should also affect other properties of the disc, such as the emissivity index or the ionisation balance, which would in turn affect the properties of the iron emission line.

From the behaviour of the time derivative of the lower kHz QPO, Sanna et al. (2012a) found that the kHz QPOs (both the lower and the upper) in 4U 1636–53 are consistent with the orbital frequency at the sonic radius in the accretion disc. We also notice that the frequency of the upper kHz QPOs monotonically increase across the colour-colour diagram consistently with the accretion disc model. All this lends support to the interpretation of the kHz QPO reflecting the orbital frequency at the inner edge of the accretion disc.

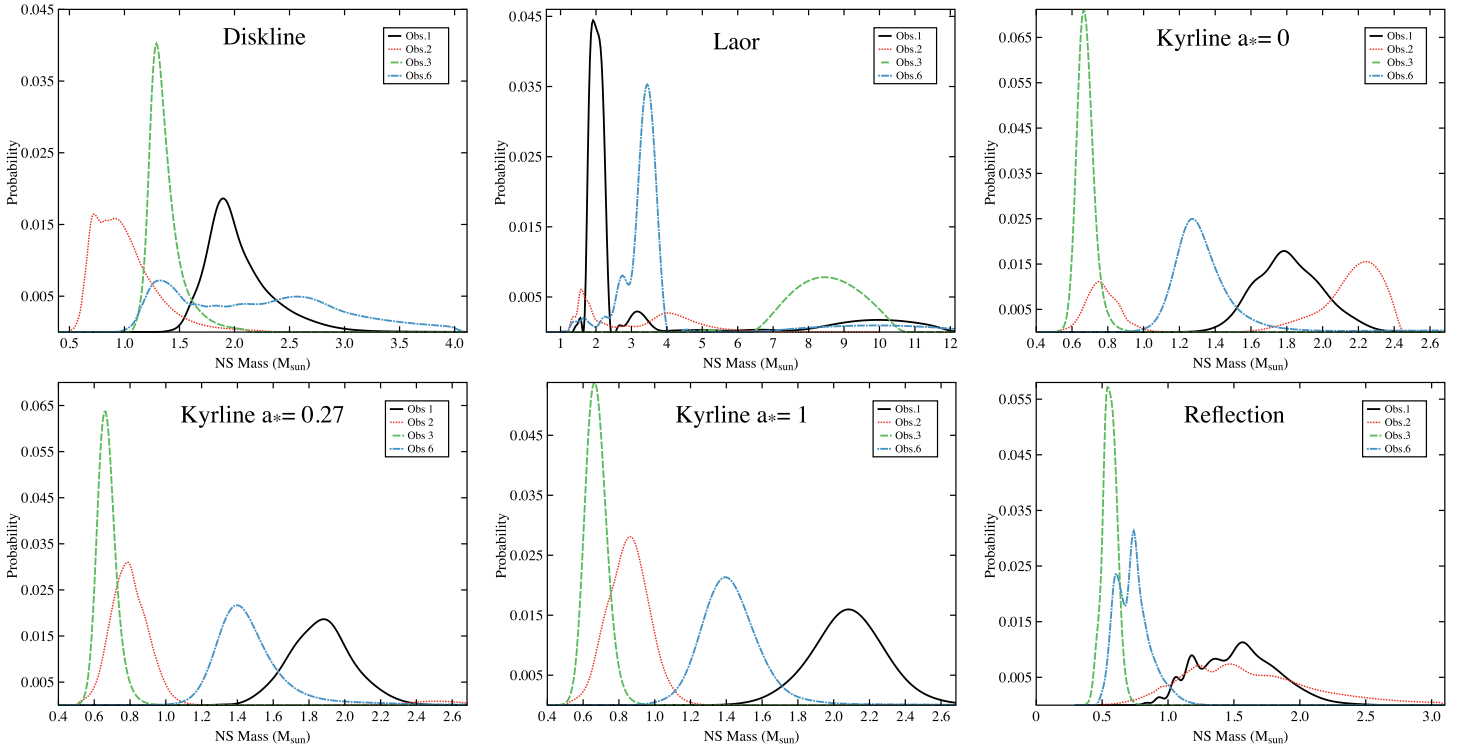

Figure 6.5: Marginal probability distribution functions of the NS mass in 4U 1636–53 inferred from simultaneous measurements of the upper kHz QPO and the iron emission line, for four different observations. Different panels represent different models used to fit the iron line profile.

Besides Doppler and relativistic effects, the iron emission line can be broadened by other processes. For example, the broadening may be (partially or totally) due to Compton scattering in a disc corona (Misra & Kembhavi 1998; Misra & Sutaria 1999; Cackett et al. 2009; see also Reynolds & Wilms 2000; Ruszkowski et al. 2000; Turner et al. 2002, and Ng et al. 2010). However, Sanna et al. (2012b) showed that Compton broadening alone cannot explain the broad profile of the iron emission line in 4U 1636–53. Titarchuk et al. (2003) argued that the red wing of the Fe K-α lines is not due to Doppler/Relativistic effects, but to relativistic, optically-thick, wide-angle (or quasi-spherical) outflows (Laming & Titarchuk 2004; Laurent & Titarchuk 2007, see however Miller et al. 2004; Miller 2007, and Pandel et al. 2008). As explained by Titarchuk et al. (2009), in this scenario the red wing of the iron line is formed in a strong extended wind illuminated by the radiation emanating from the innermost part of the accreting material. One of the main predictions of this model is that all high-frequency variability should be strongly suppressed. The fact that we detected kHz QPOs and broad iron lines simultaneously in 4U 1636–53 casts doubt on this interpretation. Although our findings contradict this scenario, the model under discussion has been developed for black holes, so it is not clear how the boundary layer or the neutron star surface could change these predictions.

Pandel et al. (2008) proposed that the line profile could be the blend of two (or more) lines, for example, formed at different radii in the disc, or due to separate regions with different ionisation balance. If this is correct, the total line profile would be the result of iron lines at different energies. To proceed further with this idea would require to solve the ionisation balance in the accretion disc where the line is formed. Sanna et al. (2012b) investigated this scenario by fitting the reflection spectrum with a self-consistent ionised reflection model, but they did not find any supporting evidence for this idea (see also Cackett et al., 2010). If in 4U 1636–53 the line profile is the result of several lines, then it is intriguing why this source would be different from other systems, like 4U 1820–30, Ser X-1 and GX 349+2, in which the line profile was well modelled with only one DISKLINE component (Bhattacharyya & Strohmayer, 2007; Cackett et al., 2008).

The fact that in Obs. 3 and 5 the kHz QPO frequency significantly varied within the 20-30 ksec required to detect the iron line suggests that the iron line profile we model is likely affected by changes of the disc during those 20-30 ksec. If the kHz QPO frequency depends upon the inner disc radius, the iron line profile we observe would be the average of different line profiles, one for each value of the inner disc radius. This is independent of whether the kHz QPO frequency reflects the orbital disc frequency, or whether the

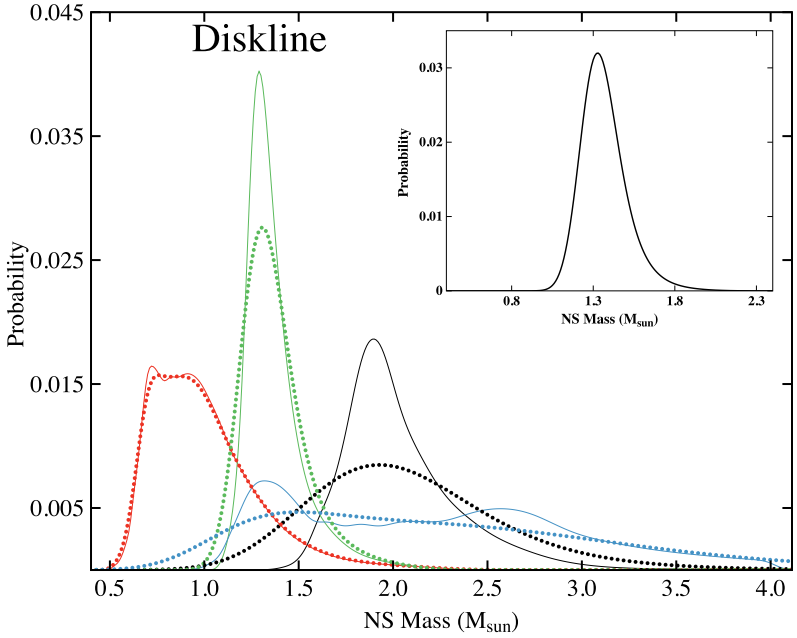

Figure 6.6: Marginal probability distribution functions of the NS mass in 4U 1636–53 using the iron line model DISKLINE. Solid and dotted lines are calculated using the error in the QPO frequency and half the FWHM of the upper kHz QPOs, respectively. The inset shows the joint probability distribution function for the four observations with Fe line and upper kHz QPO, using half the FWHM as the error in the frequency. This is the most likely NS mass range inferred from kHz QPOs and iron lines for these four observations, under the assumption that both the kHz QPO and iron line interpretations are valid.

relation between frequency and inner radius is more complicated. The line energy or the disc emissivity could also vary if the inner disc radius changes. To proceed further, detailed simulations (assuming scenarios in which only the R_{in} changes with time, as well as scenarios in which all line parameters change) are needed to test to what extent changes in the accretion flow on timescales of $\sim$30 ksec (approximately the time needed with present instruments to model the line accurately) can affect the final line profile.

A similar consideration also applies for the inner radius inferred from the kHz QPO frequency. As mentioned in Section 6.4.3, in Obs. 3 and 5 the frequency of the lower kHz QPO spanned a frequency range of $\sim$200 Hz during the $\sim$25 ks observation. Although, we did not directly see the upper kHz QPO changing frequency with time, it is likely that the upper kHz QPO followed the lower one. If this was the case, then the full width at half maximum (FWHM)

of the upper kHz QPO observed contains information on the frequency range covered by the QPO during the observation. To bring this information into the inner disc radius estimates, we should use the QPO FWHM instead of the frequency error (which is relatively small) to calculate R_{in}. In Figure 6.6 we show the marginal probability distribution functions of the NS mass inferred from the four observations combining the upper kHz QPOs and the iron lines modelled with DISKLINE. Solid and dotted lines represent the marginal probability distribution functions using the error in the QPO frequency and half the FWHM as error, respectively. In the latter case the marginal probability distribution functions of the NS mass show a broader profile, and the range of mass values where they are consistent increases (although the overlapping area is still small). By combining the marginal probability distribution functions we get the mass profile (joint probability) for which, in the 4 observations, kHz QPO and iron line estimates of the inner disc radius are consistent. This is shown in the inset of Figure 6.6. The most likely value of the NS mass, for this specific case, ranges between $\sim$1.1 and $\sim$1.5 $M_{\odot}$, which is consistent with theoretical NS mass predictions (e.g., Lattimer & Prakash, 2007). However, it should be noticed that in Figure 6.6, two out of the four PDFs (Obs. 1 and 2) marginally overlap, therefore the final joint probability function is likely not fully representative of all observations. We did not find any improvement in terms of consistency of the mass estimates for any of the other line models.

The frequency of the kHz QPO and the source intensity (likely the mass accretion rate) are degenerate on long time-scales ("parallel tracks" Méndez et al., 1999): The same QPO frequency may appear at very different source intensities. It remains to be seen whether this phenomenon can affect some properties of the disc, such as the emissivity index or the ionisation balance, which would affect the profile of the iron line, and hence the inferred value of the inner radius of the accretion disc.

Bibliography

Abramowicz, M. A., Karas, V., Kluzniak, W., Lee, W. H., & Rebusco, P. 2003, PASJ, 55, 467
Agrawal, P. C. 2006, Advances in Space Research, 38, 2989
Alpar, M. A. & Shaham, J. 1985, Nature, 316, 239
Altamirano, D. & Belloni, T. 2012, ApJ, 747, L4
Altamirano, D., Belloni, T., Linares, M., et al. 2011, ApJ, 742, L17
Altamirano, D., van der Klis, M., Méndez, M., et al. 2008a, ApJ, 685, 436
—. 2005, ApJ, 633, 358
—. 2008b, ApJ, 687, 488
Arnaud, K. A. 1996, in Astronomical Society of the Pacific Conference Series, Vol. 101, Astronomical Data Analysis Software and Systems V, ed. G. H. Jacoby & J. Barnes, 17
Ballantyne, D. R. 2004, MNRAS, 351, 57
Barret, D., Kluźniak, W., Olive, J. F., Paltani, S., & Skinner, G. K. 2005a, MNRAS, 357, 1288
Barret, D., Olive, J. F., Boirin, L., et al. 2000, ApJ, 533, 329
Barret, D., Olive, J.-F., & Miller, M. C. 2005b, MNRAS, 361, 855
—. 2005c, Astronomische Nachrichten, 326, 808
—. 2006, MNRAS, 370, 1140
—. 2007, MNRAS, 376, 1139
Barret, D. & Vaughan, S. 2012, ApJ, 746, 131
Belloni, T., ed. 2010, Lecture Notes in Physics, Berlin Springer Verlag, Vol. 794, The Jet Paradigm
Belloni, T., Homan, J., Motta, S., Ratti, E., & Méndez, M. 2007, MNRAS, 379, 247
Belloni, T., Méndez, M., & Homan, J. 2005, A&A, 437, 209
Belloni, T., Méndez, M., & Sánchez-Fernández, C. 2001, A&A, 372, 551
Belloni, T., Psaltis, D., & van der Klis, M. 2002, ApJ, 572, 392
Belloni, T., Soleri, P., Casella, P., Méndez, M., & Migliari, S. 2006, MNRAS, 369, 305
Belloni, T. M., Sanna, A., & Méndez, M. 2012, MNRAS, 426, 1701

Berger, M., van der Klis, M., van Paradijs, J., et al. 1996, ApJ, 469
Bhattacharyya, S. & Strohmayer, T. E. 2007, ApJ, 664, L103
Boutelier, M., Barret, D., Lin, Y., & Török, G. 2010, MNRAS, 401, 1290
Bradt, H. V., Rothschild, R. E., & Swank, J. H. 1993, A&AS, 97, 355
Braje, T. M., Romani, R. W., & Rauch, K. P. 2000, ApJ, 531, 447
Brenneman, L. W. & Reynolds, C. S. 2006, ApJ, 652, 1028
Cackett, E. M., Altamirano, D., Patruno, A., et al. 2009, ApJ, 694, L21
Cackett, E. M., Miller, J. M., Ballantyne, D. R., et al. 2010, ApJ, 720, 205
Cackett, E. M., Miller, J. M., Bhattacharyya, S., et al. 2008, ApJ, 674, 415
Cackett, E. M., Miller, J. M., Reis, R. C., Fabian, A. C., & Barret, D. 2012, ApJ, 755, 27
Casares, J., Cornelisse, R., Steeghs, D., et al. 2006, MNRAS, 373, 1235
Cui, W., Shrader, C. R., Haswell, C. A., & Hynes, R. I. 2000, ApJ, 535, L123
D'Aì, A., di Salvo, T., Ballantyne, D., et al. 2010, A&A, 516, A36
D'Aì, A., Iaria, R., Di Salvo, T., Matt, G., & Robba, N. R. 2009, ApJ, 693, L1
den Herder, J.-W., den Boggende, A. J., Branduardi-Raymont, G., et al. 2000, in Society of Photo-Optical Instrumentation Engineers (SPIE) Conference Series, Vol. 4012, Society of Photo-Optical Instrumentation Engineers (SPIE) Conference Series, ed. J. E. Truemper & B. Aschenbach, 102–112
di Salvo, T., D'Aí, A., Iaria, R., et al. 2009, MNRAS, 398, 2022
Di Salvo, T., Iaria, R., Méndez, M., et al. 2005, ApJ, 623, L121
Di Salvo, T., Méndez, M., & van der Klis, M. 2003, A&A, 406, 177
Di Salvo, T., Méndez, M., van der Klis, M., Ford, E., & Robba, N. R. 2001, ApJ, 546, 1107
Done, C. & Gierliński, M. 2006, MNRAS, 367, 659
Done, C., Gierliński, M., & Kubota, A. 2007, A&A Rev., 15, 1
Dove, J. B., Wilms, J., & Begelman, M. C. 1997, ApJ, 487, 747
Dovčiak, M., Karas, V., & Yaqoob, T. 2004, ApJS, 153, 205
Egron, E., di Salvo, T., Burderi, L., et al. 2011, A&A, 530, A99
Fabian, A. C., Iwasawa, K., Reynolds, C. S., & Young, A. J. 2000, PASP, 112, 1145
Fabian, A. C., Rees, M. J., Stella, L., & White, N. E. 1989, MNRAS, 238, 729
Fabian, A. C. & Ross, R. R. 2010, Space Sci. Rev., 157, 167
Fender, R. 2010, in Lecture Notes in Physics, Berlin Springer Verlag, Vol. 794, Lecture Notes in Physics, Berlin Springer Verlag, ed. T. Belloni, 115
Feroci, M., Stella, L., Vacchi, A., et al. 2010, in Society of Photo-Optical Instrumentation Engineers (SPIE) Conference Series, Vol. 7732, Society of Photo-Optical Instrumentation Engineers (SPIE) Conference Series
Ford, E. C., van der Klis, M., Méndez, M., et al. 2000, ApJ, 537, 368

Frank, J., King, A., & Raine, D. 1992, Science, 258, 1015
Frank, J., King, A. R., & Lasota, J.-P. 1987, A&A, 178, 137
Galloway, D. K., Psaltis, D., Muno, M. P., & Chakrabarty, D. 2006, ApJ, 639, 1033
George, I. M. & Fabian, A. C. 1991, MNRAS, 249, 352
Giacconi, R., Murray, S., Gursky, H., et al. 1974, ApJS, 27, 37
Gierliński, M. & Done, C. 2002, MNRAS, 337, 1373
Giles, A. B., Hill, K. M., Strohmayer, T. E., & Cummings, N. 2002, ApJ, 568, 279
Gilfanov, M. & Revnivtsev, M. 2005, Astronomische Nachrichten, 326, 812
Gilfanov, M., Revnivtsev, M., & Molkov, S. 2003, A&A, 410, 217
Gruber, D. E., Blanco, P. R., Heindl, W. A., et al. 1996, A&AS, 120, C641+
Hasinger, G. & van der Klis, M. 1989, A&A, 79
Hiemstra, B., Méndez, M., Done, C., et al. 2011, MNRAS, 411, 137
Hoffman, J. A., Lewin, W. H. G., & Doty, J. 1977, ApJ, 217, L23
Homan, J. & Belloni, T. 2005, Ap&SS, 300, 107
Homan, J., Klein-Wolt, M., Rossi, S., et al. 2003, ApJ, 586, 1262
Homan, J., Miller, J. M., Wijnands, R., et al. 2005, ApJ, 623, 383
Homan, J., van der Klis, M., Fridriksson, J. K., et al. 2010, ApJ, 719, 201
Homan, J., van der Klis, M., Jonker, P. G., et al. 2002, ApJ, 568, 878
Homan, J., van der Klis, M., Wijnands, R., et al. 2007a, ApJ, 656, 420
Homan, J., Wijnands, R., Altamirano, D., & Belloni, T. 2007b, The Astronomer's Telegram, 1165, 1
Homan, J., Wijnands, R., van der Klis, M., et al. 2001, ApJS, 132, 377
Iaria, R., D'Aí, A., di Salvo, T., et al. 2009, A&A, 505, 1143
Jahoda, K., Markwardt, C. B., Radeva, Y., et al. 2006, ApJS, 163, 401
Jonker, P. G., Méndez, M., & van der Klis, M. 2002, MNRAS, 336, L1
Jonker, P. G., van der Klis, M., Wijnands, R., et al. 2000, ApJ, 537, 374
Jonker, P. G., Wijnands, R., van der Klis, M., et al. 1998, ApJ, 499, L191
Kaaret, P., Piraino, S., Bloser, P. F., et al. 1999, ApJ, 520, L37
Kallman, T. & White, N. E. 1989, ApJ, 341, 955
Klein-Wolt, M., Homan, J., & van der Klis, M. 2004, Nuclear Physics B Proceedings Supplements, 132, 381
Kluzniak, W. & Abramowicz, M. A. 2001, ArXiv Astrophysics e-prints
—. 2002, ArXiv Astrophysics e-prints
Kluźniak, W., Abramowicz, M. A., Kato, S., Lee, W. H., & Stergioulas, N. 2004, ApJ, 603, L89
Krauss, M. I., Juett, A. M., Chakrabarty, D., Jonker, P. G., & Markwardt, C. B. 2006, The Astronomer's Telegram, 777, 1
Kuulkers, E., van der Klis, M., Oosterbroek, T., et al. 1994, A&A, 289, 795

Lamb, F. K. 1991, in NATO ASIC Proc. 344: Neutron Stars, ed. J. Ventura & D. Pines, 445
Lamb, F. K., Shibazaki, N., Alpar, M. A., & Shaham, J. 1985, Nature, 317, 681
Laming, J. M. & Titarchuk, L. 2004, ApJ, 615, L121
Laor, A. 1991, ApJ, 376, 90
Lattimer, J. M. & Prakash, M. 2007, Phys. Rep., 442, 109
Laurent, P. & Titarchuk, L. 2007, ApJ, 656, 1056
Leahy, D. A., Darbro, W., Elsner, R. F., et al. 1983, ApJ, 266, 160
Lee, H. C. & Miller, G. S. 1998, MNRAS, 299, 479
Levine, A. M., Bradt, H., Cui, W., et al. 1996, ApJ, 469, L33+
Li, L.-X., Zimmerman, E. R., Narayan, R., & McClintock, J. E. 2005, ApJS, 157, 335
Lin, D., Altamirano, D., Homan, J., et al. 2009a, ApJ, 699, 60
Lin, D., Remillard, R. A., & Homan, J. 2007, ApJ, 667, 1073
—. 2009b, ApJ, 696, 1257
Linares, M., van der Klis, M., Altamirano, D., & Markwardt, C. B. 2005, ApJ, 634, 1250
Linares, M., van der Klis, M., & Wijnands, R. 2007, ApJ, 660, 595
Mason, K. O., Breeveld, A., Much, R., et al. 2001, A&A, 365, L36
Matt, G., Perola, G. C., & Piro, L. 1991, A&A, 247, 25
Meheut, H. & Tagger, M. 2009, MNRAS, 399, 794
Méndez, M. 2001, in The Neutron Star - Black Hole Connection, ed. C. Kouveliotou, J. Ventura, & E. van den Heuvel, 313
Méndez, M. 2006, MNRAS, 371, 1925
Méndez, M. & Belloni, T. 2007, MNRAS, 381, 790
Méndez, M. & van der Klis, M. 1997, ApJ, 479, 926
Méndez, M. & van der Klis, M. 1999, ApJ, 517, L51
Méndez, M., van der Klis, M., & Ford, E. C. 2001, ApJ, 561, 1016
Méndez, M., van der Klis, M., Ford, E. C., Wijnands, R., & van Paradijs, J. 1999, ApJ, 511, L49
Mendez, M., van der Klis, M., van Paradijs, J., et al. 1998, ApJ, 494, L65+
Miller, J. M. 2007, ARA&A, 45, 441
Miller, J. M., Fabian, A. C., Reynolds, C. S., et al. 2004, ApJ, 606, L131
Miller, J. M., Fabian, A. C., Wijnands, R., et al. 2002, ApJ, 578, 348
Miller, J. M., Wijnands, R., Homan, J., et al. 2001, ApJ, 563, 928
Miller, M. C., Lamb, F. K., & Cook, G. B. 1998a, ApJ, 509, 793
Miller, M. C., Lamb, F. K., & Psaltis, D. 1998b, ApJ, 508, 791
Misra, R. & Kembhavi, A. K. 1998, ApJ, 499, 205
Misra, R. & Sutaria, F. K. 1999, ApJ, 517, 661

Mitsuda, K., Inoue, H., Koyama, K., et al. 1984, PASJ, 36, 741
Morgan, E. H., Remillard, R. A., & Greiner, J. 1997, ApJ, 482, 993
Ng, C., Díaz Trigo, M., Cadolle Bel, M., & Migliari, S. 2010, A&A, 522, A96+
Osherovich, V. & Titarchuk, L. 1999, ApJ, 522, L113
Pandel, D., Kaaret, P., & Corbel, S. 2008, ApJ, 688, 1288
Papitto, A., Di Salvo, T., D'Aì, A., et al. 2009, A&A, 493, L39
Piraino, S., Santangelo, A., di Salvo, T., et al. 2007, A&A, 471, L17
Piraino, S., Santangelo, A., & Kaaret, P. 2000, A&A, 360, L35
Pozdnyakov, L. A., Sobol, I. M., & Syunyaev, R. A. 1983, Astrophysics and Space Physics Reviews, 2, 189
Press, W. H., Flannery, B. P., Teukolsky, S. A., & Vetterling, W. T. 1989, Numerical recipes in C. The art of scientific computing
Pringle, J. E. & Rees, M. J. 1972, A&A, 21, 1
Psaltis, D., Belloni, T., & van der Klis, M. 1999, ApJ, 520, 262
Rebusco, P. 2004, PASJ, 56, 553
Reis, R. C., Fabian, A. C., & Young, A. J. 2009, MNRAS, 399, L1
Remillard, R., Muno, M., McClintock, J., & Orosz, J. 2002a, in APS Meeting Abstracts, 17076
Remillard, R. A., Lin, D., ASM Team at MIT, & NASA/GSFC. 2006a, The Astronomer's Telegram, 696, 1
Remillard, R. A. & McClintock, J. E. 2006, ARA&A, 44, 49
Remillard, R. A., McClintock, J. E., Orosz, J. A., & Levine, A. M. 2006b, ApJ, 637, 1002
Remillard, R. A., Morgan, E. H., McClintock, J. E., Bailyn, C. D., & Orosz, J. A. 1999, ApJ, 522, 397
Remillard, R. A., Sobczak, G. J., Muno, M. P., & McClintock, J. E. 2002b, ApJ, 564, 962
Reynolds, C. S. & Fabian, A. C. 2008, ApJ, 675, 1048
Reynolds, C. S. & Wilms, J. 2000, ApJ, 533, 821
Rodriguez, J., Corbel, S., Kalemci, E., Tomsick, J. A., & Tagger, M. 2004, ApJ, 612, 1018
Ross, R. R. & Fabian, A. C. 1993, MNRAS, 261, 74
—. 2005, MNRAS, 358, 211
Ross, R. R., Fabian, A. C., & Young, A. J. 1999, MNRAS, 306, 461
Rothschild, R. E., Blanco, P. R., Gruber, D. E., et al. 1998, ApJ, 496, 538
Ruszkowski, M., Fabian, A. C., Ross, R. R., & Iwasawa, K. 2000, MNRAS, 317, L11
Sanna, A., Hiemstra, B., Méndez, M., et al. 2012b, in preparation
Sanna, A., Méndez, M., Altamirano, D., et al. 2010, MNRAS, 408, 622
Sanna, A., Méndez, M., Belloni, T., & Altamirano, D. 2012a, MNRAS, 424,

2936
Savitzky, A. & Golay, M. J. E. 1964, Analytical Chemistry, 36, 1627
Shakura, N. I. & Sunyaev, R. A. 1973, A&A, 24, 337
Shih, I. C., Bird, A. J., Charles, P. A., Cornelisse, R., & Tiramani, D. 2005, MNRAS, 361, 602
Stella, L. & Vietri, M. 1998, ApJ, 492, L59+
Strohmayer, T. E. 2001a, ApJ, 552, L49
—. 2001b, ApJ, 554, L169
Strohmayer, T. E. & Markwardt, C. B. 2002, ApJ, 577, 337
Strohmayer, T. E., Zhang, W., Swank, J. H., et al. 1996, ApJ, 469, L9
Strüder, L., Aschenbach, B., Bräuninger, H., et al. 2001, A&A, 365, L18
Sunyaev, R. & Revnivtsev, M. 2000, A&A, 358, 617
Sunyaev, R. A. & Titarchuk, L. G. 1980, A&A, 86, 121
Sunyaev, R. A. & Truemper, J. 1979, Nature, 279, 506
Svoboda, J., Dovciak, M., Goosmann, R. W., & Karas, V. 2009, ArXiv e-prints
Tanaka, Y., Nandra, K., Fabian, A. C., et al. 1995, Nature, 375, 659
Taylor, J. H., Wolszczan, A., Damour, T., & Weisberg, J. M. 1992, Nature, 355, 132
Thorne, K. S. & Price, R. H. 1975, ApJ, 195, L101
Titarchuk, L. 1994, ApJ, 434, 570
Titarchuk, L., Kazanas, D., & Becker, P. A. 2003, ApJ, 598, 411
Titarchuk, L., Laurent, P., & Shaposhnikov, N. 2009, ApJ, 700, 1831
Turner, M. J. L., Abbey, A., Arnaud, M., et al. 2001, A&A, 365, L27
Turner, T. J., Mushotzky, R. F., Yaqoob, T., et al. 2002, ApJ, 574, L123
van der Klis, M. 1989, in Timing Neutron Stars, ed. H. Ögelman & E. P. J. van den Heuvel, 27
van der Klis, M. 1997, in Astrophysics and Space Science Library, Vol. 218, Astronomical Time Series, ed. D. Maoz, A. Sternberg, & E. M. Leibowitz, 121
van der Klis, M. 2001, ApJ, 561, 943
—. 2004a, ArXiv Astrophysics e-prints
—. 2004b, in "The Many Faces of Neutron Stars", NATO ASI Series, 515, 337
—. 2005, Astronomische Nachrichten, 326, 798
—. 2006, Rapid X-ray Variability, ed. Lewin, W. H. G. & van der Klis, M., 39–112
van der Klis, M., Hasinger, G., Damen, E., et al. 1990, ApJ, 360, L19
van der Klis, M., Swank, J., Zhang, W., et al. 1996, IAU Circ., 6319, 1
van Paradijs, J., van der Klis, M., van Amerongen, S., et al. 1990, A&A, 234, 181
van Paradijs, J. & White, N. 1995, ApJ, 447, L33

van Straaten, S., Ford, E. C., van der Klis, M., Méndez, M., & Kaaret, P. 2000, ApJ, 540, 1049
van Straaten, S., van der Klis, M., di Salvo, T., & Belloni, T. 2002, ApJ, 568, 912
van Straaten, S., van der Klis, M., & Méndez, M. 2003, ApJ, 596, 1155
van Straaten, S., van der Klis, M., & Wijnands, R. 2005, ApJ, 619, 455
Vaughan, S., Edelson, R., Warwick, R. S., & Uttley, P. 2003, MNRAS, 345, 1271
Verner, D. A., Ferland, G. J., Korista, K. T., & Yakovlev, D. G. 1996, ApJ, 465, 487
Wijnands, R., Homan, J., van der Klis, M., et al. 1998, ApJ, 493, L87
Wijnands, R. & van der Klis, M. 1999, ApJ, 514, 939
Wijnands, R., van der Klis, M., Homan, J., et al. 2003, Nature, 424, 44
Wijnands, R. A. D., van der Klis, M., van Paradijs, J., et al. 1997, ApJ, 479, L141
Willmore, A. P., Mason, K. O., Sanford, P. W., et al. 1974, MNRAS, 169, 7
Wilms, J., Allen, A., & McCray, R. 2000, ApJ, 542, 914
Yu, W., van der Klis, M., & Jonker, P. G. 2001, ApJ, 559, L29
Zdziarski, A. A., Johnson, W. N., & Magdziarz, P. 1996, MNRAS, 283, 193
Zhang, G., Méndez, M., & Altamirano, D. 2011, MNRAS, 413, 1913
Zhang, W., Giles, A. B., Jahoda, K., et al. 1993, in Proc. SPIE Vol. 2006, p. 324-333, EUV, X-Ray, and Gamma-Ray Instrumentation for Astronomy IV, Oswald H. Siegmund; Ed., 324–333
Zhang, W., Lapidus, I., Swank, J. H., White, N. E., & Titarchuk, L. 1997, IAU Circ., 6541, 1
Życki, P. T., Done, C., & Smith, D. A. 1999, MNRAS, 309, 561

Samenvatting in het Nederlands

Compacte objecten zijn de evolutionaire eindproducten van sterren. Wanneer een ster al haar energie heeft verbruikt, zal de naar buiten gerichte stralingsdruk afnemen en zal onder invloed van de zwaartekracht de ster ineenkrimpen en samengedrukt worden tot een ster met een vele hogere dichtheid. Afhankelijk van de ineengedrukt massa, kan het compacte object een witte dwerg, een neutronenster (NS), of een zwart gat (BH, Engels: black hole) zijn. Bij een NS wordt de zwaartekracht gebalanceerd door de tegendruk opgebouwd door gedegenereerde neutronen in de kern van de NS. Een neutronenster heeft een massa tussen de 1.4 en 3 keer die van onze zon en een straal die tussen de 10 en 20 km bedraagt. In een zwart gat is de tegendruk onbekend en de kern is mogelijk samengeperst tot een singulariteit. Stellaire zwarte gaten hebben een massa van ongeveer 10 zonsmassa's en hebben een onbekende afmeting. In de praktijk wordt een zwart gat gekarakteriseerd door een wiskundig gedefinieerd oppervlak dat de waarneemhorizon wordt genoemd. Deze waarneemhorizon begrenst het volume waaruit niets (zelfs licht niet) kan ontsnappen aan de zwaartekracht van het zwarte gat.

Nadat de compacte objecten gevormd zijn, zullen ze simpelweg afkoelen en energie verliezen waardoor ze niet tot nauwelijks waarneembaar zullen zijn in het geval ze afgezonderd achterblijven. Aan de andere kant, in het geval dat het compacte object zich in een dubbelstersysteem bevindt en zich voedt met materie afkomstig van de begeleidende ster (ook wel accretie genoemd), kunnen deze systemen zich ontpoppen tot spectaculair heldere objecten. Röntgendubbelstersystemen zijn heldere röntgenbronnen die verbonden worden met accreterende neutronensterren en zwarte gaten. In dit proefschrift onderzoek ik de fysica van accretieprocessen in lage massa röntgendubbelstersystemen (LMXBs, Engels: low-mass X-ray binaries), waarin een neutronenster of een stellair zwart gat materie accreteert van een begeleidende ster met een lage massa (minder dan die van onze zon), zie Figuur 1 voor een artistieke weergave van zo'n systeem.

Wanneer in een röntgendubbelstersysteem de begeleidende ster haar Roche-Lobe vult (dit is het druppelvormige gebied om een ster in een dubbelstersys-

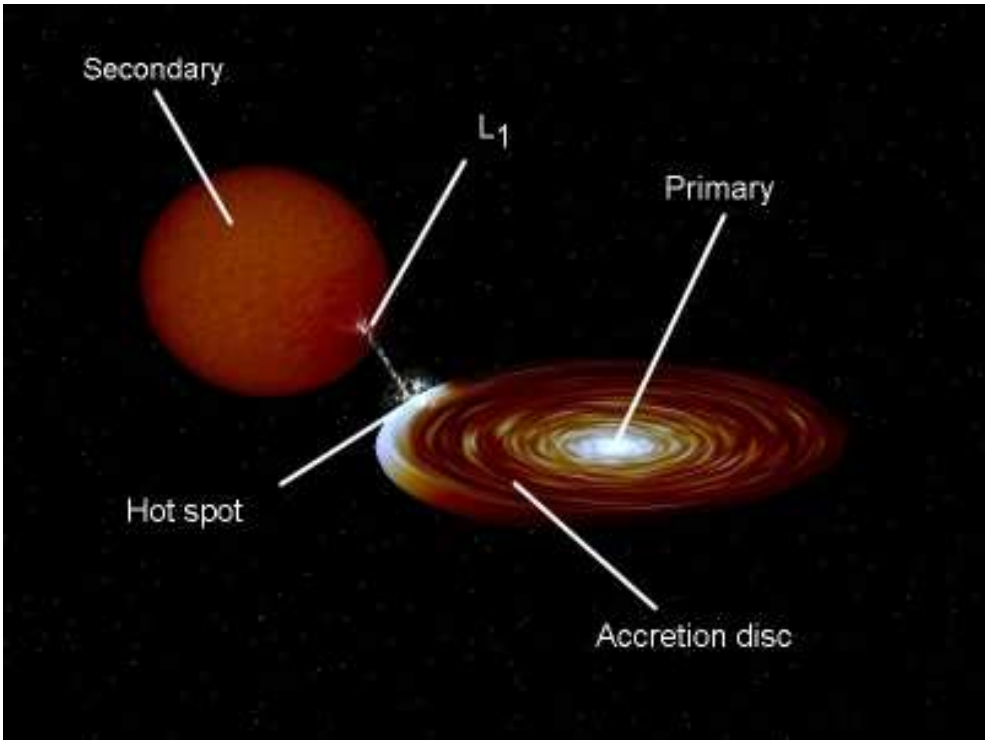

Figuur 1: Artistieke weergave van een röntgendubbelstersysteem waarin een normale ster (aangeduid met secondary) en een compact object (primary) om elkaar heen draaien. Materie wordt overgedragen via de binnenste Lagrangiaan (L1) en vormt een zogenoemde accretieschijf om het compacte object heen.

teem, waarbinnen het gas door de zwaartekracht is gebonden aan die ster), wordt de materie gewoonlijk overgedragen via de binnenste Lagrangiaan (het punt tussen de twee objecten in waar de kinetische en potentiële energie van het systeem gelijk aan elkaar is). De draaiing van de twee sterren om elkaar heen zorgt ervoor dat de overgedragen materie niet direct op het compacte object valt maar beschrijft een cirkelvormige baan om het compacte object heen en vormt op deze manier een roterende schijf, de accretieschijf genaamd. De waargenomen röntgenstraling afkomstig van deze dubbelstersystemen wordt geproduceerd in de binnenste gebieden van deze accretieschijf en de omliggende corona en komt mogelijk ook vrij van het oppervlak/grensvlak van de neutronenster wanneer de accreterende materie inslaat op het oppervlak van de neutronenster.

Röntgendubbelstersystemen vormen een belangrijke kosmologische omgeving om accretieprocessen te onderzoeken. De kenmerken van de straling

afkomstig van deze systemen, van radio- tot gammastraling, hangt af van de accretiesnelheid (oftewel de hoeveelheid overgedragen materie per tijdseenheid) en de eigenschappen van het compacte object, zoals de massa, het magnetisch veld en de rotatiesnelheid, oftewel spin van het compacte object. De natuurkunde achter de accretieprocessen is nog niet volledig begrepen en er bestaan diverse manieren waarop accretie zich manifesteert, bijvoorbeeld in quasi-periodieke oscillaties en 'jets', die mogelijk de aard en de intrinsieke parameters van het compacte object kunnen onthullen.

Een andere reden om röntgendubbelstersystemen te bestuderen is het unieke blikveld wat accretie op NS en BH schept in de fysica van de sterke zwaartekracht en dichte materie. Algemeen relativistische effecten rond deze compacte objecten zijn vele ordes van grootte sterker dan die waarop de algemene relativiteitstheorie succesvol is getest (het zwakke veld domein). Onder de extreme voorspellingen die de algemene relativiteitstheorie voor deze gebieden maakt, bevinden zich het bestaan van de waarneemhorizon van het zwarte gat en het bestaan van een binnenste straal (van de accretieschijf) waarbinnen geen stabiele baanbeweging meer mogelijk is (beter bekend als de ISCO, Engels: innermost stable circular orbit). In het inwendige van een neutronenster overschrijdt de dichtheid van de materie dat van een atoomkern. De precieze aard van de elementaire deeltjes waaruit de neutronenster is samengesteld en hun gezamenlijke eigenschappen zijn nog steeds niet goed genoeg begrepen om de toestandsvergelijking (Engels: equation of state) van neutronensterren vast te kunnen stellen. Door de baanbeweging rond een NS te onderzoeken, kunnen zowel de massa en de straal van de NS vastgesteld worden wat vervolgens kan helpen tot het preciezer bepalen van de toestandsvergelijking en aansluitend kan leiden tot een beter inzicht in de fundamentele eigenschappen van het materiaal waar de NS uit gemaakt is.

Met het oog op het begrijpen van röntgendubbelstersystemen bestuderen we de fotonen uitgezonden door deze systemen. Hoewel het energiespectrum van deze objecten zich uitstrekt van radio- tot gammagolflengten, richt ik me in mijn onderzoek alleen op de röntgenstraling afkomstig uit de nabije omgeving van het compacte object. Momenteel zijn we helaas nog niet in staat om via directe beeldvormende technieken in het röntgengebied de LMXBs ruimtelijk op te lossen. Vandaar dat we genoodzaakt zijn spectrale- en tijdsanalyses toe te passen op de waargenomen röntgenfotonen om zodoende de spectrale evolutie van de bron te begrijpen alswel de intrinsieke parameters van het compacte object te bepalen. In het bijzonder staan in dit proefschrift de kilohertz quasi-periodieke oscillaties (kHz QPOs) en de relativistische ijzeremissielijnen in de belangstelling omdat ze respectievelijk de variabiliteit en de spectrale eigenschappen van LMXBs weergeven.

kHz QPOs zijn de snelste (zo ver bekend) tijdsveranderlijke componenten in röntgendubbelstersystemen. Deze componenten zijn onderdeel van het zogenoemde 'power-density spectrum', wat de weergave is van het kwadraat van de modulus van de Fourier transformatie van de röntgenlichtkromme als functie van de frequentie. De waargenomen hoge-frequentie QPOs in NS-LMXBs hebben een frequentie tussen de 200 en 1300 Hz terwijl die in BH-LMXBs een frequentie hebben tussen de 40 en 500 Hz. Deze hoge-frequentie QPOs worden toegeschreven aan de beweging van materie aan de binnenste rand van de accretieschijf. Als dit scenario correct is dan zullen kHz QPOs één van de weinige bruikbare gereedschappen zijn om de algemene relativiteitstheorie in het sterke zwaartekrachtsveld te onderzoeken. Verder kan, onder de aanname dat de accretieschijf zich uitstrekt tot aan de ISCO, aan de hand van het meten van de frequentie van de QPO de straal van de ISCO worden afgeleid, welk direct afhangt van de massa en de afmeting van de NS.

De ijzeremissielijn is het sterkste kenmerk in het zogenoemde reflectiespectrum, een spectrum dat ontstaat wanneer hoog-energetische röntgenfotonen een optisch dik materiaal, zoals de accretieschijf, bestralen. De ijzeremissielijn vertoont vaak een karakteristiek breed en asymmetrisch profiel. Het wordt aangenomen dat de straling van dit spectrale kenmerk voornamelijk van de binnenste rand van de accretieschijf afkomt, daar waar het materiaal met zeer hoge snelheden roteert, snelheden die zelfs de helft van de lichtsnelheid kunnen bedragen. Hier verder op gebaseerd, wordt het bijzondere lijnprofiel verklaard aan de hand van de combinatie van Doppler- en relativistische effecten die weer samenhangen met de emissie van fotonen afkomstig van snel roterende materie aan de binnenste rand van de accretieschijf en in de nabijheid van het compacte object. In deze interpretatie geeft het lijnprofiel direct de fundamentele parameters van het compacte object weer, zoals de massa en het hoekmoment, maar geeft bovendien ook enkele parameters van het systeem, zoals de inclinatie. Het modelleren van de ijzeremissielijn met relativistische lijnprofielen geeft ons de mogelijkheid om de eigenschappen van het compacte object te bepalen.

In dit proefschrift richt ik me op de variabiliteit en spectrale manifestaties van verschillende LMXBs om zo de eigenschappen van de accretiestroom in de nabijheid van het compacte object te onderzoeken. In hoofdstuk 2 leg ik me toe op de eigenschappen van de kHz QPOs waargenomen in de zogenoemde 'transient' röntgenbron XTE J1701−462, één van de weinige bronnen (voor zover ontdekt zijnde) die tijdens een uitbarsting een transitie onderging van een Z klasse (hoge lichtkrachtstoestand) naar een atoll klasse (lage lichtkrachtstoestand). Ik concludeer hieruit dat de eigenschappen van de QPO, zoals de sterkte en de coherentie, niet slechts afhangt van de geometrie van de

accretieschijf, daar waar de QPOs hun oorsprong hebben.

In hoofdstuk 3 bestudeer ik de kHz QPOs in de LMXB 4U 1636−53, me daarbij richtend op hoe de frequentie van de QPO verandert met de tijd. Verder onderzoek ik de correlatie tussen de frequentie van de QPO en de straal van de accretieschijf, waarbij ik de tijdsafgeleide van de QPO frequentie omschrijf in termen van de fysica van de accretieschijf.

In hoofdstuk 4 analyseer ik systematisch de RXTE/PCA waarnemingen van 22 'transient' BH-LMXBs, zoekend naar de hoge-frequentie QPOs. Vervolgens vergelijk ik de eigenschappen van deze hoge-frequentie QPOs met die van de kHz QPOs van neutronensterren om zodoende te onderzoeken of de frequenties van de oscillaties in beide klassen van bronnen daadwerkelijk verklaard kunnen worden in termen van hetzelfde natuurkundige mechanisme.

In hoofdstuk 5 richt ik me op de ijzeremissielijn waargenomen in het spectrum van de NS LMXB 4U 1636−53. Ik bestudeer hierin het lijnprofiel met een aantal fenomenologische modellen, inclusief symmetrische en relativistisch-verbrede profielen, en tevens met een relativistisch verbreed, geioniseerd reflectie model. Het doel hiervan is om de straal van de accretieschijf te bepalen, daar waar de ijzeremissielijn zijn oorsprong vindt.

In hoofdstuk 6 combineer ik tegelijkertijd de bepalingen van de binnenste straal van de accretieschijf die verworven zijn via de kHz QPOs en via de analyse van de ijzeremissielijn in de NS LMXB 4U 1636−53. Bovendien onderzoek ik het verband tussen de ijzeremissielijn, de kHz QPOs en de spectrale toestanden met tot doel hebbende om uit te zoeken en te begrijpen of de bestaande interpretaties van deze fenomenen correct zijn.

Acknowledgments

Let us be grateful to the people who make us happy; they are the charming gardeners who make our souls blossom.

Marcel Proust

Here it finally comes the last part of the thesis... My experience here is almost over and soon I will be leaving Groningen. After five years of incredibly intense and interesting experiences, now it is probably the best moment to thank all the people that helped me through this long journey.

First thing first, I would like to thank Mariano for offering me the chance to work on my Ph.D. Thanks for always being very patient and understanding, even during our scientific discussions where I often pulled my *"I'm right, you are wrong"* stubborn attitude. I really enjoyed our coffee meetings that surely I am going to miss so much. You have been an incredibly good boss and at the same time a very good friend, and for that I am thankful. I liked your positive attitude, every time I stepped into your office with a problem you either had the solution or at least good advice to help me solve it. I would like to thank you for supporting me and believing in my capabilities even when I was not fully aware of them. You taught me almost everything I know about science and this thesis would not have been the same without you. I hope these last 5 years were just the beginning of a long friendship and a scientific collaboration.

I would like to thank Tomaso for all the very interesting collaborations we had over these years. Thanks a lot for all the interesting ideas you shared with me, for all the suggestions and comments that made this thesis more interesting. Thanks again for giving me the possibility to visit you in Merate. I really enjoyed working with you and I look forward to keeping this collaboration in the future.

A huge thanks goes to Luciano and Tiziana for all the interesting conversations and for giving me the possibility to work with Mariano before my Ph.D.

Sara, thanks for all the help and nice discussions we had during these years. During my Ph.D I spent so much time at work that I started feeling like I was at home. This is why I would like to thank Hennie, Jackie, Gineke, Christa and Lucia for making the Kapteyn Institute such a pleasant and joyful, but at the same time very efficient, place to work. Thanks to Eite, Martin and especially Wim for being always ready to help out with computer issues.
I would like to thank the institutions that gave me the possibility to follow very interesting and useful conferences, workshops and working visits: Kapteyn Institute, NWO, LKBF and ISSI.
I am grateful to the reading committee members: Chris, Luigi and Didier for a careful reading of this thesis.
Thanks to Peter, Germán, Zsofia, Stephan, Hans and Asa for sharing the office with me, which I guess it has not always been an easy task :-)
I would like to thanks all the members and aficionados of the High Energy Group: Paolo, Beike, Guobao, Diego, Lyu Ming, Valeriu, Dave, Federico, Sandra, Omar, Gerjon, Mathijs, and Marcio for all the interesting and inspiring discussions and for showing me that science meetings can also be very funny.
Beike, thanks for being such a nice collaborator and friend, a special thank for taking care of me with very nice (real Italian) coffee. Thank you very much for finding the time to translate my summary in Dutch, you did a wonderful job. Sorry again for not being able, at the very last moment, to be your paranymph.
Diego, I do not even know where to start... you are probably the person who helped me the most (besides Mariano) throughout my Ph.D. I enjoyed a lot discussing about work with you and I really liked your being always very supportive and encouraging. Thanks a lot for letting me crash at your place in Amsterdam and for the nice background pictures for the iPad :-) I really had fun playing sports with you, I still have vivid memories of our basketball matches (man, you are too old for that game!!), however to be fair you always beat me at squash.
Guobao, thanks for always being ready to help me out. I honestly admire your positive attitude: in the last 5 years I never saw you angry or discouraged, you always walked around with a big smile on your face. Thanks a lot for that, it was very inspiring!
Paolo, I am glad I had the possibility to work with you. All these years you have been like a brother to me, someone you can always rely on, someone that always has time to listen and to give support. I wish you all the best with Jenny and Marco, you three make a beautiful family. Thanks a lot for all the delicious dinners.
Marcio, it was very nice having you around here in Groningen. If your offer is

still valid, I will find a good (work related) excuse to visit you in Brazil. You know, some project that requires a lot of thinking at the beach :-)
These last few years in Groningen have been a unique life experience, a mixture of excitement for a new job challenge and sadness for not having the people I love around me. Overall I am glad with this experience and I would like to thank the people that helped me and contributed to make my life here easier and enjoyable.
Giamba, we started this journey together and I have to admit that it helped me a lot having you around. Sharing the apartment was probably not the smartest move in the history of our friendship, but I am happy things are finally better now.
Facu, thanks for being able to regularly organise the Sunday afternoon football matches, it is not as easy as it might sound. Thanks also for hosting the best FIFA tournaments ever :-)
Anto, thanks a lot for all the nice dinners and movie nights. Thanks also for all the relaxing coffee and cigarette breaks.
Peter, thanks for keeping on trying to interact with me in the first period despite my embarrassing level of English. Thanks also for letting witness one of your last music performances, your scary-death-growl style of singing still gives me nightmares sometimes :-S
Aycin, you are the only person who somehow made me eat yogurt and I can assure you many people tried hard and failed in the past. To be completely fair it was yogurt soup and I only discovered it after I ate it, but still very impressive. Thanks also for the very nice Turkish food you introduced me to, you are a very good cook.
Paolo, your Sardinian accent made me feel at home. Thanks for showing me how hard is to fly kites. Thanks also for all those interesting discussions during coffee breaks.
Mirjam, thanks for being so helpful with me and Claudia when we first moved in your neighbourhood, it really meant a lot. Sophie, you are one of the cutest and funniest kid I have ever seen. Thanks for teaching me how to make animal puzzles.
Mati, thanks a lot for cooking *empanadas*, they where delicious.
JP, thanks for sharing for two years in a row your birthday party with me, we had a lot of fun celebrating.
Boris, a huge thank you for the amazing races at the Euro Kartracing, kudos for your driving skills. Btw, sorry for breaking your record ;-)
Oscar, you are probably one of the funniest and most frank people I have ever met. I had so much fun playing Guitar Hero, PES, poker, football, pretending to learn how to play real guitar and so many other things, that I am really

going to miss you a lot.
Teresa, thanks for letting me make jokes every time you talk about Catalunya, you should see your face sometimes >:(To make it up to you, I will also embrace the movement, so: *Som una nació. Nosaltres decidim.* :-P
Carlos, thanks for all the hilarious conversations we have when I stopped by your office. Thanks also for your priceless faces every time I mentioned you had to fill an extra form for the thesis.
Koshy, thanks for all the fun during the happy hour, it is always very nice talking to you. Thanks also for randomly meeting you in the bus at the weirdest hours of the night.
Harish, you are beyond hilarious, some of your jokes almost made me pee my pants. I had so much fun during happy hours where you, German and I usually ended up engaging in never ending philosophical conversations. Iva, thanks a lot for all the very nice chats during coffee breaks, and good luck taking care of Harish. I hope you guys will come visit me in Sardinia, maybe you could go hiking.
Germán, first I would like to thank you for accepting to be my paranymph, it really means a lot to me. Thanks for being such a nice friend during all these years, you were very supportive especially during the toughest moments. Thanks for all the delicious Colombian dinners and thanks for almost destroying your bike trying to pull a wheelie.
Adriana, thanks a lot for transforming my simple idea into such a beautiful cover. Violeta, you are so sweet and cute. Thanks for playing with me and thanks for all your smiles. Germán, take good care of these two wonderful gals.
A special thanks goes to the Italian gang: Stefania, il Lelli, Giacomo, Giuliana, il Garuffi, Stefano, Linda, Simona, Giamba, Chiara, Paolo and Paolo, for bringing joy, vitality and nonetheless good coffee to the Kapteyn, making it even a more enjoyable place where to work.
Burcu, Esra, Pratyush, Robyn, Princess Katinka, Yan Ping, Parisa, Marius, Mark, Maarten, Sanaz, Nancy, Jan, Andrey, Rosina, Stéphanie, Vibor, Ajinkya, Oscar, Kyle, Thomas, and probably many more old colleagues that I am forgetting now, thanks for all the nice lunch breaks, parties, barbecues and conversations we had!
Vivere per così tanto tempo lontano da casa non è stata un' impresa semplice, per questo vorrei approfittare di questo momento per ringraziare gli amici e la famiglia per essermi stati sempre molto vicino e per avermi fatto sentire parte delle loro vite pur essendo fisicamente così distante. Un grazie di cuore a Luca, Francy, il piccolo Riccardo, Maury, Ricky, Cece, Corra e famiglia per tutte le piacevoli serate passate in vostra compagnia durante le vacanze. Grazie agli

esuli per i fantastici pranzi commemorativi. Cristian, grazie per tutte le serate di poker e le partite di calcetto. Ginetto, grazie mille per le ore passate in chat a cazzeggiare ricordando i bei tempi dell'università. Pippo, Manu e la piccola Emma, grazie per le belle chiacchierate e le cene al mare. Luca e Catia, grazie per il continuo supporto e i bei momenti passati assieme. Zap, non ho ancora capito esattamente come fai, ma ad ogni conversazione su Skype riesci sempre a tirar fuori un aneddoto incredibile.
Mamma e Papá, senza il vostro continuo supporto tutto questo sarebbe stato estremamente più difficile. Grazie per aver sempre creduto in me in tutti questi anni, vi voglio tanto bene!
Un grazie di cuore anche a mio fratello, mia sorella e alle loro famiglie per essermi stati sempre vicino in questo periodo. Grazie anche al piccolo Lorenzo per le divertenti quanto incomprensibili conversazioni su Skype.
Un grazie anche a Palmiro e Anna Maria per il loro affetto. Grazie Zio Luigi per tutto il supporto dimostrato in questi anni.
Finalmente ho la possibilità di ringraziare pubblicamente chi, più di chiunque altro, mi ha dato la forza di compiere questo percorso. Claudia, amore mio, grazie di cuore per aver gioito con me per ogni successo, di aver sofferto con me nei momenti di difficoltà, di avermi sostenuto quando mi sono mancate le forze e di aver colmato l'enorme distanza che ci ha separato amandomi ancora piú intensamente. Non vedo l'ora di poter cominciare a vivere un'altra emozionante fase della nostra vita, finalmente assieme nella nostra nuova casa. Ti Amo!

Pabillonis, 20 December 2012

I close my eyes
Only for a moment and the moment's gone
All my dreams
Pass before my eyes with curiosity

Dust in the wind
All they are is dust in the wind

Same old song
Just a drop of water in an endless sea
All we do
Crumbles to the ground, though we refuse to see

Dust in the wind
All they are is dust in the wind

Now don't hang on
Nothin' last forever but the earth and sky
It slips away
And all your money won't another minute buy

Dust in the wind
All we are is dust in the wind

Dust in the wind - Kansas